Università degli Studi di Padova

Dipartimento di Fisica e Astronomia "Galileo Galilei"

Corso di Laurea Magistrale in Astronomia

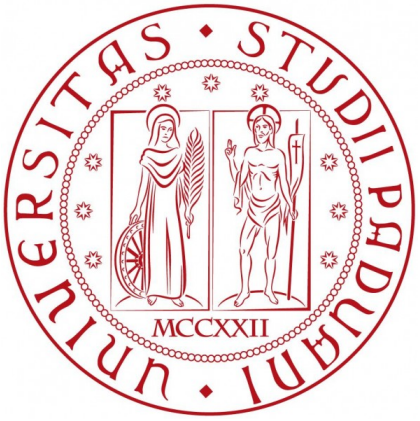

Tesi di Laurea Magistrale in Astronomia

Thermally Pulsing Asymptotic Giant Branch Stars in the Cluster NGC 419

Relatrice: Prof. Paola Marigo
Correlatori: Dr. Léo Girardi
Dr. Yang Chen
Dr. Giada Pastorelli

Laureanda: Maria Moressa

Anno Accademico 2017-2018

08/03/2018

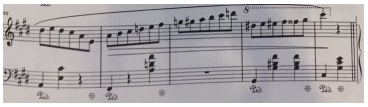

F. Chopin, *Waltz Op.64 No.2*

Contents

Abstract

In this work we study the *Thermally Pulsing Asymptotic Giant Branch* (TP-AGB) stars in the Small Magellanic Cloud (SMC) star cluster NGC 419. This is the known star cluster which is richest in TP-AGB and carbon stars. The metallicity is $Z \sim 0.003$, the turn-off mass $M \sim 1.65\ M_{\odot}$, and the distance modulus is $(m - M)_0 = 18.934$.

The aim of this work is twofold: i) to test available stellar models originally calculated for field TP-AGB stars of the SMC, and ii) to calibrate the processes involved during TP-AGB phase (mass loss and third dredge-up) to reproduce the observed properties of TP-AGB stars of the cluster (star counts and luminosities).

First we consider photometrical data by *High Resolution Channel* and by *Wide Field Channel* of the *Advanced Camera for Surveys* (respectively ACS/HRC and ACS/WFC) of Hubble Space Telescope to estimate the global properties of the cluster (age, mass). From the color-magnitude diagram (CMD) of NGC 419 we can note some dispersion, especially in the main sequence and in the turn-off. This is likely due to rotation but, since this aspect is not treated in the models, in order to have a satisfactory description of star counts related to pre-AGB phases, we analyze it as due to an age spread. The population synthesis code used is `TRILEGAL`. First of all we use ACS/HRC data and we consider the isochrone fitting method: with this method we find an age in the range [1.30; 1.60] Gyr. In this range we build the star formation history (SFH) of the cluster, trying to reproduce the luminosity function of the red clump region. The result is a prolonged SFH but with a clear peak at $t \sim 1.45\ Gyr$. With this SFH we are able to reproduce well the CMD of the red giants, and we expect to have a reasonable distribution of the core masses of stars entering the AGB phase. We are also able to estimate the stellar mass comprised in the HRC field.

Afterwards we use ACS/WFC data to estimate the total mass of the cluster: we consider the number density profile in order to assess the background density ($0.62\ pc^{-2}$) and the radius ($R = 1.18' = 21\ pc$) of the cluster. Within this radius we obtain a mass of $M = (1.31 \pm 0.11) \cdot 10^5\ M_{\odot}$.

Once determined the global properties of the cluster, in the second part of this work we consider near-IR data (`2MASS` and `CASPIR` photometry) of AGB stars of NGC 419. We first consider a complete list of AGB stars of the cluster and then we discard the ones which are outside the fixed radius of 21 pc and the ones which are below the tip of red giant branch ($K = 12.6\ mag$). The final sample consists of 19 TP-AGB stars: 11 carbon stars (C-star) and 8 oxygen-rich stars (M-stars). The transition luminosity is $K = 11.66\ mag$, while the AGB tip luminosity is $K = 10.71\ mag$. These are the key quantities which we try to reproduce in simulations.

We test eighteen `COLIBRI` models for TP-AGB stars, obtaining median values for the adopted quantities and 1σ error bars using the cumulative function. A general result of all models is a *deficit* of predicted M-stars and a too faint M/C transition luminosity (these quantities are mainly related to the onset of third dredge-up). There is instead a good agreement of most of the models with the data in reproducing the number of C-stars and the AGB tip luminosity. We discuss the three most different models: `S001`, `S014` and `S017`. We analyze their diffencences concerning mass loss regimes, characteristic of third dredge-up and the Hertzsprung-Russel diagrams. The general aspect required by all models for a better description of the data and for a following work is a later onset of the third dredge-up which would imply a longer M-phase and a brighter M/C transition luminosity.

The work is structured as follows.

In Chapter 1 there is a brief review of stellar evolution, of AGB phase and of its importance. In Chapter 2 there is a general description of AGB stars in star clusters, their importance in calibrating TP-AGB models and a presentation of NGC 419. In Chapter 3 we describe the population synthesis code `TRILEGAL` and we estimate global properties of the cluster. In Chapter 4 we consider the observed AGB sample and we describe and test the stellar evolutionary models. In Chapter 5 we discuss the models which present the most evident differences and we draw the final conclusions and the next steps for a following work.

Chapter 1

Basic Stellar Evolution

1.1 Stellar Evolution up to Asymptotic Giant Branch phase

Stars form from gravitational collapse and fragmentation of dense and cool molecular clouds which exceed the limit of *Jeans mass*, $M_J \propto T^{\frac{3}{2}}\rho^{-\frac{1}{2}}$ being T the temperature, and ρ the density. The result is a fully convective protostar of a given mass in hydrostatic equilibrium. Its luminosity is now provided by gravitational contraction, according to the *Virial Theorem* (VT) which connects mechanical and energy properties. For an ideal gas it can be demonstrated that VT yields $E_{int} = -\frac{1}{2}E_{grav}$ (where E_{int} and E_{grav} are internal and gravitational energies). In this phase the protostar occupies the so called *Hayashi line*: an almost vertical line in the *Hertzsprung-Russel* diagram, i.e. in the $LogL - LogT_{EFF}$ diagram (this means that $T_{eff} \sim constant$). *Hayashi line* is definied as the evolutionary path traced by a fully convective structure in hydrostatic equilibrium. Contraction continues causing temperature rise and the protostar leaves the *Hayashi line*. At certain point the central temperature is sufficiently high that nuclear fusion reactions can be activated in the core of the star. It must be said that stars exist within a finite mass range, $0.08M_\odot \lesssim M \lesssim 100M_\odot$: stars with too low masses are not able to trigger nuclear fusions in their core (*brown dwarves*), while stars with too high masses cannot exist because of dynamical reasons.

When temperature reaches $T \simeq 10^7\ K$, the star starts to burn hydrogen (H) in the core and, once the energy generated by nuclear burning compensates for the energy radiated at the surface, the star stops contracting and settles down on the *zero-age main sequence* (ZAMS). The *Main Sequence* (MS) is defined as the stage during which a star burns hydrogen in its nucleus and this is the longest evolutionary phase. The MS lifetime depends mainly on the stellar mass:

$$\tau_{MS} \approx 10^{10} yr \left(\frac{M}{M_\odot}\right)^{-2.5} \tag{1.1}$$

It can be seen, for example, that the Sun spends approximatively 10 Gyr on the MS. Stellar structures and hence the mechanism of H-burning are now very different depending on the mass:

- Stars with $M \lesssim 1.2M_\odot$ develope a radiative core and a convective envelope. H is burnt into helium (He) through the *proton-proton chain* (pp-chain) reaction, in which the net result is:

$$6p \rightarrow {}^4\mathrm{He}^{++} + 2p + 2e^+ + 2\nu + 2\gamma \tag{1.2}$$

(where e^+ is positron, ν is neutrino and γ is photon). Obviously the reaction proceeds through two-body collisions.

- Stars with $M \gtrsim 1.2M_\odot$ develope instead a convective core and a radiative envelope. H is now burnt into He through the *carbon-nitrogen-oxygen cycle* (CNO-cycle), in which the net result is:

$$4p \rightarrow {}^4\mathrm{He}^{++} + 2e^+ + 2\nu + 3\gamma \tag{1.3}$$

  This reaction obviously requires the presence of C, N, O nuclei (even if a small quantity is necessary) which act as catalysts.

The energy generation has different T-dependence in the two processes:

$$\epsilon_{PP} \propto T^4 \tag{1.4}$$

$$\epsilon_{CNO} \propto T^{18} \tag{1.5}$$

It can be noticed that T-dependence of CNO-cycle is steeper than the pp-chain one: at lower T pp-chain dominates, but with rising T there a fast transition to a CNO-cycle dominance. Both pp-chain and CNO-cycle can contribute in H-burning process at different efficiency, but because of the different T-dependence, CNO-cycle is more important for heavier stars since their interior regions reach higher temperatures.

A consequence of the H-burning is the increase of the mean molecular weight μ. It causes core contraction and hence an increase of burning rate and of the flux emitted: this is the *Sub giant branch* (SGB) phase where the star is left with a H-exhausted core (i.e. a He core), a H-burning shell and a H-rich envelope. The next evolutionary path of a star beyond H-consumption depends on its mass. Now the burning shell is the main energy source of stellar luminosity and continues burning hydrogen and adding He to the inert core. Once it exceeds the *Schönberg-Chandraseckhar* (SC) limit, $M_{core} \approx 0.10 M_{tot}$, thermal equilibrium is no longer possible and the core contracts and heats up until it reaches $T \sim 10^8\ K$, temperature required for He-burning to occur. This process occurs with different paths and requires a different time depending on the stellar mass:

- The core of low mass stars ($M \lesssim 2M_\odot$) contracts until the point of degeneracy (end of SGB), the outer layers expand and cool and the star evolves along the *Red giant branch* (RGB), close to the *Hayashi line*. During the RGB stars experience a mixing mechanism, the *first dredge up*: convective envelope moves down, bringing then to the surface H-burning products. During RGB it can be seen also the *RGB bump*: a sudden "bump" in the luminosity due to the discontinuity in H abundance left by the convective envelope at its deepest extent. After the bump, the star move very rapidly along the RGB up to the end of this phase: the *RGB tip*. The evolution track of a low mass star can be seen in Figure 1.1.

- SGB and RGB phases in intermediate-mass and massive stars (i.e. $M \geq 2M_\odot$) are faster. The evolution along SGB occurs in a thermal timescale ($\tau_{KH} \approx 10^5 yr$) so it causes the so called *Hertzsprung gap*, due to the low number of observed stars in this phase. At the onset of surface convection, star evolves along the *Hayashi line* (RGB phase). It's a short-lived phase during which the stars experience the *first dredge up*. The evolution track of intermediate-mass and massive stars can be seen in Figure 1.2.

As discussed, stars of all masses undergo the *first dredge up*. Another important process experienced during RGB is the mass loss, probably related to magneto-acoustic waves in the surface layers.

Once the SC limit is reached, He-burning in the core is triggered: helium is burnt into carbon, and the net result is

$$3\alpha \rightarrow {}^{12}\mathrm{C} + \gamma \tag{1.6}$$

The so called *triple-α* reaction, where α particles are He nuclei. The energy generation of *triple-α* process has a huge T-dependence:

$$\epsilon_{3\alpha} \propto T^{40} \tag{1.7}$$

The He-burning reaction is the same, but it takes place under different conditions in stars of different masses:

- In low mass stars He-ignition occurs in degenerate conditions: the *Helium flashes*. These are periodic episodes of non-catastrophic thermal runaway which happen in regions of maximum temperature that, because of neutrinos cooling processes, are a little off-centre. The enormous amount of energy released does not reach the surface but it is used to remove the degeneracy: the thermal runaway is quenched and He is then burnt in a quiescent condition. In evolutionary track (Figure 1.1), a low mass star passes rapidly from the top of RGB down to the region of He-burning called *Horizontal branch*. Since He-burning takes place at the same core mass $M_C \sim 0.45 M_\odot$, the luminosity of low-mass He-burning stars is almost independent on their mass, and this represents a key feature in *color-magnitude diagram* of star clusters since it allows to derive the distance of the object.

- In intermediate-mass and massive stars, He is burnt in a stable, non-degenerate manner in the convective core. In evolutionary track (Figure 1.2) this phase corresponds to the so called *blue loop*.

1.2 Asymptotic Giant Branch phase

The *Asymptotic Giant Branch* (AGB) phase is an advanced evolutionary stage after the central helium burning phase. At this point the further evolution, beyond helium (He) burning, is very different between stars of low-intermediate mass which develope a degenerate carbon-oxygen (CO) core and go through AGB phase, and massive stars which avoid the core degeneracy and undergo further nuclear burnings. So stars of interest in the next discussion, i.e. the ones which evolve along the AGB in *Hertzsprung-Russel* (HR) diagram, have an initial mass in the range $0.5 M_\odot \leq M \leq 8 M_\odot$. Qualitatively the last evolution of stars in this range is quite similar: they rise from AGBs undergoing strong mass loss, pass the phase of *planetary nebula* and end their lives as cooling *white dwarves*. Beyond this similarity, however, there are also some differences (e.g. the duration of each phase) which depend on the mass. Different evolutions of stars of $1 M_\odot$ and of $5 M_\odot$ can be seen respectively in Figure 1.1 and in Figure 1.2. Finally, during AGB phase, there is a tight *core-mass/luminosity* relation:

$$L = 5.9 \times 10^4 L_\odot \Big(\frac{M_C}{M_\odot} - 0.52 \Big) \tag{1.8}$$

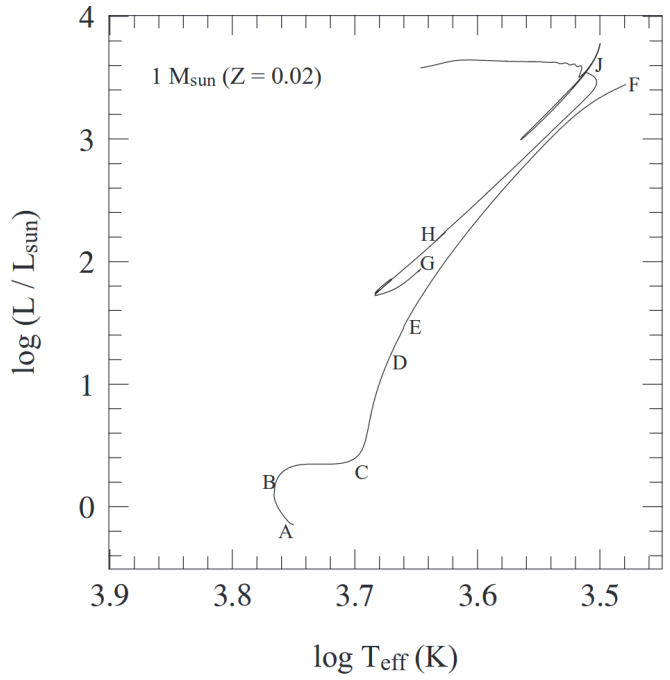

Figure 1.1: Evolutionary track along the HR diagram of a $1M_{\odot}$ star with metallicity $Z = 0.02$. The correlated paths along the HR diagram are: AB: Main Sequence (central H-burning), BC: Sub Giant Branch, CF: Red giant Branch, E: RGB bump, F: RGB tip, GH: Horizontal Branch (central He-burning), HJ: Asymptotic Giant Branch.

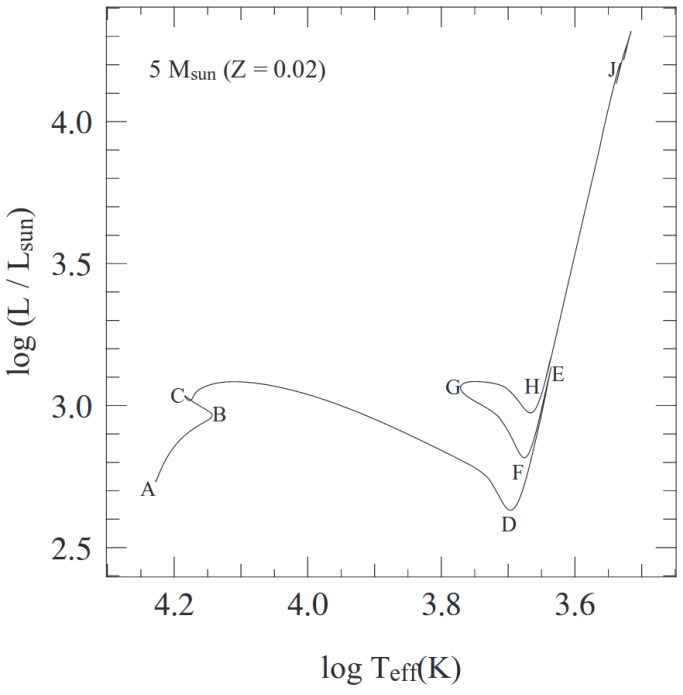

Figure 1.2: Evolutionary track along the HR diagram of a $5M_{\odot}$ star with metallicity $Z = 0.02$. The correlated paths along the HR diagram are: AB: Main Sequence (central H-burning), CD: Sub Giant Branch, DE: Red Giant Branch, EFGH: Blue Loop (central He-burning), HJ: Asymptotic Giant Branch.

1.2.1 Early AGB and Thermally Pulsing AGB phase

Early AGB phase. After the exhaustion of the central He-burning, all the regions below the H-burning shell contract until the activation of He-burning in a shell. From the *mirror principle* (i.e. the burning zones act as a 'mirror' provocating inverse behaviours between opposite regions) the core and the external envelope contract, while the inter-region between the two burning shells expands until it causes the exhaustion of the H-burning shell for the decreasing temperature. This long phase is called *early* AGB (E-AGB) phase and now the luminosity of the star is almost provided by the He-burning shell. The shell continues burning He and adding mass to the CO core which becomes degenerate due to the increasing density. The envelope expands and cool. At this point stars of sufficiently high mass ($M \geq 4M_{\odot}$) experience a second convective mixing episode, the *second dredge-up* (while the *first dredge-up* common to star of all masses was experienced during RGB phase): due to the expansion and the cooling of the outer layers, the convective envelope penetrates down into the He-rich regions, bringing to the surface He-rich and N-rich material (the latter produced by the CNO-cycle). Stars of lower masses do not experience the *second dredge-up* because they mantain a thin active H-burning shell which prevents a deep penetration of the convective envelope.

Thermally Pulsing AGB phase. At the end of the *second dredge-up* the stellar envelope contracts causing the re-ignition of the H-burning shell. Now a configuration of *double shell burning* can be seen: H and He shells are close together. The He-burning shell is thermally unstable and undergoes periodic *thermal pulses*, so this phase is called *Thermally Pulsing AGB* (TP-AGB) phase. The *thermal pulse cycle* is schematically the sequent: for most of the time the He-shell is inactive, while the H-burning shell continues producing and adding He to the intershell region (increasing pressure and temperature at the bottom). When a critical value for the core mass is reached, He is ignited in an unstable manner, giving rise to a thermonuclear runaway called *helium shell flash*. The large amount of released energy drives the convection in the intershell region, mixing the products of the 3α reaction and expanding and cooling the intershell region. Consequently, a phase of stable He-burning is reached while the H-burning shell is now estinguished. A further important consequence of the expansion and cooling of the intershell is the *third dredge-up* (3DU): a deep penetration of the outer convective envelope which bring to surface the products of He-burning, particularly ^{12}C. After the 3DU the H-burning shell is re-ignited and the He-burning shell becomes inactive again, until the occurence of the next thermal pulse. The occurence of the 3DU is related to two characteristic quantities:

- M_C^{min}: the minimum core mass for the onset of the 3DU;
- $\lambda = \frac{\Delta M_{dup}}{\Delta M_H}$: the efficiency of the 3DU, i.e. the ratio between the mass which is dredged up into the envelope and the mass by which the H-exhausted core has grown during the preceding interpulse period.

The *interpulse period* depends on the core mass. The *thermal pulse cycle* can repeat many times (and there can be also several 3DUs). This is schematically represented in Figure 1.3. Thermal instability grows in strength during the AGB evolution and the He-shell luminosity becomes larger and larger after each successive pulse reaching very high values ($\sim 10^8\ L_{\odot}$). It can be seen in Fig 1.4. TP-AGB phase will be the fulcrum of the following discussion.

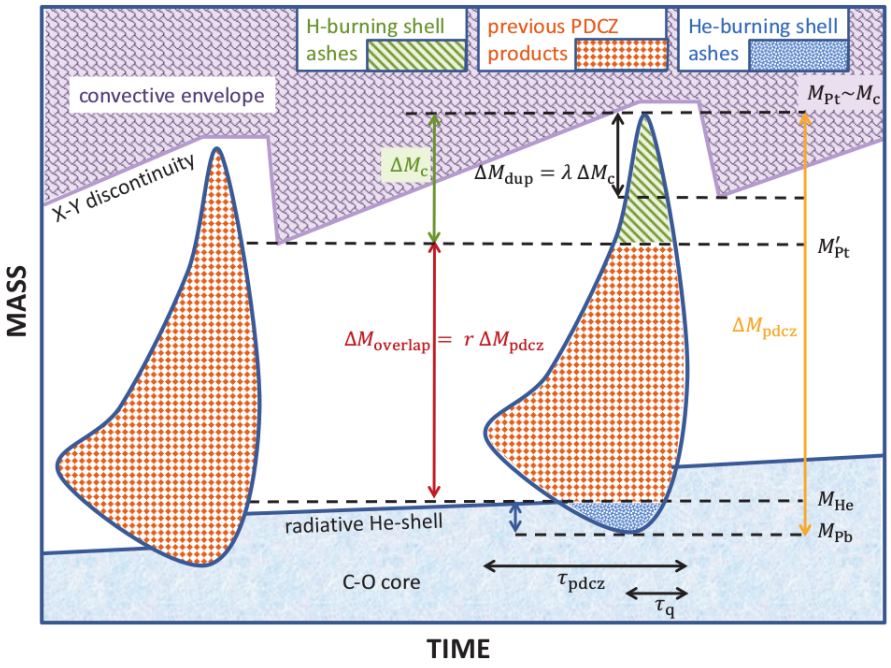

Figure 1.3: Schematical representation of a *thermal pulse cycle* (Marigo et al., 2013).

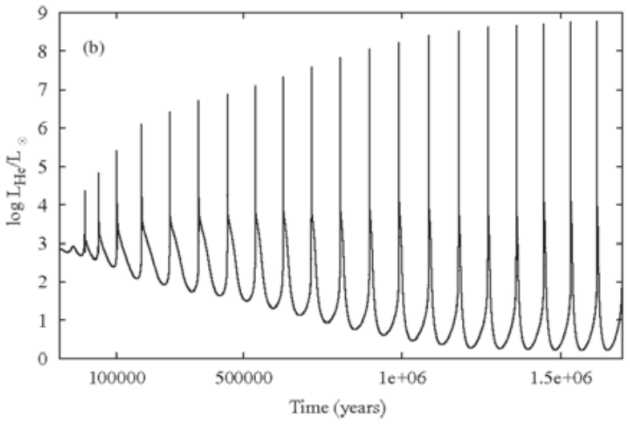

Figure 1.4: Behaviour of thermal pulses luminosity: He-shell luminosity grows in time.

Evolution of more massive stars is finally very different since they reach a sufficiently high temperature in their core to undergo a non degenerate C-ignition and they do not experience the AGB phase.

1.2.2 Importance of AGB phase

During the AGB phase there are several processes which have important effects on the subsequent evolution of the star and also on the interstellar medium, and whose evidence can be analyzed both photometrically and spectroscopically.

Nucleosynthesis of heavy elements

Production of heavy elements can continue via nuclear fusion in stars of sufficiently high mass until the synthesis of iron, ^{56}Fe, the most stable element (since it has the strongest binding energy). Elements heavier than iron can however be produced via different mechanisms, for example via neutron capture reactions. During AGB phase, elements heavier than iron are produced via neutron capture on Fe nuclei in the so called *s-process*: the process is *slow* if $\tau_{n-capture} \gg \tau_{\beta-decay}$, i.e. timescale for neutron capture is long compared to β-decay timescale. Obviously the *s-process* requires a source of free neutrons which can be produced in the He-rich intershell by both the H- and the He-burning regions; In particular the main reactions involved (for neutron production) in intermediate mass stars are:

$$^{13}\mathrm{C}(\alpha, n)^{16}\mathrm{O} \tag{1.9}$$

$$^{22}\mathrm{Ne}(\alpha, n)^{25}\mathrm{Mg} \tag{1.10}$$

while for the low mass star (up to $3M_{\odot}$) the main reaction is probably

$$^{13}\mathrm{C}(\alpha, n)^{16}\mathrm{O} \tag{1.11}$$

Once the neutrons are generated, *s-process* can take place: neutrons are captured by Fe to produce heavier elements (such as ^{57}Fe, ^{58}Fe, ^{59}Fe, up to ^{208}Pb and ^{209}Bi) through the relation

$$Fe + n \rightarrow s - elements \tag{1.12}$$

The *s-process* materials, as well as the carbon, are then mixed and brought to the surface by the next dredge-up.

Mass loss: enrichment of interstellar medium

Mass loss episodes are very important during AGB phase since the mass decrement determines the number of thermal pulses and hence the entire duration of TP-AGB phase. AGB stars suffer strong stellar winds: an infrared excess can be seen from the spectral energy distributions and many AGB stars (OH/IR stars) are enshrouded in a dusty circumstellar envelope invisible at optical wavelenghts. The episodes of such strong mass loss are conjectured to be driven by two main mechanisms, predominant at different evolution stages. Initially the stellar wind originates from magneto-acustic waves operating below the stellar chromosphere. This stage of mass loss is described semi-empirically by Schröder & Cuntz (2005). Later, mass loss is considered to be due to a combination of *pulsation* and *radiation pressure* on dust grains formed in the atmospheres, the so called

Pulsation-enhanced dust-driven wind scenario: AGB stars undergo strong radial pulsations inducing shock waves which can bring the gas to the condensation distance. If this limit is reached, gas can condensate in dust particles with a very high opacity and these grains are thus accelerated by radiation pressure producing dust-driven outflows (Bedijn, 1988). It is important to be careful of the fact that these episodes of mass loss are due to long period pulsation, not to thermal pulses. Mass loss rate can reach very high values ($10^{-4} M_{\odot}/yr$) and it is called *superwind*. Once an AGB star enters this phase, its H-rich envelope is rapidly removed and this marks the end of the AGB phase.

Surface abundances: C/O ratio

The most important effect of thermal pulses and particularly of the 3DU is bringing to the surface the newly synthetized elements. A particular attention has to be paid to the He-burning products, especially to carbon. A spectroscopic dichotomy can be found between oxygen (O) rich and carbon (C) rich AGB stars. These different spectral features can be described in terms of *C/O ratio*: the ratio between the number densities of the two elements. This happens because at the low temperatures of stellar atmospheres most of the atoms of C and O are bounded into a molecule of CO, while the remaining excess of one or the other element can give rise to other molecules. Initially we have a photospheric situation of C/O < 1, i.e. all the atoms of C are locked in the CO, while the remaining atoms of O form O-rich molecules and dust particles such as TiO, VO, H_2O and silicate grains. The AGB stars which present these features are classified as *M-type*. The repeated 3DUs bring to surface a certain amount of C and, at some point, the ratio becomes C/O > 1. In this case, all the O atoms are locked into CO, while the remaining C forms C-rich molecules and dust grains such as C_2, CN and carbonaceous particles like graphite. In this case the AGB stars are classified as *carbon stars* of *C-type*. The increment of C/O is not linear but it is discontinuous. When C/O ~ 1, AGB stars are classified as *S-type* stars. Besides carbon, suface abundances of many other elements and isotopes (produced via *s-process*) vary with time during TP-AGB phase.

A last important process has to be mentioned: the *Hot Bottom Burning* (HBB). This involves massive AGB stars ($M \geq 4{-}5 M_{\odot}$): during interpulse period temperatures become so high to induce H-burning at the base of the convective envelope via pp-chain and CNO-cycle. This causes an increment of the surface luminosity, but also a conversion of ^{12}C into ^{14}N, thus preventing massive AGB stars from becoming carbon stars. Beyond the H-burning, at high temperatures, there can be also the activation of other cycles such as $Ne - Na$ and $Mg - Al$ cycles whose products are then dredged-up to surface.

1.2.3 Uncertainties in AGB models

The study of AGB phase is important also in the perspective of analysis of several large systems, such as clusters or galaxies and, viceversa, the analysis of these systems can put constraints on parameters of AGB models. AGB phase (and in particular TP-AGB phase) is challenging to model. The main reason of difficulty is the duration of the TP-AGB phase which is quite fast (of the order of $\sim 10^6 yr$, even if this is one of the parameters to be constrained): this makes the statistical sample relatively poor when a system like a star cluster is analyzed. There are anyway many other sources of uncertainty, mainly due to the fact that the details of physical processes themselves (such as 3DU, nucleosynthesis, HBB, opacities) of the TP-AGB phase are still unclear. The most important sources of uncertainty are *mass loss mechanism* and *mixing mechanism*.

Mass loss. As already seen in the previous paragraphs, stars experience a dramatic mass loss during AGB phase. Mass loss mechanism is of fundamental importance since it is related both to the end and to the duration of TP-AGB phase. Beyond efforts to understand the detailes of the mechanisms involved, mass loss is difficult to be treated in models.

Mixing mechanism. This is a complex topic which involves several processes such as the difficult treatment of convection mechanism (e.g. through the *Mixing Lenght Theory*), of the possible presence of convective overshooting, the hypothesis of importance of rotational mixing (Endal & Sofia, 1976) and magnetic field (Spruit (2002) and MacDonald & Mullan (2004)).

It is therefore necessary to provide constraints for the parameters in AGB models and this is also the aim of this work. In order to calibrate TP-AGB models several targets can be chosen: field stars in Magellanic clouds (MCs), resolved galaxies with known star formation history (SFH) and star clusters. These last targets are of particular interest because their AGB stars have progenitor masses and metallicity known.

Chapter 2

AGB Stars in Star Clusters

2.1 Star Clusters

A *Star Cluster* (SC) can be defined, in general, as an overdensity of stars. Stars in a SC share a common motion in the galaxy, properties like a common distance, the same amount of interstellar absorption, the same age and metallicity (even if it will be seen that these last two conditions are valid just in first approximation). These properties translate into distinctive features in the HR diagram. A SC can be considered as a collisional autogravitating fluid of stars characterized by random motions.

2.1.1 Milky Way Globular and Open Clusters

Considering their basic properties, SCs in the Milky Way can be divided into two main groups: *Globular Clusters* (GC) and *Open Clusters* (OC). Their main differences and reference quantities are reported in Table 2.1. As can be seen, while the group of GCs

Table 2.1: List of the main differences between GCs and OCs.

	Shape	**Number of stars**	**Age**
GC	spherical	$10^4 - 10^5$	$10 - 13\ Gyr$
OC	irregular	$\sim 10^2$	$0.001 - 9\ Gyr$

has quite regular properties, OCs belong instead to a more variegated ensemble: they are younger and less populous than GCs, but with a wide spread in property range. This difference is reflected on *color-magnitude diagram* (CMD): GCs CMDs are essentially similar, while OC ones are very heterogeneous. Because of their irregularity, OCs are usually more challenging to study. However these differences hold mainly for Milky Way SCs, while in external systems they can be quite different. In particular, the *Magellanic Clouds* host a number of clusters as massive and spherical as the GCs, but as young as the OCs in the Milky Way.

2.2 Calibrating TP-AGB models

The main purpose of this work is to obtain a calibration of TP-AGB phase using star clusters in the *Magellanic Clouds*. Historically, these clusters have been used by many authors for this scope (see for example Frogel et al. (1990); Kamath et al. (2010); Pessev et al. (2008)). Because of their high intrinsic brightness, TP-AGB stars contribute significantly

to the total luminosity (L) of a *single stellar population* (SSP), and so they have a high importance in *stellar population synthesis* (SSP) models. Uncertainties in TP-AGB models can alter the $\frac{M}{L}$ ratio, hence the derivation of basic properties (e.g. the age) of galaxies, especially at high redshift. Moreover, these uncertainties dominate over observational errors. Different models thus provide conflicting results. There is the need to perform reliable calibrations of TP-AGB models.

2.2.1 Calibrating TP-AGB models: Magellanic Clouds Star Clusters

As already seen, SCs are ideal targets in order to study AGB phase. In particular, it is convenient to use Magellanic Clouds SCs because the distances of *Small Magellanic Cloud* and of *Large Magellanic Cloud* are well known and hence luminosity of AGB stars can be derived accurately (see for example Keller & Wood (2006)). Historically, calibrations relied on star counts, integrated fluxes and spectral classifications. More recently models have been expanded to take into account nucleosynthesis and pulsation. AGB models have to reproduce various observables, such as temperature, oxygen to carbon transition luminosity (i.e. $L_{C/O=1}$), AGB-tip L, period-luminosity relation, abundances. It is then possible to put constraints on poorly known quantities such as minimum core mass M_C^{min} and 3DU efficiency λ. A dramatic problem is arised from the fact that, using MC SCs as calibrators, when then TP-AGB models are applied to other external galaxies, they overstimate the contribution of TP-AGB stars also for comparable values of metallicity. Recently an interesting solution to this problem has been pointed out (Girardi et al., 2013): this overstimation is probably due to the *AGB boosting* (treated in the next paragraph).

The use of SCs as calibrators is affected also by a couple of limitations:

- the low number of TP-AGB stars is SCs: it brings to large Poisson fluctuations;
- the narrow sampling of the age-metallicity plane.

Beyond these problems, other complications have to be considered such as the uncertainty about SC age or the presence of *multiple stellar populations* (MSPs).

2.2.2 AGB boosting

TP-AGB models calibrated on MCs star clusters, when applied to *evolutionary population synthesis* models of galaxies, overstimate TP-AGB contribution. *AGB boosting* phase is a period in which the number of TP-AGB stars is not proportional to the cluster integrated light in optical passbands and it can be seen as a short-lived feature which cannot last much longer than 0.1 Gyr. The effect is the following: an abrupt change in He-core-burning lifetime causes a temporary boost in the production rate of subsequent evolutionary phase (AGB phase included). M_i can be plotted as a function of *age* (Figure 2.1). Fixed that an initial mass of $M_i \approx 1.75\ M_\odot$ is the limiting maximum mass to develope an electron degenerate He-core after MS, it can be seen that at $M_i \gtrsim 1.75\ M_\odot$ (i.e. condition under which electron degeneracy is no longer developed in the core before He-ignition) *central He-burning* lifetime gets longer. From the figure it can be also seen that the isochrone of $t \approx 1.6\ Gyr$ crosses three times the AGB phase: this means that stars with slightly different M_i experience this phase.

In this narrow range of parameters ($M_{TO} \sim 1.75\ M_\odot$ and $t \sim 1.6\ Gyr$) there are the most massive MC star clusters (with lots AGB stars) used to calibrated models.
Another important aspect to be considered is the contribution of integrated luminosity of TP-AGB stars to the integrated bolometric light of a SSP as a function of its age t.

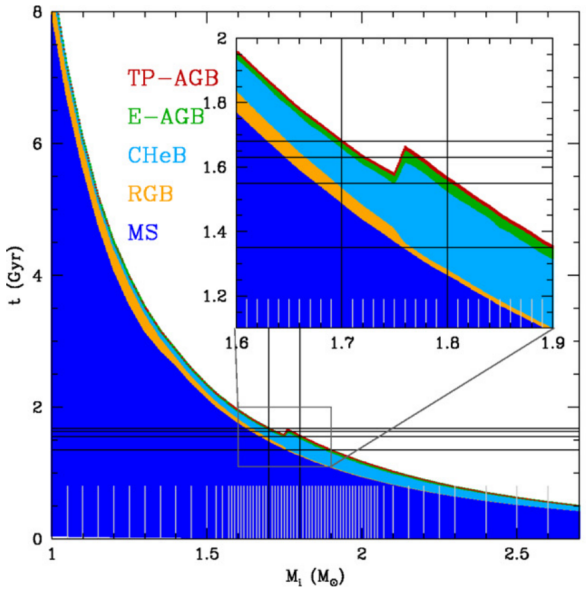

Figure 2.1: Initial mass as a function of age (inverse power-law relation). It can be noticed an increase of central He-burning lifetime (at least twice) for values of $M_i \gtrsim 1.75\ M_\odot$. Isochrones (orizonthal lines) of $t \approx 1.6 Gyr$ cross three times the AGB phase. (Image taken from Girardi et al. (2013)).

Figure 2.2 shows the typical feature of *AGB boosting*: for ages of $t \sim 1.6\ Gyr$ there is an increase of total integrated luminosity.

It must be pointed out that these results are obtained using the *Isochrone Method* (Charlot & Bruzual, 1991), while with the use of *Fuel Consumption Theorem* (FCT) approximation (Renzini & Buzzoni, 1986) there is no sign of *AGB boosting* period: this is due to the fact that FCT provides an incomplete description of light evolution of SSPs since it does not take into account changes of the central He-burning lifetime, hence any SSP can cross a given post-MS phase no more than once.

AGB boosting is likely the reason of the fact that TP-AGB contribution to the integrated light is biased toward too high values. In this perspective TP-AGB models based on intermediate-age MC clusters have to be revised. As an example, the SMC star cluster NGC 419 shows the favorable parameters in the narrow range described, necessary to undergo *AGB boosting* phaenomenon: it has an age of $t \sim 1.5\ Gyr$, a turnoff mass close to M_{HeF} (i.e. 1.75 $M_\odot$) and it shows multiple turnoffs and dual red clumps. All the detailes can be found in Girardi et al. (2013).

2.2.3 Critical Parameters

Two important parameters have to be primarily calibrated as a function of mass and metallicity of the stellar progenitor: *TP-AGB lifetimes* and *core-mass growth* during TP-AGB phase.

- TP-AGB lifetimes, τ_{TP-AGB}, are of paramount importance since they are related to the contribution to the integrated light of the system and to the number of TPs (hence to the chemical surface enrichment). A peak of τ_{TP-AGB} can be seen at $M_i \approx 2\ M_\odot$ (approximatively the critical stellar mass for the development of a

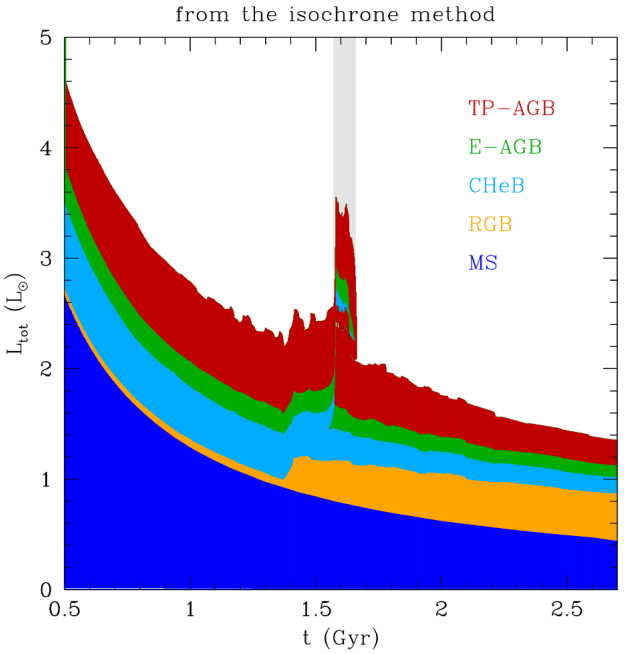

Figure 2.2: Evolution of integrated bolometric luminosity of a SSP as a function of age. For $t \sim 1.6$ *Gyr* (shadow area) it can been noticed the *AGB boosting period* (Image taken from Girardi et al. (2013)).

degenerate He-core). TP-AGB lifetimes are mainly determined by the efficiency of mass loss.

- Core-mass growth during TP-AGB phase is important because it is linked to the mass of the chemically enriched gas returned to insterstellar medium and it fixes a lower limit to the nuclear fuel burnt during TP-AGB phase. This parameter is affected mainly by mass loss and the 3DU.

Analyzing the theoretically-predicted distribution of the TP-AGB lifetime on the age-metallicity plane, there seems to be a particular region where TP-AGB stars are present in a considerable number: this means that the development of TP-AGB phase is favoured under certain conditions:

- A metallicity which varies from solar-like to MCs one;
- An age of $\sim$ few *Gyr* (i.e. an initial mass of $M_i \sim 1.5 - 2\ M_\odot$)

This region which emerges in the age-metallicity plane is called *TP-AGB island* and it is shown in Figure 2.3.

2.3 Small Magellanic Cloud and NGC 419

The *Small Magellanic Cloud* (SMC) is a dwarf irregular galaxy (dI) near the Milky Way. Its central coordinates are $\alpha = 00^h52^m44.8^s$ and $\delta = -72°49'43''$ (*NASA/IPAC Extragalactic Database* (NED)) and its distance is of $d = 60.6 \pm 1$ *kpc* corresponding to a true distance modulus of $(m - M)_0 = 18.91 \pm 0.03$ (Hilditch et al., 2005). The absolute magnitude of the SMC is $M_V \approx -16.2$ *mag* (Binney & Merrifield, 1998). The SMC has a central bar structure which leads to think that it was once a barred spiral galaxy then disrupted by

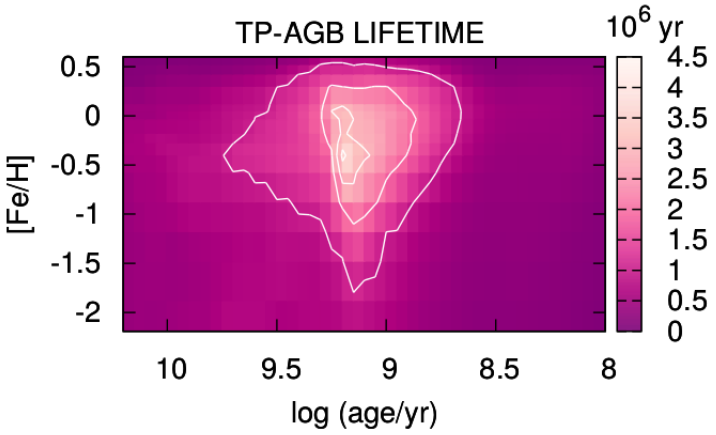

Figure 2.3: Map of TP-AGB lifetimes over the relevant age-metallicity plane occupied by TP-AGB stars (Marigo, in preparation).

Table 2.2: Main properties of NGC 419

Properties of NGC 419	
α (RA)	$01^h08^m17.79^s$ (*SIMBAD database*)
δ (DEC)	$-72°53'02.8''$ (*SIMBAD database*)
Metallicity	$[\frac{Fe}{H}] = -0.7 \pm 0.3$, $Z \approx 0.003$ (Kayser et al., 2009)
Age	$1.2 - 1.6 Gyr$ (Glatt et al., 2008)
	$1.3 - 1.5 Gyr$ (Girardi et al., 2009)
	$1.2 - 1.8 Gyr$ (Rubele et al., 2010)
Distance modulus	18.91 (Hilditch et al., 2005)
Reddening	$E(B-V) = 0.11$ (Glatt et al., 2008)
M_{ZAMS}	$1.90 M_\odot$ (Kamath et al., 2012)
M_{E-AGB}	$1.85 M_\odot$ (Kamath et al., 2012)
Pulsation Period	$790 d$ (Kamath et al., 2012)

the tydal interaction with the Milky Way.
Unlike the *Large Magellanic Cloud* which does not host star clusters in the age range $[4; 10]$ Gyr, SMC appears as the unique nearby dwarf galaxy with star clusters of all ages and of a wide range of metallicities. Star formation history of SMC is rather smooth and well-understood, with a high rate between 5 and 8 Gyr ago, and the metallicity increased from the early value of $[\frac{Fe}{H}] \approx -1.3$ for ages above 8 Gyr, to $[\frac{Fe}{H}] \approx -0.7$ presently (Dias et al., 2010).

NGC 419 is an intermediate-age, bright and populous cluster discovered in 1826 by James Dunlop and located to the east of the Small Magellanic Cloud (SMC) bar, in a region relatively poor of dust and of SMC field stars. Unlike other MC star clusters, NGC 419 contains a large number of TP-AGB stars, some of them with very high mass-loss rate. The main properties of this cluster are listed in Table 2.2, while the cluster and its CMD can be seen in Figure 2.4 in Figure 2.5.

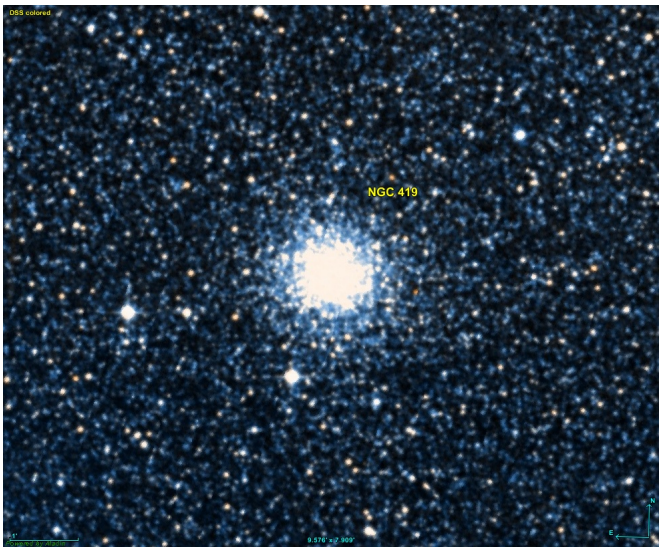

Figure 2.4: Image of NGC 419 taken from the *Digital Sky Survey* (DSS).

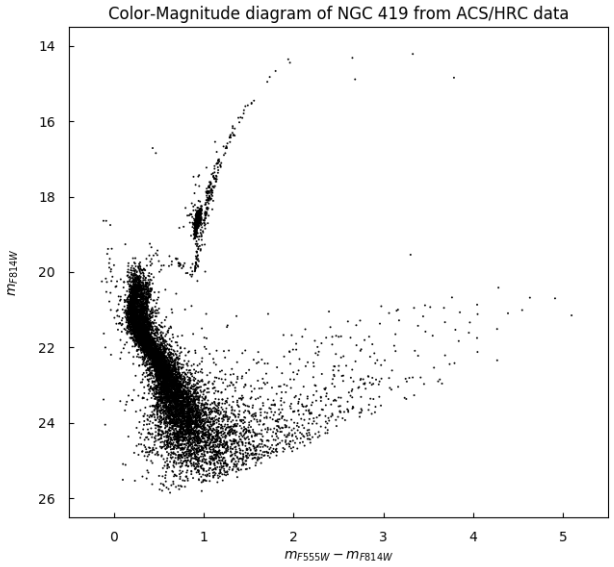

Figure 2.5: Color-Magnitude diagram of NGC 419. The data have been taken with the *High Resolution Camera* (HRC) of the *Advanced Camera for Surveys* (ACS) of the Hubble Space Telescope (HST). The magnitudes and the color are obtained with the filters *F555W* and *F814W*.

2.3.1 Photometrical features in CMD and interpretations

NGC 419 shows the presence of a broad MS such as of an extended main sequence turnoff (eMSTO) (noticed by Glatt et al. (2008)) and the presence of a dual red clump (Girardi et al., 2009).

Presence of dispersion in the Main Sequence

NGC 419 shows a clear spread in the distribution of the MS such as a broad turnoff.

- The explanation of these features was for a long time imputed to the presence of an age spread. A possibility to unfold the presence of spread in photometrical features of the MS is to consider a continuous, prolonged SFH, as suggested in Rubele et al. (2010): using the *CMD reconstruction* technique, they found a prolonged star formation lasting at least 700 Myr (from 1.2 to 1.9 Gyr) with a marked peak in the middle, for an age of ~ 1.5 Gyr. This hypothesis of a continuous star formation would be also able to explain the presence of the dual red clump, since an age spread of 700 Myr translates into ~ 0.26 $M_{\odot}$ spread in turnoff masses (i.e. ~ 0.01 $M_{\odot}$ spread in masses of H-exhausted cores) and this is enough to cause the appearence of a dual red clump. An accurate analysis (performed by Martocchia et al. (2017)) has demonstrated the absence of multiple stellar populations (MPs) in NGC 419 (populations of stars generated at different epochs). This consideration is based on the fact that no broadening is observed in RGB, i.e. no considerable spread in the chemical abundances of RGB stars is present. This can be immediately noticed in the *pseudo-color diagram*, if combination of different UV bands are plotted (as described in Piotto et al. (2015)). Many massive clusters in the Magellanic Clouds show the presence of MPs. Such evidence leads to consider the cluster total mass as the key property linked to the presence of MPs. The absence of MPs in NGC 419 leads to think that another important parameter could be the cluster age (that is, MPs are only observed in older clusters). Therefore the eMSTO is not due to the presence of MPs.

- Recently another possibility has been explored, basing on the fact that, if age spread was invocated to disentangle the question, this would lead to observational features not observed in the CMD of the cluster. In particular, the main inconsistence resides in the SGB morphology: SGB is too tight to be explained with a significant age spread. Moreover it is broader on the blue than on the red side (this phenomenon is called *converging* SGB). As suggested in Wu et al. (2016), the observed eMSTO and the SGB morphology might be due to rotation. In particular SGB morphology can be explained by rotational deceleration owing to the conservation of angular momentum during the evolutionary expansion of SGB stars. Stellar rotation affects the eMSTO area in two ways: through *gravity darkening*, i.e. luminosity and surface-temperature reduction due to the centrifugal force (which enlarges the eMSTO region) and through *rotational mixing*, which causes the increase of the size of convective cores and prolongs the MS lifetime. This hypothesis seems to be the most reliable since it permits to explain the broad features of the MS such as the tight SGB and the absence of spread in the RGB.

Presence of a Dual Red Clump

The red clump is a region of the HR diagram populated by stars which are in the central He-burning phase. This is visible in many OCs but also in some intermediate-age GC. NGC 419 shows an evident composite structure: a main compact red clump and a well delineated and fainter secondary red clump below it. It has been demonstrated that this secondary structure is an intrisic feature of the cluster and it is not due to the SMC field stars. The first panel of Figure 2.6 taken from Girardi et al. (2013) shows the stellar core mass as a function of initial mass. It can be noticed an abrupt drop of core mass around $M_i \sim 1.75\ M_\odot$: core mass passes rapidly from $\sim 0.45\ M_\odot$ to $\sim 0.33\ M_\odot$.

- Stars with lower initial masses ($M_i \lesssim 1.75\ M_\odot$) develope a degenerate He-core and undergo the He-ignition at higher core masses ($M \sim 0.47\ M_\odot$); their evolution is characterized by a well-pronounced RGB and then, in the Color-Magnitude diagram, they belong to a bright red clump (*main clump*).

- Stars with higher initial masses ($M_i \gtrsim 1.75\ M_\odot$) undergo the He-ignition in non-dege nerate conditions and at lower core masses ($M \sim 0.33\ M_\odot$); their evolution is characterized by a very short time spent in the RGB phase and, in the Color-Magnitude diagram, they belong to a faint red clump (*secondary clump*).

Core masses of NGC 419 stars after H-exhaustion do corresponds to a narrow range of initial masses, comprehending the transition between intermediate and low mass stars, M_{HeF}. NGC 419 is, therefore, a cluster in the condition of fast transition from classical to degenerate He-core.
This rare occurence of a dual red clump in a cluster permits to put stringent constraints on the age of the cluster and on other important quantities such as convective core overshooting: this parameter changes the relation between initial mass and H-exhausted core mass thus affecting M_{HeF} and t_{HeF}. It can be constrained the efficiency of the convective core overshooting Λ_C and it results a value of $\Lambda_C = 0.47^{+0.14}_{-0.04}$. All the detailes can be found in Girardi et al. (2009).
Moreover, if the presence of rotation is assumed, it contributes to further complicate the situation since it possibly change the star location on the CMD. However the effects of rotation on the CMDs usually focuse on the MS and SGB so a complete quantitative description is absent for later stages of evolution.

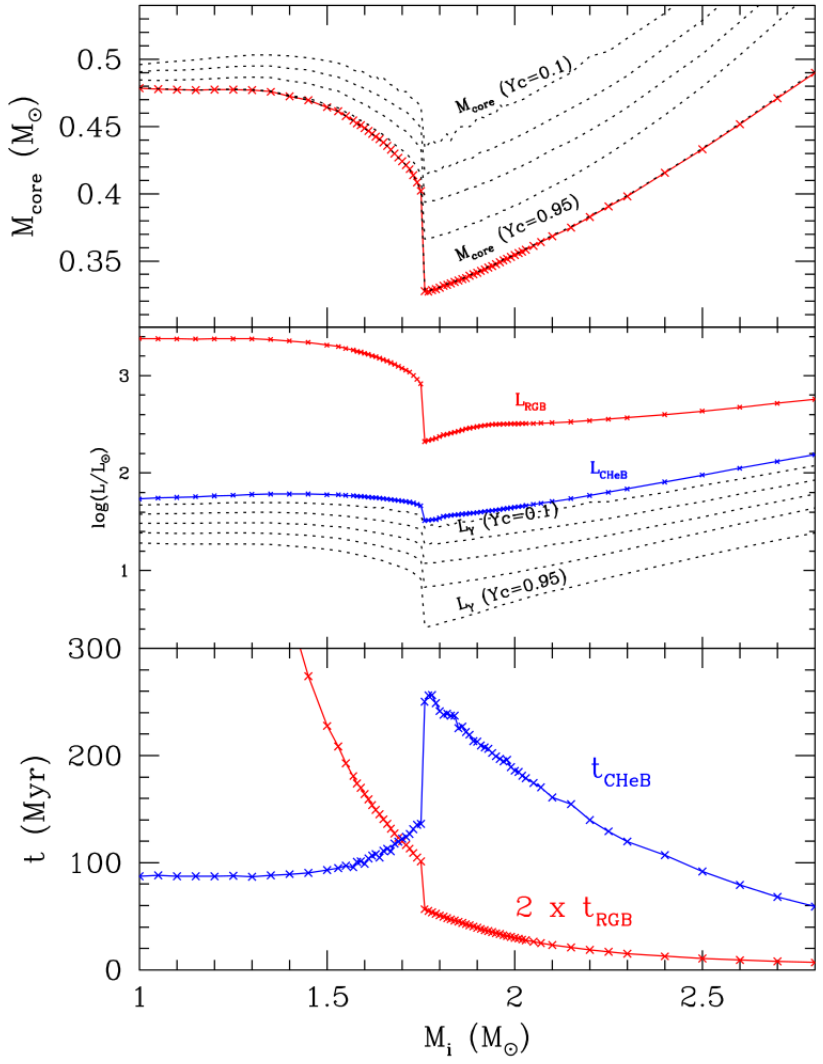

Figure 2.6: First panel: Core mass as a function of initial mass. Image taken from Girardi et al. (2009).

Chapter 3

Analyzing and simulating NGC 419

The aim of this work is to analyze the photometry of the cluster NGC 419, to reproduce the observed data with simulations in order to put constraints on the main physical properties especially about the AGB phase. First of all, Figure 3.1 shows the CMD of the cluster made with photometrical data taken by the camera *High Resolution Channel* (HRC) of the *Advanced Camera for Surveys* (ACS) installed in *Hubble Space Telescope* (HST), while Figure 3.2 shows the CMD of the cluster made with the data from the *Wide Field Channel* (WFC) of ACS. The latter CMD results to be more scattered due to contamination of field stars, since the observed region of sky is wider, while the former appears better delineated because HRC observes only the central region of the cluster. These data have been reduced by Girardi et al. (2009) and Goudfrooij (private communication). The two filters used here are F555W (centered on $\lambda = 535.5946\ nm$) and F814W (centered on $\lambda = 811.5338\ nm$), which closely correspond to the *Johnson-Cousins* V and I bands respectively. All the details about ACS/HRC and ACS/WFC photometry can be found in Sirianni et al. (2005) and Girardi et al. (2008).

3.1 The code `TRILEGAL`

`TRILEGAL` is a population synthesis code which generates stellar catalogs to simulate objects such as clusters or galaxies. It takes as input mass, distance, extinction, star formation history and age metallicity relation, with the possibility to include the Milky Way foreground population. A complete description can be found in Girardi et al. (2005). A general scheme of the code is shown in 3.3.

The continuous arrows refer to steps performed inside the `TRILEGAL` main code and subroutines; they lead to simulation of perfect photometric data (i.e. without errors). The dashed lines refer to optional steps usually performed with external scripts (such as the creation of catalogs with photometric errors). Stars in `TRILEGAL` are generated through a Monte Carlo simulation according to a probability distribution. For each star produced, star formation rate, age-metallicity relation and initial mass function are used to simulate the correspondent age, mass and metallicity. The absolute photometry is obtained via interpolation in a grid of evolutionary tracks or isochrones and it is converted to the apparent magnitudes using bolometric corrections, distance modulus and extinction. The main input datasets in `TRILEGAL` are:

- tables of stellar evolutionary tracks (which give their basic properties as a function

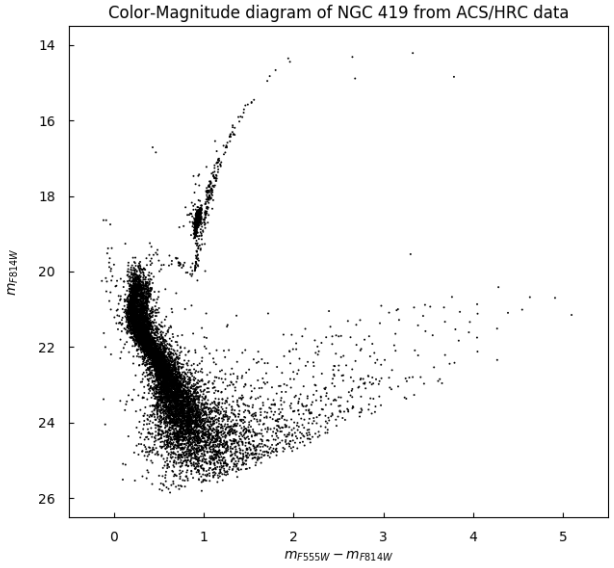

Figure 3.1: Photometry of NCG 419 in the two filters F555W and F814W from ACS HRC data.

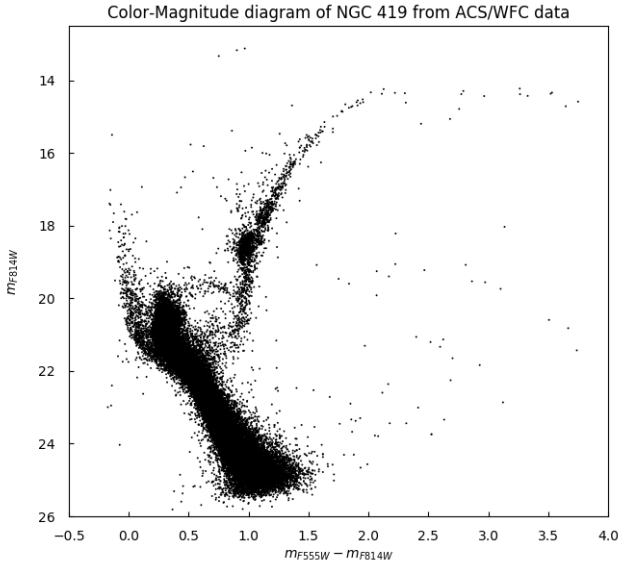

Figure 3.2: Photometry of NCG 419 in the two filters F555W and F814W from ACS WFC data.

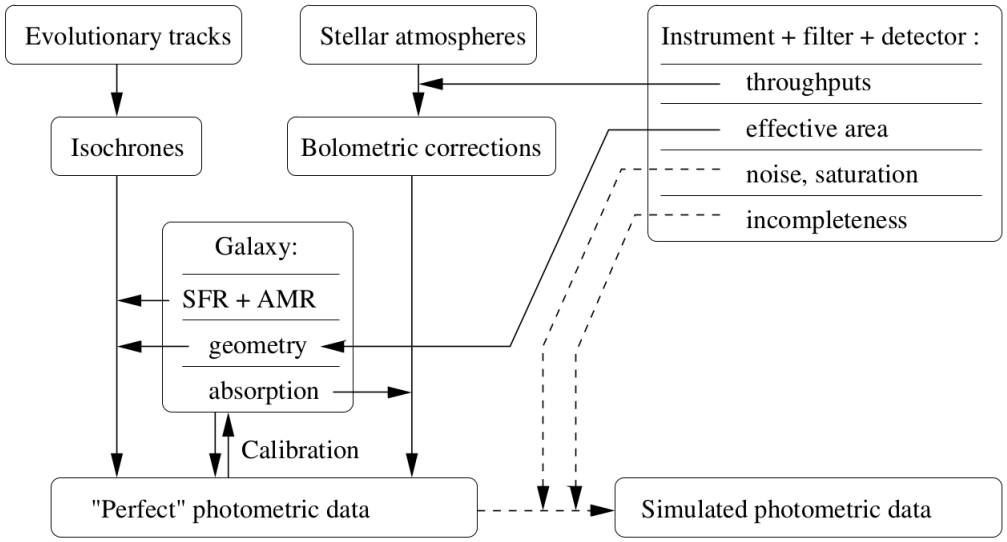

Figure 3.3: General scheme of `TRILEGAL` (Girardi et al., 2005).

of inital mass M_i, stellar age τ and metallicity Z);

- tables of bolometric corrections for the several filter pass-bands as a function of effective temperature T_{EFF}, gravity $\log g$ and metallicity [M/H], and the relative absorption with respect to V-band;
- the initial mass function IMF;
- the star formation rate SFR as a function of age, and the age-metallicity relation AMR;
- the geometry of Galaxy components.

In the next work the IMF used is the *Chabrier lognormal* IMF (Chabrier, 2003), the geometry of the Galaxy components is the simplest one (an object at a single distance), while the star fomation history will be determined in Section 3.3, and the `PARSEC` tracks used are described in Section 4.3.

3.2 Age of NGC 419

A way to determine the age of the cluster is to consider the *isochrone fitting*. An isochrone in the HR diagram is a line which connects stars of different masses but with the same age. Using isochrone fitting implicitly means to consider a well defined moment in which star formation took place, i.e. a *burst* of star formation. Even if this is just an approximation because many complications are present, just in order to have an estimation of the age of the cluster and to check its distance and metallicity it is convenient to make the isochrone fitting anyway.

The isochrone are generated with the code `TRILEGAL`. Theoretical isochrones have to be moved to the observational plane in order to be directly compared with the data. To do this is necessary to adopt some reference value:

- As first step it is necessary to fix the metallicity of the cluster. The reference value for the metallicity used in the next discussion is $[Fe/H] = -0.7 \pm 0.3$ *dex* (Kayser

et al., 2009) which translates in $Z = 0.003$ (for a solar metallicity of $Z_\odot = 0.0152$). The isochrones generated will have this value of Z.

- The reference value for the true distance modulus of the SMC used in the next discussion is $(m-M)_0 = 18.91\ mag$ (Hilditch et al., 2005) corresponding to $d = 60.5\ Kpc$. Since the magnitudes of the generated isochrones are absolute magnitudes, it is necessary to sum the true distance modulus to made them comparable with the data.

- The reference value for the extinction is $A_V = 0.15 \pm 0.02\ mag$ (Goudfrooij et al., 2014). Since the magnitudes used are m_{F555W} and m_{F814W}, it is necessary to obtain the extinctions in these bands:

$$A_{F555W} = 0.16\ mag \tag{3.1}$$

$$A_{F814W} = 0.09\ mag \tag{3.2}$$

  These values have to be added (together with the true distance modulus) to the isochrones magnitudes.

Once fixed these reference values it is possible to generate isochrones of different ages with `TRILEGAL`. Initially isochrones of different ages are generated starting from 1.2 Gyr up to 2.0 Gyr with a step of 0.1 Gyr. Since the most promising ages seem to be in the range $[1.3; 1.7]$ Gyr, it is convenient to explore better this set with a more accurate step of 0.05 Gyr. This is shown in Figure 3.4.

From this more accurate perspective, it can be seen that the best fitting isochrones are in the range $[1.45; 1.60]$ Gyr. If a zoom of the CMD of the HRC data is made (as shown in Figure 3.5), it can be cleary seen the broad features of the MS and of the turnoff.

As already discussed in the previous chapter, this effect might not be due to the presence of multiple stellar populations in the cluster or to an extended SFH, but to rotation. Even if the qualitative comprehension of the mechanism which induces the spread is quite clear, a quantitative treatment is still almost absent. Therefore the situation is complicated: dispersion seems not to be related to an age spread, and in the following discussion models do not treat rotational effects. For this reason, taking into account MS and turnoff features to find an isochrone which best fits the data to estimate the age of the cluster is a little arduous. So the fitting will be appproximate anyway.
In Figures 3.6 it can be seen the fitting with isochrones in the range [1.30; 1.60] Gyr of the region of upper MS, turnoff, sub giant branch and red clump.

As can be noticed, younger isochrones (e.g. 1.45 Gyr) better fit the lower part of the red clump (i.e. the so called *secondary clump*), while older ones better fit the MS and SGB regions (even if with the limits discussed above). Therefore, from isochrone fitting for NGC 419, it can be estimated an age in the range [1.30; 1.60] Gyr, in agreement with the values present in literature and reported in Table 2.2. The reference values for the cluster are summarized in Table 3.1. They will be used in the next discussion.

3.3 Star Formation History of NGC 419

As already seen in Section 2.3.1, CMD features (splitted MS, broad turnoff, dual red clump) can be explained by rotational effects. Since the models do not treat rotation, they will be modelled as being due to an age spread. However, instead of trying to fit the Main Sequence, we will concentrate in fitting the red clump. There is a good reason

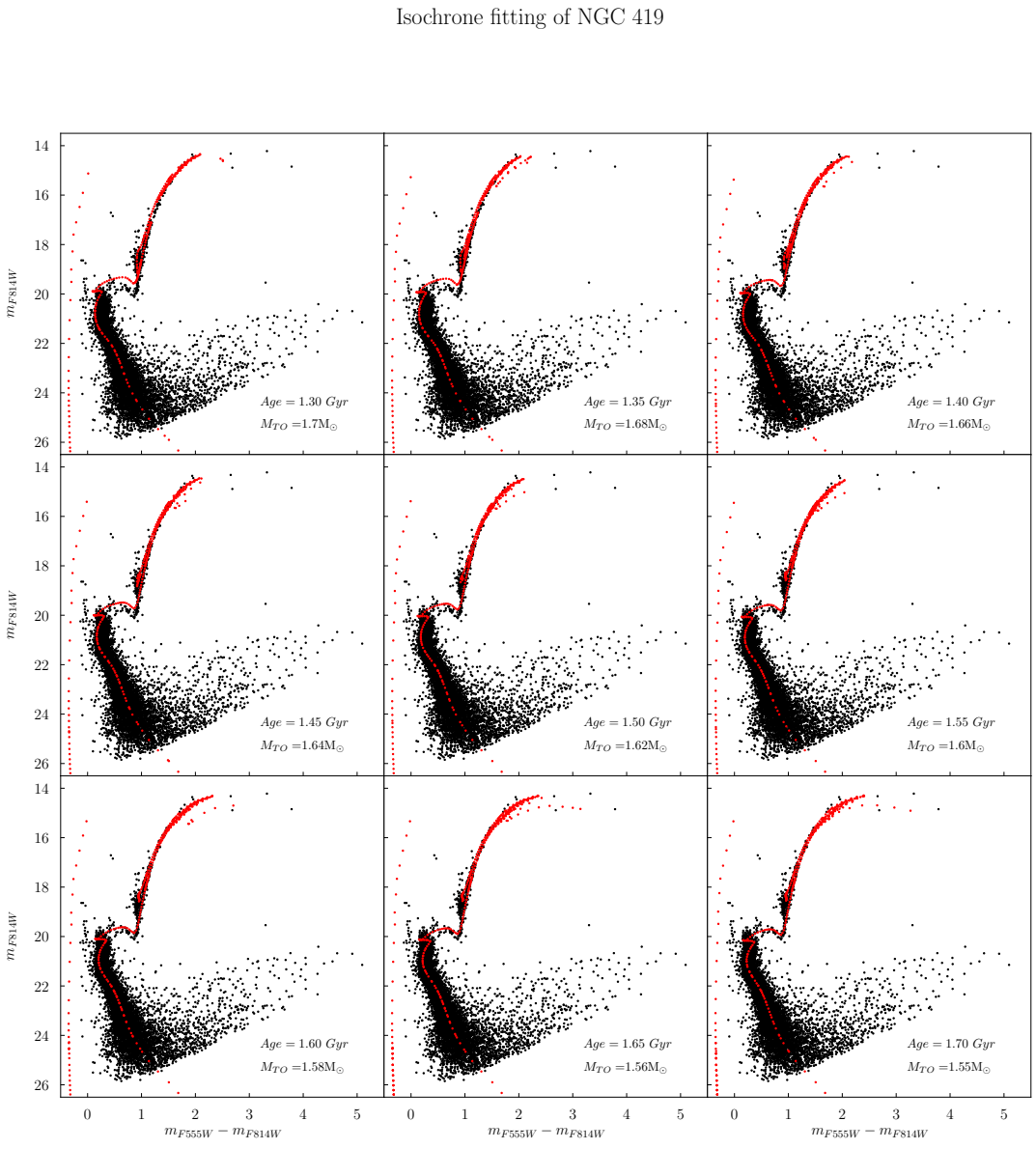

Figure 3.4: Fitting of NGC 419 with isochrones of ages in range $[1.3; 1.7]$ *Gyr* and with step of 0.05 *Gyr*. The parameters are: true distance modulus of 18.91 *mag*, metallicity $Z = 0.003$, extinction $A_V = 0.15$ *mag*. In the figures also the turn-off masses are reported.

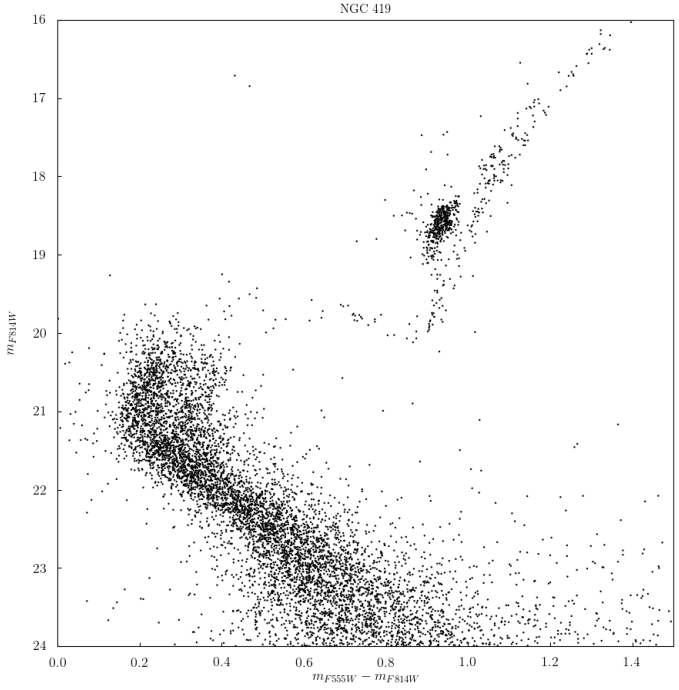

Figure 3.5: Zoom of the CMD from HRC data.

Table 3.1: Reference properties of NGC 419.

NGC 419: Reference Properties	
Metallicity	$[\frac{Fe}{H}] = -0.7 \pm 0.3,\ Z \approx 0.003$
True Distance modulus	18.91 mag
Extinction	$A_V = 0.15\ mag$
	$A_{F555W} = 0.16\ mag$
	$A_{F814W} = 0.09\ mag$
Age	$[1.30;\ 1.60]\ Gyr$

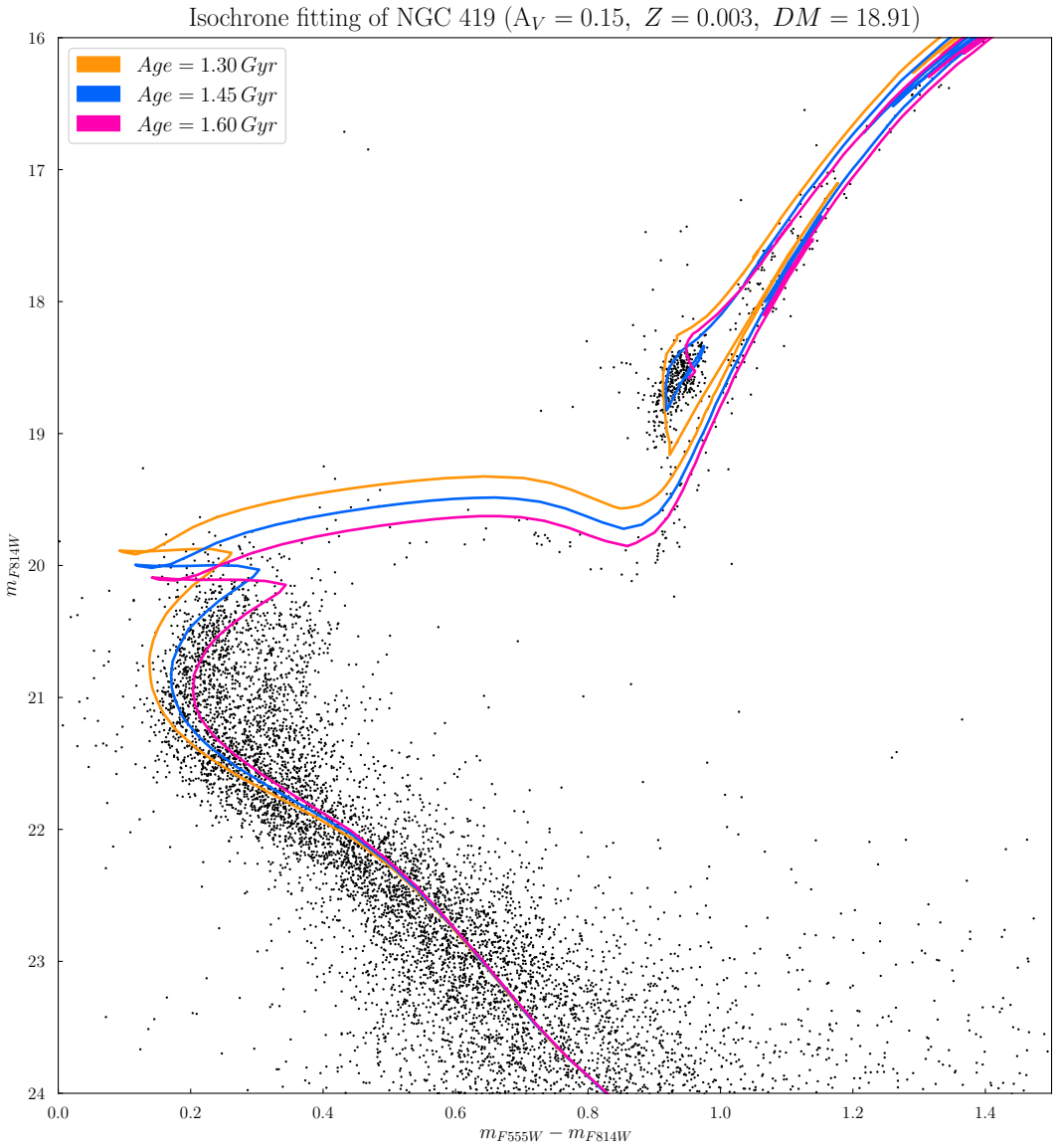

Figure 3.6: Zoom of the CMD from HRC data and the fitting isochrones in age range of [1.30; 1.60] *Gyr*.

to do this: what matters in order to discuss the AGB evolution is the core mass at the end of the central He-burning phase, and the distribution of core masses actually is what determines the distribution of luminosities at the red clump. It is therefore convenient to pay attention to the red clump region of the CMD and to try to reproduce the observed luminosity function (LF) in the two bands $F555W$ and $F814W$.

- For luminosity function in $F814W$ band, limits in the CMD are conveniently fixed in range [0.8; 1.05] for color $m_{F555W} - m_{F814W}$ and [18; 19.2] for m_{F814W} ;
- For luminosity function in $F555W$ band, limits are conveniently fixed in range [0.8; 1.05] for color $m_{F555W} - m_{F814W}$ and [19.2; 20.1] for m_{F555W}.

In order to study the LF of the red clump region it is necessary to adjust the mass value in the `triinput` file of `TRILEGAL` and the input star formation history (SFH) file.
As first attempt, it has been considered the simplest SFH: a step-shaped SFH in the age range of [1.3; 1.6] Gyr, roughly determined by the isochrone fitting. The initial constant star formation rate at different age bins has been then changed to better reproduce the observed LF. Some aspects have to be noticed:

- For age bins older than 1.6 Gyr the contribution does not better approximate the LF, so the age range previous determined is a good one;
- For other values of metallicity ($Z = 0.002$ and $Z = 0.004$) simulations does not produce a better fit, so the previous value of $Z = 0.003$ reveals to be a good choice;
- A true distance modulus of 18.934 mag (instead of the previous value of 18.91 mag) produces better simulations. This anyway agrees within the error with the true SMC distance modulus of 18.93 ± 0.024 estimated by Keller & Wood (2006) using Cepheid variables.

Several SFHs are used and the ones which produce best results are peaked around 1.45 Gyr (see Figure 3.8). A good extimation for the mass is the value of $M = 5.5 \times 10^4\ M_\odot$ (we recall that this value refers to the area framed by the HRC survey which corresponds just to a part of the cluster, as well shown in Figure 1 of Girardi et al. (2010), so to obtain the total mass of the cluster it will be necessary a further consideration. In order to produce more realistic outputs and to reduce effects of noise, simulations are done with a value of mass ten time higher and then the height of the bins in the LF is divided for ten. Moreover a mean of ten simuation has been considered. In the end to select the SFH for which simulations best approximate the observed LF, χ^2 is computed:

$$\chi^2 = \sum_i \frac{(N_{sim} - N_{phot})^2}{(1 + N_{phot})} \tag{3.3}$$

(here the normalization is $(1 + N_{phot})$ since the value of some luminosity bin is ~ 0 and to resolve the problem it would be otherwise necessary to reduce drastically the number of bins). The distributions in the two bands ($F555W$ and $F814W$) which turned out to has the lowest value of χ^2, are reported in Figure 3.7, while the relative SFH is reported in Figure 3.8. The general comparison between simulation and HRC data is shown in Figure 3.9.

A last important note has to be mentioned: in first approximation the SFH determines the shape of the LF, while the total mass regulates the height of the bins. In reality the two aspects are not completely uncorrelated: during the work has been necessary to modify repeatedly both the inputs to obtain the final fit.

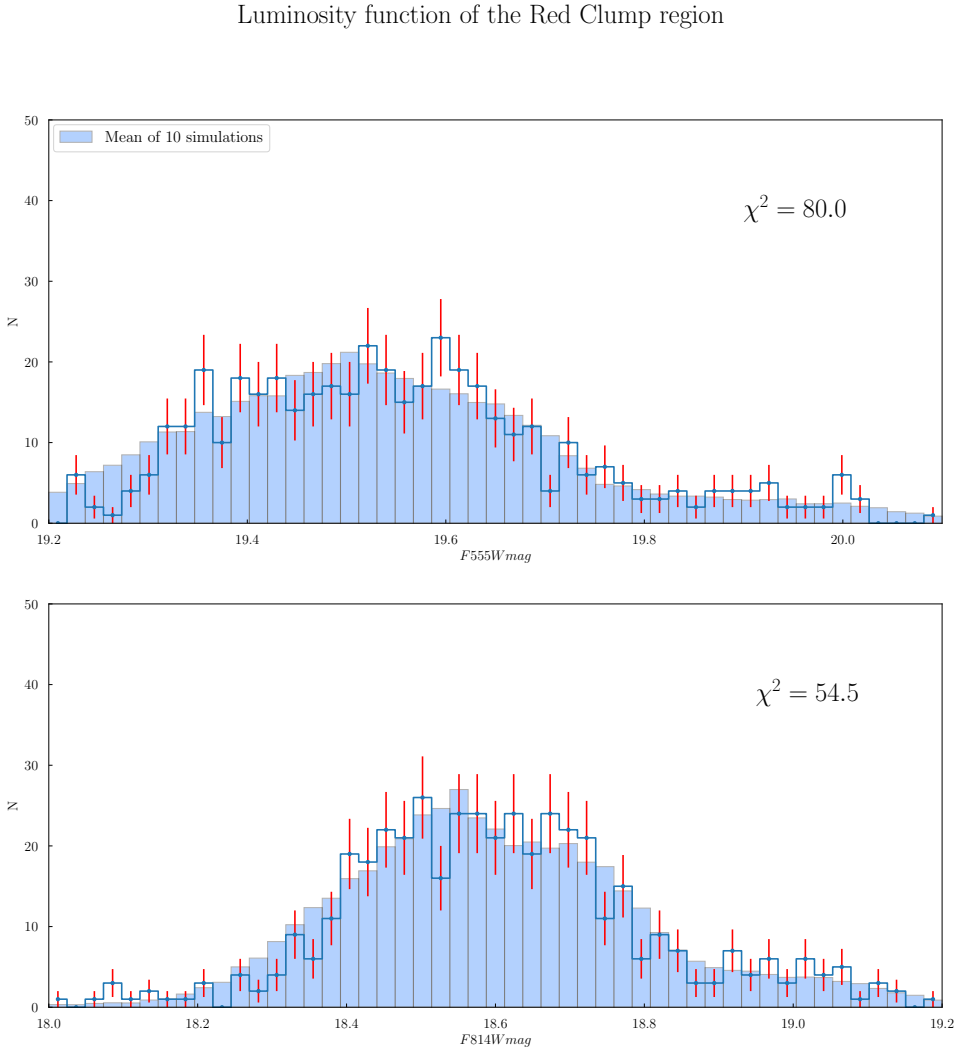

Figure 3.7: Comparison between luminosity function in the red clump region from HRC data (stacked) and simulation (barred) in the two filters $F814W$ (top) and $F555W$ (bottom). The error in photometry is poissonian, i.e. $\sqrt{N}$ where N is now the height of the bin. The simulations are done with a SFH in range [1.30; 1.60] Gyr, $\sigma(logz) = 0.065$, $z = 0.003$, $DM = 18.934$, $M = 5.5 \cdot 10^4\ M_\odot$.

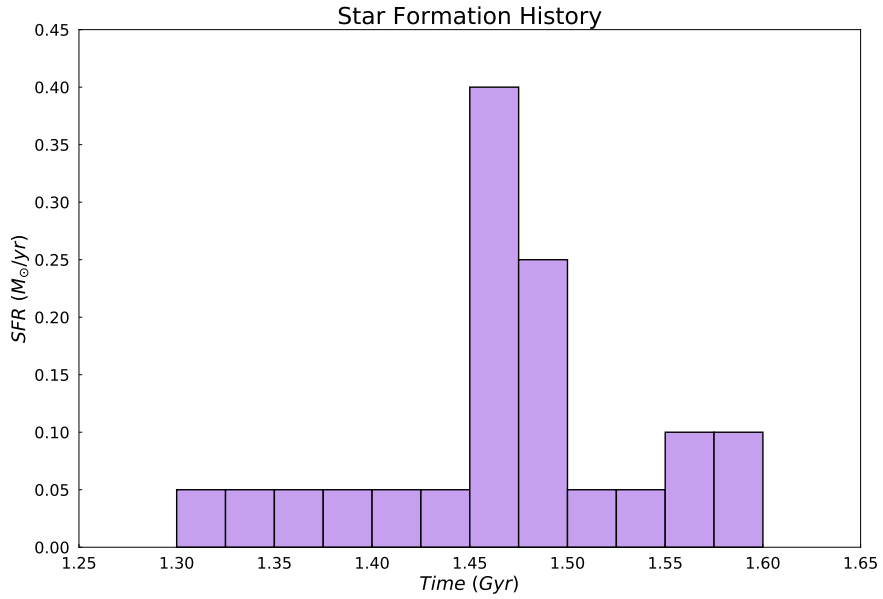

Figure 3.8: Star formation history in age range [1.3; 1.6] *Gyr* which produces the distribution with the lowest χ^2.

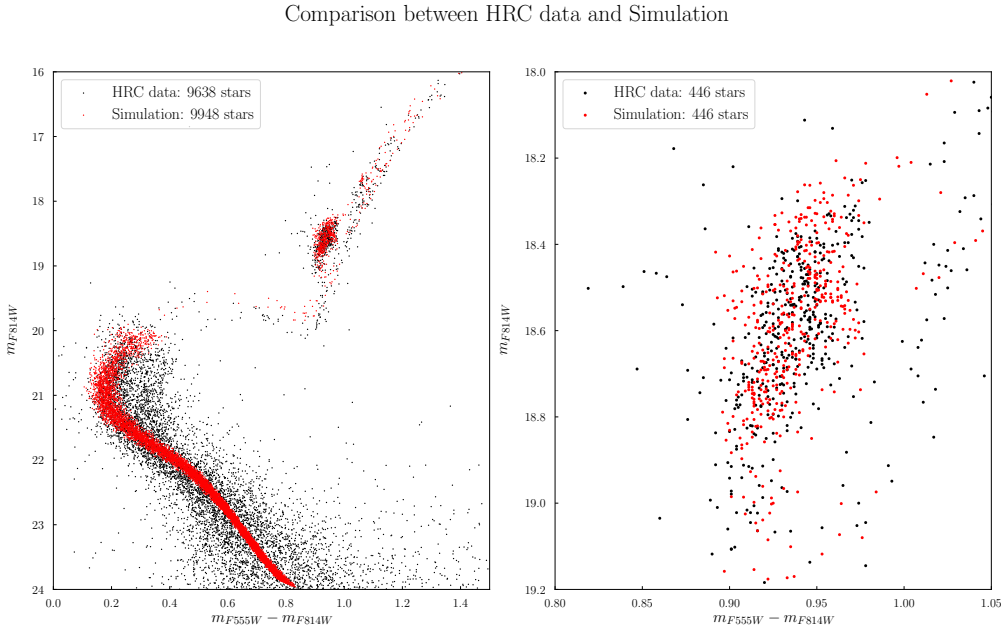

Figure 3.9: Comparison between simulation and HRC data in the whole CMD (left) and in the red clump region (right).

3.4 Total mass of NGC 419

Once fixed age and star formation history using the more detailed and less rumorous ACS/HRC data, in order to estimate the total mass of the cluster is now necessary to analyze the ACS/WFC data since they frame the whole cluster and not only a partial region.

At first, an important problem has to be noticed: when the two sets of data are compared together (for example in a CMD diagram) they result to be shifted one from the other along the abscissa. This fact has no physical explanation, and this is probably due to a mistake made during the calibration. Since the main aim of this work is not to obtain rigorously the properties of NGC 419 but to calibrate AGB models basing on them, it is sufficient to introduce, for the moment, a fictitious shift in color: $color - 0.04$. In this way the two set of data appeared to be perfectly overlapped. Hereafter *color* in ACS/WFC data will have always this shift.

The proceeding is now quite intuitive: the mass of a particular region is proportional to the counts in that region,

$$M_{HRC} \propto N_{HRC} \tag{3.4}$$

$$M_{WFC} \propto N_{WFC} \tag{3.5}$$

so, knowing the mass of HRC portion by the simulations, it is possible to derive the total mass of the cluster considering the ratio between the star counts in the two sets of data. As reference, it has been considered the not too contaminated region in the CMD, in range $color \in [-0.75\ ; 2]$ and $F814W \in [16;\ 21]$ as shown in Figure 3.10.

From a first rough comparison between counts, the expected proportional factor is ~ 3, so at first sight the total mass of the cluster is expected to be $M_{TOT} \sim 3 \times M_{HRC} \sim 1.65 \times 10^5 M_\odot$.

Obviously the counts have to be corrected for the contribution of field stars. In order to do that it is necessary to consider the *number density profile*: the number density (i.e. the number of stars per unit area) is expected to decrease with radius, getting away from the center, until a certain point where it remains constant as the radius increase. This constant value corresponds to background density, while the point beyond which density becomes constant establishes the end of the cluster. To obtain *number density profile* is a little tricky, since the ACS/WFC field is not simmetric and centered. Fortunately NGC 419 is quite circular (its ellipticity is very low), so to build the profile in a reasonable area, it is possible to consider only the right-down quarter highlighted in Figure 3.11.

The center of the cluster has been found by Goudfrooij. To visualize physical quantities, distance in pixel has been converted into $arcsec$ and then into $parsec$ through the relations:

$$d_{arcsec} = d_{pixel} \cdot 0.04 \tag{3.6}$$

$$d_{parsec} = d_{cluster} \times tan\Big(\frac{d_{pixel} \cdot 0.04}{206265}\Big) \tag{3.7}$$

being 0.04 the dimension of each pixel (in $arcsec$) in ACS/WFC3, and

$$d_{cluster} = 10^{\frac{18.934+5}{5}}\ pc \tag{3.8}$$

where 18.934 is the distance modulus previously estimated.

The *number density profile* is built considering the number of stars in circular annuli of width of 1 pc, while the error bars are made considering the poissonian error $\sqrt{n}$ (where n is the height of the bin). The resulting plot can be seen in Figure 3.12.

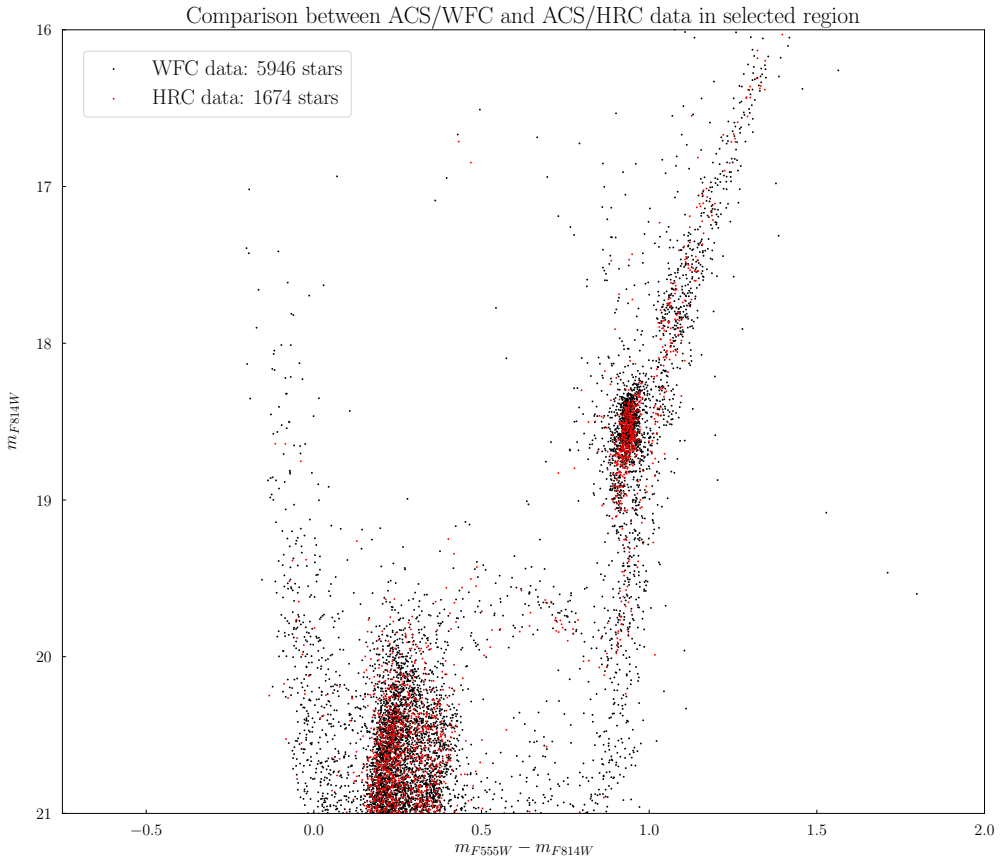

Figure 3.10: Comparison between ACS/HRC and (shifted) ACS/WFC data in the region taken as reference. Star counts in this region is also reported.

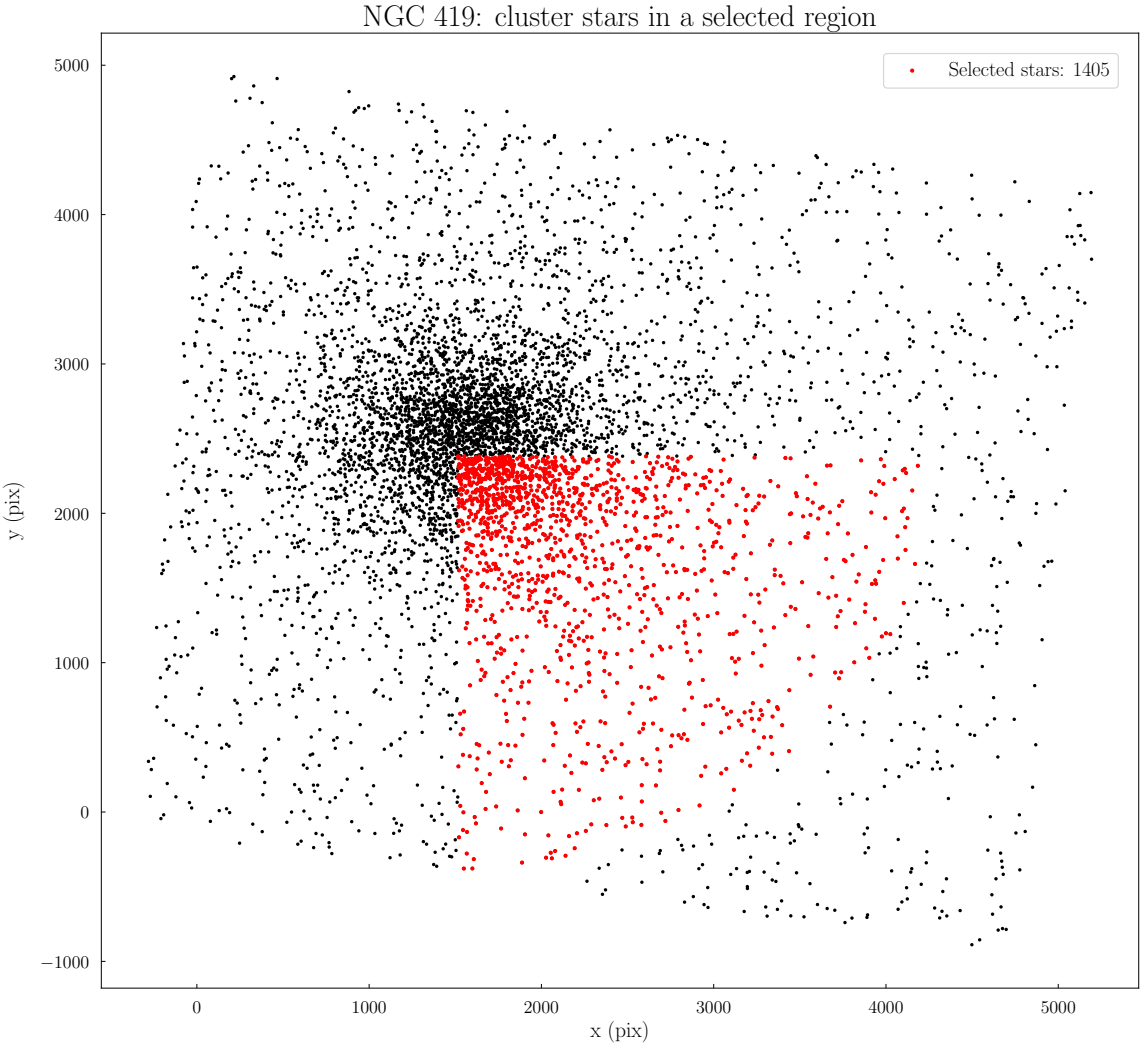

Figure 3.11: Spatial distribution of stars in NGC 419. Only stars in range $color \in [-0.75;\ 2]$ and $F814W \in [16;\ 21]$ are plotted. The red points correspond to stars in the selected area, used to build the *number density profile*.

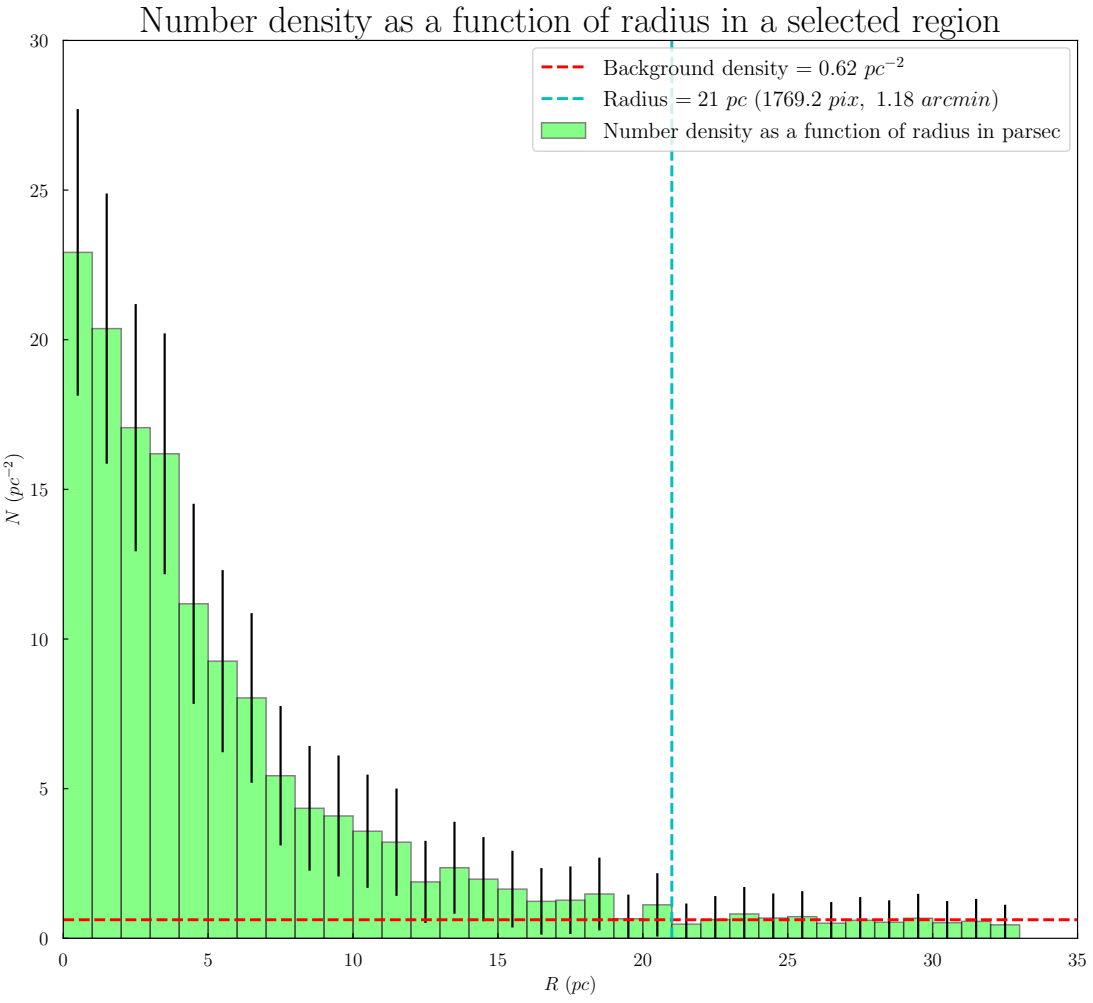

Figure 3.12: Behaviour of number density as a function of radius in NGC 419. As can be seen, the trend becomes flat: this represents the background density, while the point corresponding to the flattening fixed the end of the cluster. The horizontal line corresponds to the background density, while the vertical one corresponds to the radius of the cluster

It is immediately evident that the number density flattens at a certain point. To estimate rigorously the background density, a weighted average has been done: only the bins with height ≤ 1.2 (i.e. 1.2 stars per unit area) are taken into account and they are weighted inversely proportionally to their poissonian error, according to the relation:

$$Bg = \frac{\sum_i (V_i \times W_i)}{\sum_i W_i} \tag{3.9}$$

where the values V are the heights of the bins and the weights W are the inverse poissonian errors $1/\sqrt{n}$. The error on the weighted mean is computed in the following way:

$$\sigma_p = \sqrt{\frac{1}{\sum_i \sigma_i}} \tag{3.10}$$

where $\sigma_i = \frac{1}{\sqrt{n}}$. The result is a background density of

$$Bg = (0.62 \pm 0.24)\ pc^{-2} \tag{3.11}$$

The radius of the cluster is fixed as the point beyond which the height of the bins does not overcome of more than 10% the value of background density, and it results to be

$$R = 1769.2\ pixel = 1.18\ arcmin = 21\ pc \tag{3.12}$$

Once determined the border of the cluster, it is finally possible to estimate the total mass of the cluster considering the relation

$$M_{TOT} = \frac{N_{TOT}}{N_{HRC}} \times M_{HRC} \tag{3.13}$$

The proportional factor is obtained from the ratio between the star counts in ACS/WFC and ACS/HRC in the selected region of $color \in [-0.75;\ 2]$ and $magnitude \in [16;\ 21]$ previously seen, corrected now for the contribution of background stars (obtained multiplying the background density for the area of the two surveys) through the relation:

$$f = \frac{N_{TOT(\leq 21pc)} - (0.62 \times A_{TOT})}{N_{HRC} - (0.62 \times A_{HRC})} = \frac{4744 - [0.62 \times (\pi(21)^2)]}{1674 - (0.62 \times 66.4)} = 2.38 \pm 0.19 \tag{3.14}$$

Now the total mass can be finally estimated multiplying the HRC mass for this proportional factor:

$$M_{TOT} = (1.31 \pm 0.11) \cdot 10^5 M_\odot \tag{3.15}$$

Both the errors of the proportional factor f and of the total mass M_{TOT} have been computed with the propagation of uncertainties. This value obtained for the total mass of the cluster will be, hereafter, the reference value used in simulations.

Chapter 4

Calibrating TP-AGB models

4.1 AGB stars in NGC 419

Once the parameters of the cluster NGC 419 are obtained (estimation of the age, star formation history, total mass) considering optical ACS/HRC and ACS/WFC data, the next work consists of finding the best TP-AGB models to reproduce the observed properties of AGB stars of the cluster. In order to do that IR data of AGB stars are taken into account. In Kamath et al. (2010) AGB variables of NGC 419 are analyzed. Since in simulations all stars above a certain magnitude limit (RGB tip) and not only the variable ones will be taken into account, a complete catalog is needed. The complete list of AGB stars and their spectral types are reported in Table 4.1 (together with the reference papers), the magnitudes are reported in Table 4.2, together with the equatorial coordinates right ascension (RA) and declination (DEC) taken from `SIMBAD` database. For the stars present in Kamath et al. (2010) paper, the J and K magnitudes used are the ones from the near-IR imaging system *Cryogenic Array Spectrometer/Imager* (`CASPIR`) photometry: They are the most reliable values because they take into account mean flux-averaged photometric magnitudes and not only the value at a certain instant of time. For all the other stars reference magnitudes are the ones from `2MASS` photometry. In Table 4.1 stars in the first group are the AGB variables from Kamath et al. (2010), all the stars at the bottom are from Frogel et al. (1990). The relative spatial distribution of TP-AGB stars can be seen in Figure 4.1. The only star which an uncertain identification, present in Kamath et al. (2010), is the extremely red MIR1 (MIR1 010817.47-725309.5). This pulsating star is a IR source with a large mass-loss rate. Its coordinates are very close to the ones of IR2 which is instead bluer. Since photometry of MIR1 is not complete in Kamath et al. (2010), it has not been taken into account in this work. Distribution of TP-AGB stars in the CMD diagram, can be seen in Figure 4.2. The bands used hereafter are the infrared J (1.28 μm) and K (2.22 μm). The value for *RGB tip* (12.6 mag) is taken from Boyer et al. (2011).

As already seen, initially stars have a carbon-to-oxygen ratio $C/O < 1$ (these are called *M-stars*). Then the repeated *third dredges up* bring to surface a certain amount of C and carbon-to-oxygen ratio exceeds unit. Stars with $C/O > 1$ are classified as *carbon stars* (*C-stars*). As can be seen from the CMD in Figure 4.2, C-stars are redder and more luminous than M-stars.

Table 4.1: AGB stars of NGC 419: different names, ID and spectral types.

Ident	ID	SpT
LE16	OGLE 010801.10-725 17.1 2MASS J01080114-7253173	C (Kamath et al., 2010)
ADQR1/RAW 1544	OGLE 010810.31-725 307.6 2MASS J01081036-7253078	C (Kamath et al., 2010)
LE20/ARP V-39	OGLE 010811.55-725314.7 2MASS J01081158-7253148	C (Kamath et al., 2010)
LE21	OGLE 010812.36-725315.5 2MASS J01081240-7253157	C (Kamath et al., 2010)
IR1	OGLE 010812.92-725243.7 2MASS J01081296-7252439	C (Kamath et al., 2010)
5-3/ARP V-3/W84	OGLE010814.58-725356.7 2MASS J01081461-7253570	M (Kamath et al., 2010)
LE25/ARP VI-5/FMB4	OGLE 010815.63-725251.6 2MASS J01081568-7252520	C (Kamath et al., 2010)
LE24/ARP VI-4	OGLE010815.73-725254.3	M0 (Lloyd Evans, 1983)
LE35	OGLE 010817.45-725301.1 2MASS J01081749-7253013	C (Kamath et al., 2010)
LE37	OGLE 010819.40-725312.0 2MASS J01081940-7253121	C (Kamath et al., 2010)
LE36	OGLE 010819.80-725259.0 2MASS J01081985-7252593	C (Kamath et al., 2010)
LE27	OGLE 010820.61-725251.7 2MASS J01082067-7252519	C (Kamath et al., 2010)
LE28/ARP V-20/BR4 FMB19/RAW1550	OGLE 010821.50-725216.0 2MASS J01082155-7252161	C (Kamath et al., 2010)
LE23	OGLE 010821.67-725302.7	C (Kamath et al., 2010)
LE22	OGLE 010822.23-725302.3	C (Kamath et al., 2010)
LE29/ARP V-18/BR5 FMB18/RAW1552	OGLE 010822.28-725233.5 2MASS J01082231-7252337	C (Kamath et al., 2010)
LE19/ARP V-13	OGLE 010823.43-725318.2 2MASS J01082347-7253183	M (Kamath et al., 2010)
5-15/FMB14/ARP V-15	OGLE 010823.80-725309.4 2MASS J01082384-7253094	M (Kamath et al., 2010)
LE18/BR6	OGLE 010824.89-725256.7 2MASS J01082495-7252569	C (Kamath et al., 2010)
IR2 (MIR1?)	SSTISAGEMA J010817.51-725309.2 (MIR 010817.47-725309.5 ?)	C (Kamath et al., 2010)
TLE33/ARP VI-2	2MASS J01082087-7252479	M0 (Lloyd Evans, 1983)
TLE26/ARP VI-3	2MASS J01081796-7252525	M1 (Lloyd Evans, 1983)
TLE31/ARP V-6	2MASS J01082050-7253284	K (Lloyd Evans, 1983)
TLE30/ARP V-7	2MASS J01081924-7253376	K5 (Mould & Aaronson, 1980)
TLE34	2MASS J01082699-7252467	K5 (Lloyd Evans, 1983)
ARP VI-1	2MASS J01081843-7253230	K (Bessell et al., 1983)
LEB32	2MASS J01083685-7253398	C (Bessell et al., 1983)
LEB1	2MASS J01083702-7252227	AB (Boyer et al., 2011)
LEA31	2MASS J01084575-7253012	AB (Boyer et al., 2011)

Table 4.2: Main properties of AGB stars of NGC 419: magnitudes and equatorial coordinates.

Ident	J	K	RA	DEC
LE16	13.96	11.08	01h 08m 01.14s	$-72°53'17''.4$
ADQR1	13.87	12.56	01h 08m 10.37s	$-72°53'07''.8$
LE20	12.56	11.00	01h 08m 11.59s	$-72°53'14''.9$
LE21	12.67	10.90	01h 08m 12.401s	$-72°53'15''.76$
IR1	13.56	10.80	01h 08m 12.97s	$-72°52'44''.0$
5-3	12.91	11.95	01h 08m 14.595s	$-72°53'57''.24$
LE25	12.59	11.11	01h 08m 15.689s	$-72°52'52''.03$
LE24	13.15	12.02	01h 08m 15.70s	$-72°52'54''.3$
LE35	12.52	10.86	01h 08m 17.49s	$-72°53'01''.3$
LE37	12.77	11.56	01h 08m 19.407s	$-72°53'12''.16$
LE36	12.55	10.71	01h 08m 19.860s	$-72°52'59''.33$
LE27	12.52	10.89	01h 08m 20.67s	$-72°52'52''.0$
LE28	13.23	11.53	01h 08m 21.55s	$-72°52'16''.2$
LE23	12.83	11.23	01h 08m 21.73s	$-72°53'03''.0$
LE22	12.78	11.06	01h 08m 22.29s	$-72°53'02''.6$
LE29	12.74	11.24	01h 08m 22.31s	$-72°52'33''.7$
LE19	13.38	12.34	01h 08m 23.479s	$-72°53'18''.39$
5-15	13.39	12.33	01h 08m 23.85s	$-72°53'09''.4$
LE18	12.82	10.93	01h 08m 24.95s	$-72°52'56''.9$
IR2	14.41	13.58	01h 08m 17.47s	$-72°53'09''.23$
LE33	13.174	11.89	01h 08m 20.880s	$-72°52'47''.96$
LE26	12.724	11.658	01h 08m 17.963s	$-72°52'52''.55$
LE31	13.635	12.591	01h 08m 20.505s	$-72°53'28''.45$
LE30	13.52	12.446	01h 08m 19.248s	$-72°53'37''.6$
LE34	13.668	12.631	01h 08m 26.995s	$-72°52'46''.70$
6-1	13.168	12.174	01h 08m 18.431s	$-72°53'23''.01$
LEB32	12.923	11.684	01h 08m 36.836s	$-72°53'39''.85$
LEB1	13.613	12.562	01h 08m 37.027s	$-72°52'22''.77$
LEA31	13.538	12.481	01h 08m 15.67s	$-72°53'01''.20$

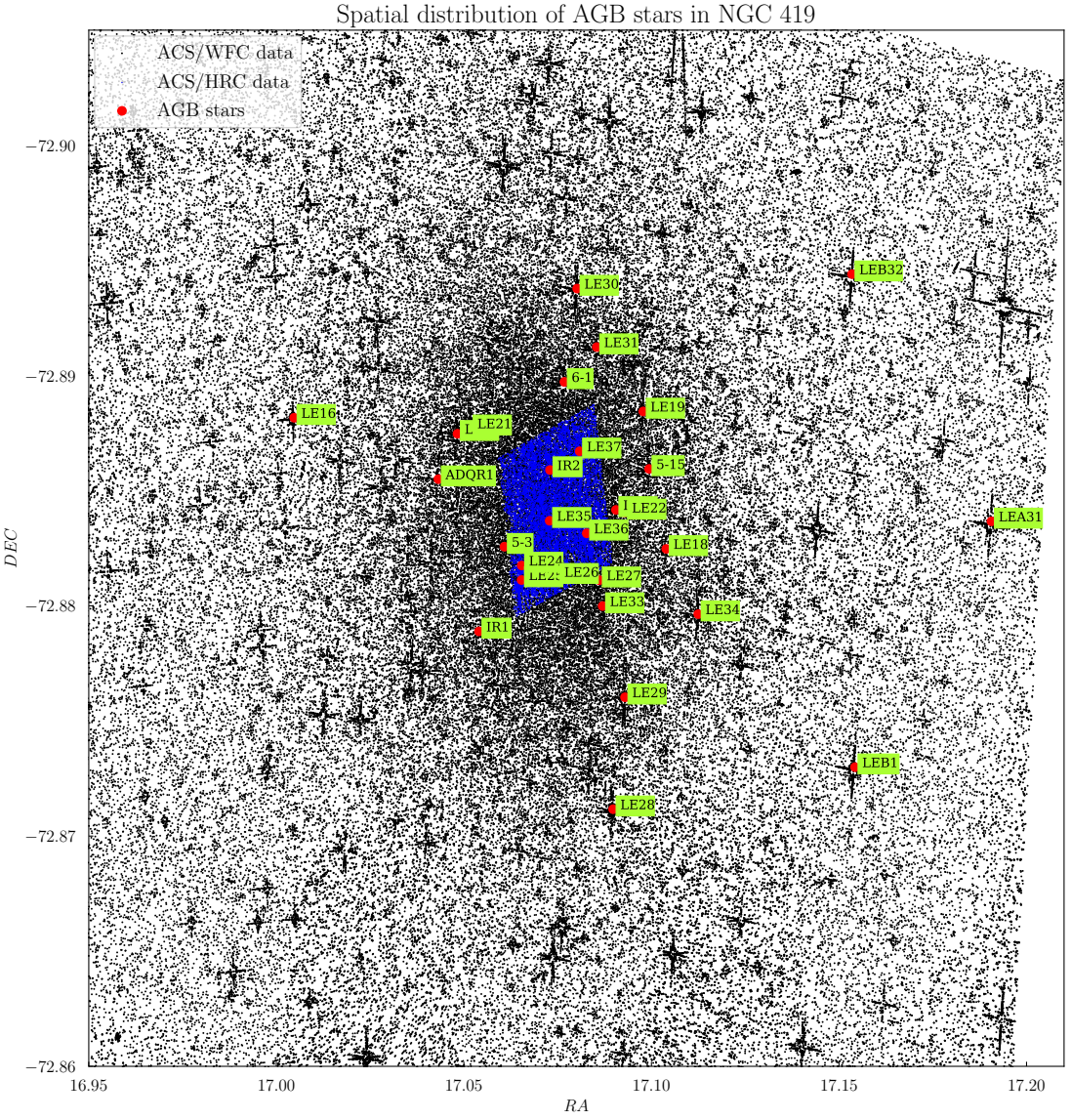

Figure 4.1: Spatial distribution of AGB stars of the cluster (red points). Black points are ACS/WFC data while the blue central region represents ACS/HRC data.

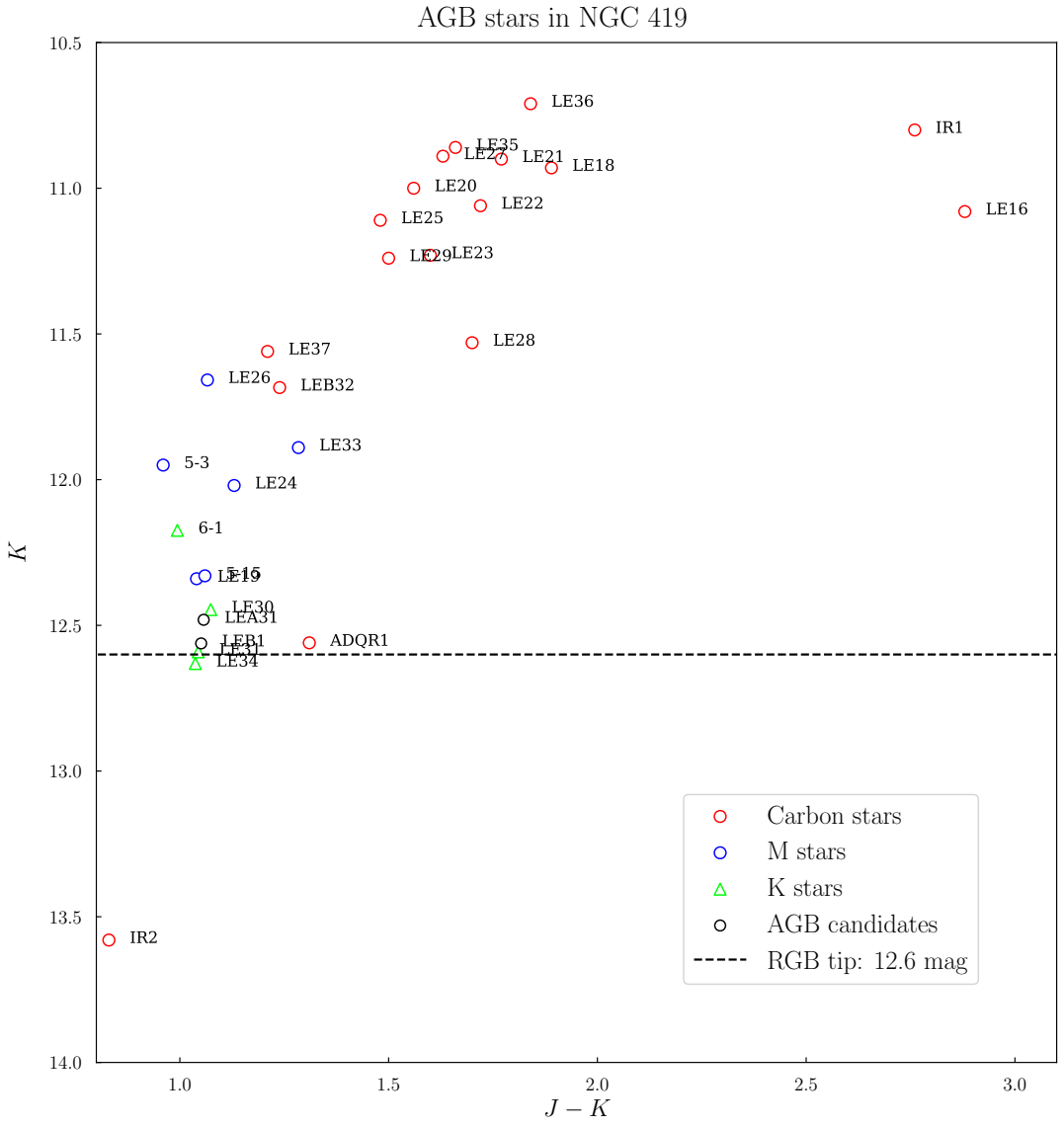

Figure 4.2: Distribution of AGB stars in color-magnitude diagram in band J and color $J - K$. As can be seen, some star is fainter than the RGB tip for the SMC determined in Boyer et al. (2011).

Table 4.3: Distance of AGB stars of NGC 419 from center.

Center: (SIMBAD)	$RA_C = 01h\ 08m\ 17.79s$ $DEC_C = -72°53'02''.8$	$R_C = 21pc$
Ident	**Distance from center**	**Membership**
LE16	59.97 pc	**NO**
ADQR1	26.75 pc	**NO**
LE20	22.57 pc	**NO**
LE21	19.74 pc	Yes
IR1	18.30 pc	Yes
5-3	11.64 pc	Yes
LE25	8.23 pc	Yes
LE24	7.95 pc	Yes
LE35	1.17 pc	Yes
LE37	6.44 pc	Yes
LE36	7.53 pc	Yes
LE27	10.88 pc	Yes
LE28	19.44 pc	Yes
LE23	14.20 pc	Yes
LE22	16.22 pc	Yes
LE29	18.52 pc	Yes
LE19	20.95 pc	Yes
5-15	21.89 pc	**NO**
LE18	25.89 pc	**NO**
IR2	2.15 pc	Yes
TLE33	12.00 pc	Yes
TLE26	3.11 pc	Yes
TLE31	12.35 pc	Yes
TLE30	11.57 pc	Yes
TLE34	33.62 pc	**NO**
ARP VI-1	6.42 pc	Yes
LEB32	68.99 pc	**NO**
LEB1	70.87 pc	**NO**
LEA31	100.80 pc	**NO**

4.2 AGB sample

Before going on with the discussion, an important aspect has to be noticed: in order to be consistent, in the previous analysis a radius of $R \sim 21\ pc$ has been fixed for the cluster, hence a mass of $M \sim 1.31 \times 10^5\ M_\odot$. Therefore now it is necessary to check if AGB stars considered are inside of this radius. To do that, central coordinates of NGC 419 are taken from `SIMBAD` database:

$$RA_C = 01h\ 08m\ 17.79s \tag{4.1}$$

$$DEC_C = -72^\circ\ 53'\ 02''.8 \tag{4.2}$$

and then, to obtained the distance of each star from the center, the following formula is used:

$$R = \sqrt{[(RA - RA_C) \cdot \cos(DEC)]^2 + (DEC - DEC_C)^2} \tag{4.3}$$

this relation takes into account the fact that equatorial coordinates are not an orthogonal system. Obviously the radius has to be converted in *arcsec* and then in physical units through the relation:

$$R_{[pc]} = D_c \cdot \tan\left(\frac{R \cdot 3600}{206265}\right) \tag{4.4}$$

where

$$D_c = 10^{\frac{18.934+5}{5}} = 61206.85\ pc \tag{4.5}$$

is the distance of the cluster assuming a distance modulus of $DM = 18.934$. The physical distance of each star is reported in table 4.3. In the end the initial sample has to be corrected discarting stars which are out of the fixed radius and stars which are below the RGB tip magnitude of $K = 12.6\ mag$ (Boyer et al., 2011). The final sample of AGB stars which will be consider in the next work consists of 19 stars whose photometry are reported in Table 4.4.

An important aspect has to be stressed: Spectral type (i.e. classification of stars as *C*- or *M*- stars) are of fundamental importance since it is one of the observables which allows to test models. Spectral types of some AGB variables in Kamath et al. (2010) are taken from Frogel et al. (1990), while for AGB stars with unknown spectral type, spectra have been obtained with the Dual Beam Spectrograph on the 2.3 m telescope of the Australian National University at Siding Spring Observatory. There are a couple of discrepancies in the Kamath et al. (2010) sample: the first one concerns the star LE24, which has an undefined spectral type in Kamath et al. (2010), but it is classified as an M0 in Lloyd Evans (1983). In the work it will be considered as an M-star. The second one is the spectral type of the star LE36, which is classified as an M-star by Lloyd Evans (1983) and as a C-star by Frogel et al. (1990) hence by Kamath et al. (2010). In the next work LE36 it will be considered a C-star. The last point to be aware of is represented by the three K-stars LE31, LE30 and 6-1. They could be early AGB stars. They will be considered in the class of M-stars.

In the end, the important properties of observed TP-AGB stars, which will be fundamental in the next analysis of AGB models, are briefly summarised in Table 4.5. These observed values are the reference ones to compare the results and to test AGB models.

Table 4.4: Final sample: Spectral type and photometry of AGB stars of NGC 419. The first group of stars is the one taken from Kamath et al. (2010) with CASPIR photometry. The second group has 2MASS photmetry taken from Cutri et al. (2003).

Ident	Spectral Type	J	K	Photometry
LE21	C	12.67	10.90	CASPIR
IR1	C	13.56	10.80	CASPIR
5-3	M	12.91	11.95	CASPIR
LE25	C	12.59	11.11	CASPIR
LE24	M	13.15	12.02	CASPIR
LE35	C	12.52	10.86	CASPIR
LE37	C	12.77	11.56	CASPIR
LE36	C	12.55	10.71	CASPIR
LE27	C	12.52	10.89	CASPIR
LE28	C	13.23	11.53	CASPIR
LE23	C	12.83	11.23	CASPIR
LE22	C	12.78	11.06	CASPIR
LE29	C	12.74	11.24	CASPIR
LE19	M	13.38	12.34	CASPIR
LE33	M	13.174	11.89	2MASS
LE26	M	12.724	11.658	2MASS
LE31	K	13.635	12.591	2MASS
LE30	K	13.52	12.446	2MASS
6-1	K	13.168	12.174	2MASS

Table 4.5: Main properties of TP-AGB stars of NGC 419 important to test AGB models.

Observed properties	Values
Number of TP-AGB stars	19
Number of C-stars	11
Number of M-stars	8
C/M ratio	1.375
M-C transition (the most luminous M-star)	11.66 mag
AGB tip (the most luminous C-star)	10.71 mag

4.3 Evolutionary tracks and isochrones: PARSEC and COLIBRI

The set of stellar evolutionary tracks from the pre-main sequence up to the first thermal pulse is taken from the database of the PAdova and TRieste Stellar Evolution Code (PARSEC). A complete descritption can be found in Bressan et al. (2012). The code computes the stellar tracks for stars with initial masses in range $0.1\ M_{\odot} \leq M_i \leq 12\ M_{\odot}$, with a resolution of $0.05\ M_{\odot}$ and $0.2\ M_{\odot}$ for low- and intermediate-mass stars respectively. The metallicity ranges from $Z = 0.0005$ to $Z = 0.07$.

Solar distribution of heavy elements. The initial abundance of every element heavier than ^{4}He is assigned relative to the total solar metallicity ($X_i/Z_{\odot}$, with $Z_{\odot} = 0.0152$) which is the reference distribution. The solar distribution consists of 90 chemical elements (Grevesse & Sauval, 1998; Caffau et al., 2011).

Opacity. Opacity of stellar matter has been computed by means of Rosseland mean opacities $\kappa_R(\rho, T)$. It depends on temperature and density but also on the gas chemical composition (H and He abundances and distribution of heavy elements). At high temperatures, in the range $4.2 \leq \log(T/K) \leq 8.7$, the opacities are provided by the Opacity Project At Livermore (OPAL), while at lower temperatures, in the range $3.2 \leq \log(T/K) \leq 4.1$, opacities are computed with AESOPUS code. For the temperature in the transition region $4.1 \leq \log(T/K) \leq 4.2$ a linear interpolation between opacities from OPAL and AESOPUS code is adopted. Two distinct sets of opacity table are generated: the H-rich one and the H-free one ($X = 0$) that describes the opacities for the He-burning regions.

Convection and overshooting. The overshoot across the border of convective regions is described by the parameter Λ_C which is the mean free path of fluid elements and it is proportional to the local pressure scale height. Λ_C in the convective core is related to stellar mass and it describes the transition between radiative and convective cores: $\Lambda_C = 0$ for $M \leq 1\ M_{\odot}$, it increases linearly up to $\Lambda_{MAX} = 0.5$ in range $1\ M_{\odot} \leq M \leq 1.4\ M_{\odot}$, and $\Lambda_C = 0.5$ for $M > 1.5\ M_{\odot}$. The overshoot efficiency in the convective envelope is tratead as in Alongi et al. (1991): $\Lambda_e = 0.05$ for $M \leq 1\ M_{\odot}$ and $\Lambda_e = 0.7$ for $M > 1\ M_{\odot}$. the transition between these two values is smooth.
Recently, the data base of PARSEC tracks has been complemented with new models of massive stars (up to $350\ M_{\odot}$), from the pre-main sequence to the central carbon ignition, covering a broad range of metallicities, $0.0001 \leq Z \leq 0.04$ (Chen et al., 2015).

The TP-AGB evolution is computed with the COLIBRI code (Marigo et al., 2013). The code computes the stellar models starting from the first thermal pulse until the almost complete ejection of the envelope via stellar winds. The initial condition for each stellar model at the first thermal pulse (core-mass, luminosity, T_{EFF}, envelope chemical composition) are taken from the PARSEC database. The robust numerical stability and the high computational speed of the code allow to perform a multiparametric and accurate calibration of the TP-AGB phase. With respect to purely-synthetic TP-AGB models, COLIBRI relaxes a significant part of the analytic formalism in favour of detailed physics applied to a complete envelope models, integrated from the atmosphere down to the H-burning shell. This approach allows to follow the basic changes in the envelope and both the energetics and nucleosynthesis of the hot bottom burning phase. In the following

the main features of COLIBRI code are presented.

Opacities. Equation of state for $\sim$ 800 atoms and molecular species as well as the Rosseland mean opacities in the atmosphere and in the deep envelope are computed *on-the-fly*. This has been obtained by the inclusion of AESOPUS code (Marigo & Aringer, 2009) for $3.2 \leq \log(T/K) \leq 4.2$ and the *Opacity Project* (OP) code (Badnell et al., 2005) for $4.2 \leq \log(T/K) \leq 8$, as internal routines of COLIBRI. This technique allows to follow in detail the evolution of surface C/O ratio which is of fundamental importance.

Hot Bottom Burning. The hot bottom burning process (HBB) is described coupling a complete nuclear network with a time-dependent diffusion scheme forconvection. It allows to treat litium nucleosynthesis. ^{7}Li nucleosynthesis follows the *Cameron-Fowler beryllium mechanism*: in the outermost layers ^{7}Li is efficiently produced and sustained by electron captures on ^{7}Be nuclei until the reservoir of ^{3}He is exhausted or HBB is extinguished due to envelope ejection by stellar winds. COLIBRI allows also to compute the nucleosynthesis of CNO, NeNa and MgAl cycles.

Pulse-driven nucleosynthesis. The chemical composition of the third dredged-up material (mainly ^{4}He, ^{12}C, ^{16}O, ^{22}Ne, ^{23}Na) is computed as means of a full nuclear network, which includes tripleα reaction and α-captures reactions applied to a simple model of the pulse-driven convection zone.

Mass-loss rates. Mass loss in AGB models is important since it controls the duration of the phase, which normally terminates when the whole envelope is ejected into the interstellar medium. Over the years substantial efforts have been done to understand the physical mechanisms responsible for mass loss in AGB stars, and more generally in red giants (Höfner & Olofsson, 2018; Willson, 2000).
While the key roles of stellar pulsation and dust growth are today universally acknowledged, a comprehensive theoretical framework is still missing.
The general scheme for the models considers two regimes of mass loss: a "pre-dust mass loss" (with a rate $\dot{M}_{\rm pre-dust}$) and a "dust-driven mass loss" (with a rate $\dot{M}_{\rm dust}$).

- The pre-dust mass loss corresponds to red giant stages, characterized by relatively low luminosities and high effective temperatures, which set unfavourable conditions for a stellar wind to be driven by radiation pressure on dust grains. During these phases mass loss should be produced by another, still not clearly identified, mechanism. Plausible candidates are the Alfvén waves and the turbulence that originate in cool extended chromospheres (Cranmer & Saar, 2011). There exist two formalisms for $\dot{M}_{\rm pre-dust}$: the Schröder & Cuntz (2005) relation modified following Rosenfield et al. (2016), and the algorithm developed by Cranmer & Saar (2011). This latter, in particular, predicts $\dot{M}_{\rm pre-dust}$ that is driven by the pressure of Alfén waves, likely produced by stellar rotation.
- The dust mass loss concerns later stages along the AGB: the chromospheric mass loss is quenched and the outflow is accelerated by the radiation pressure on dust

grains thanks to the dust-gas dynamical coupling. Several relations for $\dot{M}_{\rm dust}$, as a function of stellar parameters (M, L, $T_{\rm eff}$,, Z), are available in literature. The most popular relations are the Vassiliadis & Wood (1993) which relate the efficiency of mass loss with the pulsation period, and the Bloecker (1995) which is characterized by a significant dependence on the luminosity. In addition, in the models the recent results of dynamical atmosphere models (Mattsson et al., 2010; Eriksson et al., 2014) is used to predict $\dot{M}_{\rm dust}$ as a function of the carbon excess, C-O, in carbon stars.

During the TP-AGB evolutionary calculations, if not otherwise specified, the current mass-loss rate is taken as:

$$\dot{\rm M} = \max(\eta_{\rm pre-dust} \times \dot{\rm M}_{\rm pre-dust},\, \eta_{\rm dust} \times \dot{\rm M}_{\rm dust})\,, \tag{4.6}$$

where $\eta_{\rm pre-dust}$, and $\eta_{\rm dust}$ are adjustable efficiency parameters.

Third dredge-up Given the uncertainties and the heterogeneous results that characterize convective mixing in full TP-AGB models, it is necessary to treat the third dredge-up following a parametric scheme as detailed in Marigo et al. (2013).
In summary we need to specify three main characteristics of the third dredge-up: i) the onset, ii) the efficiency, and iii) the chemical composition of the intershell material.
The occurrence of a mixing event is usually checked with a parameter, $T_{\rm b}^{\rm dred}$, that defines the minimum temperature that should be reached at the base of the convective envelope at the stage of the maximum post-flash luminosity. Typical values lie in the range $6.3 \leq \log(T_{\rm b}^{\rm dred}) \leq 6.7$. At each thermal pulse the COLIBRI code performs complete envelope integrations to check whether the temperature criterion is satisfied or not.
Another choice, equivalent to $T_{\rm b}^{\rm dred}$, is the classical parameter $M_{\rm c}^{\rm min}$ that defines the minimum core mass for the onset of sequence of third dredge-up events. Typical values are usually within the range $0.54{\rm M}_\odot \leq M_{\rm c}^{\rm min} \leq 0.60{\rm M}_\odot$.
The efficiency of each mixing event is usually described by the parameter $\lambda = \Delta{\rm M}_{\rm dred}/\Delta{\rm M}_{\rm c}$, the fraction of the increment of the core mass during and inter-pulse period that is dredged-up at the next thermal pulse. Typical values are in the range between $\lambda = 0$ (no dredge-up) and $\lambda = 1$ (i.e. not net increase of the core mass), even though cases with $\lambda > 1$ are predicted in models that assume efficient convective overshoot (Herwig, 2004).

4.3.1 Stellar Isochrones

The production of an extended and dense (in mass and metallicity) grid of TP-AGB tracks is necessary to build accurate stellar isochrones covering the whole relevant ranges of ages and metallicities. These are fundamental instruments in the population synthesis simulations of clusters and galaxies including AGB stars, and they can be direct compared with observations. Building isochrones essentially consists in interpolating inside the grids of stellar evolutionary tracks (which describe how the stellar properties vary as a function of time t) to produce a sequence of properties as a function of M_i for a given set of t. In order to do this, the method of interpolating between tracks using pairs of *equivalent evolutionary points* (EEP) is used: once a pair of EEPs is identified in two adiacent tracks, the whole evolutionary sequence between these EEPs is assumed to be equivalent and interpolated in all quantities, using M_i and age as independent variables. When a dense grid of interpolated tracks of masses M_i is built, it is possible to draw a complete isochrone simply selecting points with a certain age t.

The new generation of PARSEC-COLIBRI stellar isochrones (Marigo et al., 2017) provides a detailed treatment of the TP-AGB phase, covering a wide range of metallicities ($0.0001 \leq Z_i \leq 0.06$). In building these isochrones many improvements are introduced: use of new TP-AGB tracks with the related atmosphere models and with the spectra for M- and C-type stars; inclusion of dredge-up episodes and hot bottom burning; inclusion of complete thermal pulse cycles (Trabucchi et al., 2017); use of new pulsation models and new dust models (which follow the growth of the grains during the AGB evolution). Isochrones include the effect of light reprocessing by circumstellar dust in the envelopes of mass-losing AGB stars. Extended tables of bolometric corrections obtained through detailed radiative transfer calculations (Marigo et al., 2008; Nanni et al., 2016) are used to account for the effect of dust for both oxygen-rich mixtures (C/O < 1), dominated by silicates, and carbon-rich mixtures (C/O > 1), dominated by carbonaceous dust grains.

4.4 TP-AGB models S001-S018

The TP-AGB models to be tested for the SMC are eighteen (from S001 to S018). Their main differences (related to the main parameters described in the previous section) are reported in Table 4.6.

Models: Mass loss prescription. All the models have Cranmer & Saar (2011) prescription for the pre-dust mass loss. This kind of mass loss follows the energy flux of magneto-hydrodynamic turbulence from a subsurface convection zone to its eventual dissipation and escape through open magnetic flux tubes. This mechanism is driven by the pressure of Alfén waves, likely produced by stellar rotation. Supersonic winds can be driven by either gas pressure in a hot corona or wave pressure in cool, extended chromospheres.

All the models have Bloecker (1995) prescription for dust mass loss in the M-phase: mass loss is based on dynamical calculations of the atmospheres of Mira-like stars. The dependence of mass loss on the luminosity is significant:

$$\dot{M} = 4.83 \cdot 10^{-9} M^{-2.1} \cdot L^{2.7} \cdot \dot{M}_R \tag{4.7}$$

where $\dot{M}_R$ is the mass loss at pulsation period of $P_0 = 100\ d$.

Most of the models have Mattsson et al. (2010) prescription for dust mass loss in C-phase. The general expression for mass loss is:

$$\dot{M} \propto \tau_w \frac{L}{u_{out} - u(R_c)} \cdot \left(1 - \frac{1}{\Gamma}\right) \tag{4.8}$$

being τ_w the flux-mean optical depth far out in the wind, u_{out} and $u(R_c)$ respectively the wind velocities at the outer boundary radius (typically $20 - 30\ R$) and at the condensation radius, and the factor Γ:

$$\Gamma = \frac{\kappa L}{4\pi c G M} \tag{4.9}$$

where κ is the total flux-mean opacity.
The Mattsson et al. (2010) prescription is activated in the C-phase when the carbon-excess $(C - O) > 8.2$ (as described in Section 5.2.3).

The use of the different prescriptions varies in the models:

- From model S001 to model S016 it is always taken the maximum between pre-dust and dust mass loss prescription: $\dot{M} = max(\dot{M}_{pre-dust}; \dot{M}_{dust})$;

Table 4.6: TP-AGB model grid. CS11 = Cranmer & Saar (2011), BL95 = Bloecker (1995), MA10 = Mattsson et al. (2010), K02 = Karakas et al. (2002)

	Mass-loss Prescription						**Third Dredge-Up**	
	Pre-Dust		**Dust - driven**				**Onset**	**Efficiency**
			M-stars		**C-stars**			
SET	**Id**	η	**Id**	η	**Id**	η	T_b^{dred}	λ
S001	CS11	2	BL95	0.05	BL95	0.05	6.40	original K02 ($\lambda_{max} \sim 1$)
S002	CS11	2	BL95	0.02	MA10	1	6.40	original K02 ($\lambda_{max} \sim 1$)
S003	CS11	2	BL95	0.03	MA10	1	6.40	original K02 ($\lambda_{max} \sim 1$)
S004	CS11	2	BL95	0.05	MA10	1	6.40	original K02 ($\lambda_{max} \sim 1$)
S005	CS11	2	BL95	0.06	MA10	1	6.40	original K02 ($\lambda_{max} \sim 1$)
S006	CS11	3	BL95	0.06	MA10	1	6.40	original K02 ($\lambda_{max} \sim 1$)
S007	CS11	3	BL95	0.06	MA10	1	Z-var (case1)	K02 ($\lambda_{max} \sim 1$)
S008	CS11	3	BL95	0.06	MA10	1	Z-var (case1)	modified K02 ($\lambda_{max} = 0.5$)
S009	CS11	3	BL95	0.02	BL95	0.02	Z-var (case1)	modified K02 ($\lambda_{max} = 0.5$)
S010	CS11	3	BL95	0.01	BL95	0.01	Z-var (case1)	modified K02 ($\lambda_{max} = 0.5$)
S011	CS11	3	BL95	0.01	MA10	1	Z-var (case1)	modified K02 ($\lambda_{max} = 0.5$)
S012	CS11	3	BL95	0.01	MA10	1	Z-var (case1)	original K02
S013	CS11	3	BL95	0.01	MA10	1	Z-var (case1)	parabolic $f(M_c)$ ($\lambda_{max} = 0.5$) $M_{c0} = 0.65, M_{c1} = 0.95$
S014	CS11	3	BL95	0.01	MA10	1	Z-var (case1)	parabolic $f(M_c)$ ($\lambda_{max} = 0.5$) $M_{c0} = 0.65, M_{c1} = 0.85$
S015	CS11	3	BL95	0.01	MA10	1	Z-var (case1)	parabolic $f(M_c)$ ($\lambda_{max} = 0.6$) $M_{c0} = 0.60, M_{c1} = 0.85$
S016	CS11	3	BL95	0.01	MA10	1	Z-var (case2)	parabolic $f(M_c)$ ($\lambda_{max} = 0.6$) $M_{c0} = 0.60, M_{c1} = 0.85$
S017	CS11	3	BL95	0.01	MA10	1	Z-var (case2)	parabolic $f(M_c)$ ($\lambda_{max} = 0.6$) $M_{c0} = 0.60, M_{c1} = 0.85$
S018	CS11	3	BL95	0.02	MA10	1	Z-var (case2)	parabolic $f(M_c)$ ($\lambda_{max} = 0.6$) $M_{c0} = 0.60, M_{c1} = 0.85$

- In models S017 and S018 the prescription depends on the C/O ratio: if C/O < 1, $\dot{M} = max(\dot{M}_{pre-dust}; \dot{M}_{dust})$, while if C/O > 1, $\dot{M} = max(\dot{M}_{Mattsson}; \dot{M}_{Bloecker})$.

A last important additional point concerns the models from S011 to S018: If in the C-phase the dust-driven wind is not active, we assume Bloecker (1995) prescription.

Models: Third dredge-up prescritpion. The parameter related to the onset of the third dredge-up is the temperature T_b^{dred}.

- For the models from S001 to S006: $\log T_b^{dred} = 6.40$;

- For the models from S007 to S015, given the metallicity Z, the temperature parameter is assumed to increase with the metallicity according to a linear relation

$$T_b^{dred} = T_{b,1} + \frac{Z - Z_1}{Z_2 - Z_1} \cdot (T_{b,2} - T_{b,1}) \tag{4.10}$$

  The parameters are reported in Table 4.7, case 1;

- For the models S016, S017 and S018 the temperature parameter varies with metallicity as described above, but with prescription in Table 4.7, case 2. This second case favours earlier onset of the third dredge-up at low Z and later onset at high Z.

Table 4.7: Third dredge-up prescription: temperature parameter T_b^{dred}.

	Z_1	Z_2	$T_{b,1}$	$T_{b,2}$	$T_{MINb,1}$
case 1	0.001	0.02	6.30	6.60	6.30
case 2	0.001	0.02	6.10	6.75	6.20

The parameter related to the efficiency of the third dredge-up is λ (as defined in Section 5.2.1). It depends on intial mass, core mass and metallicity of the star.

- The models from S001 to S007 and the model S012 use original Karakas et al. (2002) prescription. The behaviour of λ varies with mass M: it is nearly linear at low M, rising steeply with mass until M $\sim 3\ M_\odot$ and flattening out to be almost constant at high mass. In this prescription the $\lambda_{max} \sim 1$;

- For models from S008 to S011 a modified Karakas et al. (2002) prescription is adopted: the maximum efficiency parameter is set to $\lambda_{max} = 0.5$;

- For models from S013 to S018 the efficiency parameter is assumed to have a parabolic behaviour as a function of the core mass M_c:

$$\lambda = a + bM_c + cM_c^2 \tag{4.11}$$

  The values of λ_{max} for the different models are reported in Table 4.6 and the quantities M_{c0} and M_{c1} represent respectively the core mass at λ_{max} and at $\lambda = 0$.

4.5 Simulations

Simulations are run with the code TRILEGAL with the aim to reproduce observed properties of the sample of AGB stars summarised in Table 4.5. The magnitudes of the observed sample are both from 2MASS and CASPIR photometries. In simulations the photometry used is the CASPIR one: it has been checked that the photometry of a synthetic sample produced using 2MASS filters differs from CASPIR one for a quantity of the order of 0.04 *mag*. So it is possible to choose to use just CASPIR photometry.

In order to produce more reliable results, simulations are done considering a mass a thousand higher than the one of NGC 419, i.e. a mass of $M = 1.31 \times 10^7\ M_\odot$. From this large simulation then a thousand random simulations are extracted each one with a mass equal to $M = 1.31 \times 10^5\ M_\odot$ (i.e. the value estimated for the cluster mass). For each simulation the quantities of interest are computed: the number of AGB star produced, the number of C-stars, the number of M-stars, the most luminous M-star (which corresponds to the transition luminosity from M- to C-stars) and the most luminous C-star (which represents the AGB tip).

Since the distribution of the quantities is not symmetric (therefore the inferior and superior errors are not equal in principle), the final value and the confidence limits are obtained considering the *cumulative distribution function*: this gives the probability that a quantity takes a value less or equal to a certain size. As an example, in Figure 4.3 it is represented the count of C-stars for the model S017 using the cumulative function: once the histogram with the related probability in each bin of values has been built and a linear interpolation which connects the central points of the bins has been considered, the median value is the quantity at which cumulative function is equal to 0.5, while the inferior and superior errors are respectively the values at which the cumulative function is equal to $0.5 - 0.341 = 0.159$ and $0.5 + 0.341 = 0.841$ (being $1\sigma = 0.6827$). This method has been used for all the relevant quantities obtained. The results of the comparison between observations and models are reported in Table 4.8.

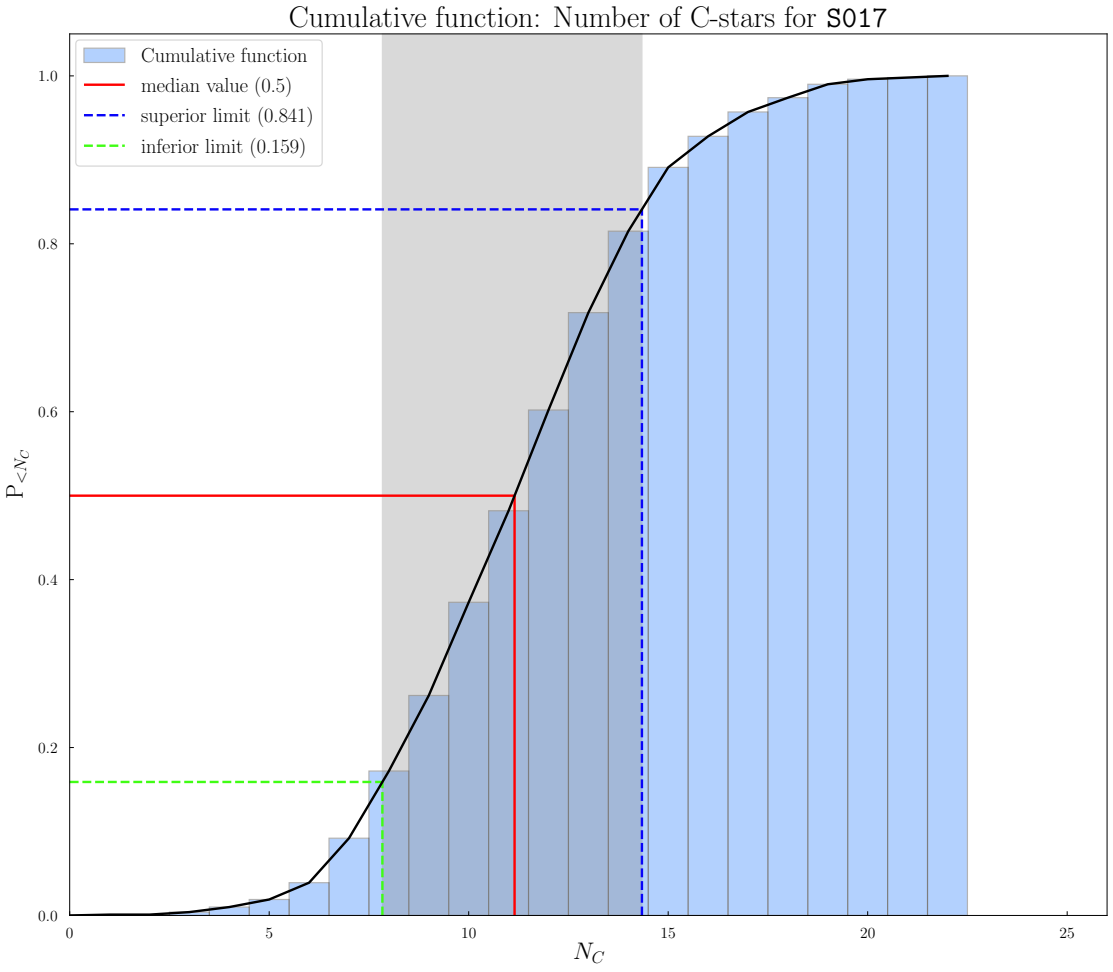

Figure 4.3: Cumulative distribution function for the number of C-stars in the set S017.

Table 4.8: Results of simulations for different models (from S001 to S018). A thousand of random simulations are taken from a simulation with a mass a thousand higher than the one estimated for the cluster. Then the median values and the associated error are computed for each parameter using the cumulative function.

	AGB	**C**	**M**	**C/M**	**M-C transition**	**AGB tip**
Obs:	**19 ± 4.4**	**11 ± 3.3**	**8 ± 2.8**	**1.375**	**11.66 mag**	**10.71 mag**
S001	$9.4^{+3.1}_{-2.7}$	$5.7^{+2.4}_{-2.3}$	$3.4^{+2.3}_{-1.9}$	1.680	$12.02^{+0.15}_{-0.13}$	$11.05^{+0.29}_{-0.12}$
S002	$13.3^{+3.7}_{-3.5}$	$10.2^{+3.2}_{-3.1}$	$2.3^{+2.0}_{-1.6}$	4.400	$12.14^{+0.12}_{-0.13}$	$10.84^{+0.24}_{-0.12}$
S003	$13.4^{+3.9}_{-3.5}$	$10.3^{+3.3}_{-3.0}$	$2.4^{+1.7}_{-1.6}$	4.267	$12.16^{+0.10}_{-0.12}$	$10.86^{+0.22}_{-0.13}$
S004	$13.0^{+4.1}_{-3.3}$	$10.1^{+3.4}_{-3.1}$	$2.4^{+2.1}_{-1.6}$	4.226	$12.14^{+0.11}_{-0.13}$	$10.84^{+0.22}_{-0.13}$
S005	$13.4^{+3.5}_{-3.3}$	$10.4^{+3.1}_{-3.1}$	$2.5^{+2.0}_{-1.6}$	4.206	$12.15^{+0.12}_{-0.13}$	$10.87^{+0.21}_{-0.14}$
S006	$11.4^{+3.4}_{-3.0}$	$8.4^{+3.1}_{-2.8}$	$2.3^{+1.9}_{-1.5}$	3.650	$12.13^{+0.12}_{-0.13}$	$10.92^{+0.24}_{-0.11}$
S007	$11.8^{+3.5}_{-3.2}$	$9.0^{+3.3}_{-2.9}$	$2.3^{+1.8}_{-1.6}$	3.962	$12.17^{+0.11}_{-0.16}$	$10.92^{+0.22}_{-0.10}$
S008	$11.5^{+3.5}_{-3.2}$	$8.6^{+3.1}_{-2.9}$	$2.4^{+1.9}_{-1.6}$	3.504	$12.16^{+0.12}_{-0.13}$	$10.94^{+0.24}_{-0.13}$
S009	$11.5^{+3.3}_{-3.7}$	$8.3^{+2.8}_{-2.9}$	$2.4^{+1.8}_{-1.5}$	3.426	$12.15^{+0.12}_{-0.16}$	$10.91^{+0.22}_{-0.10}$
S010	$12.0^{+3.4}_{-3.3}$	$8.7^{+3.3}_{-2.6}$	$2.4^{+2.0}_{-1.6}$	3.680	$12.14^{+0.13}_{-0.13}$	$10.88^{+0.22}_{-0.11}$
S011	$11.6^{+3.5}_{-3.3}$	$8.5^{+3.2}_{-3.0}$	$2.3^{+2.6}_{-1.5}$	3.631	$12.16^{+0.11}_{-0.15}$	$10.94^{+0.24}_{-0.12}$
S012	$11.5^{+3.5}_{-3.3}$	$8.5^{+3.2}_{-2.7}$	$2.3^{+1.9}_{-1.5}$	3.790	$12.16^{+0.12}_{-0.13}$	$10.94^{+0.25}_{-0.12}$
S013	$11.0^{+3.2}_{-3.1}$	$7.1^{+2.8}_{-2.6}$	$3.5^{+2.0}_{-1.8}$	2.027	$12.03^{+0.17}_{-0.14}$	$10.88^{+0.23}_{-0.12}$
S014	$10.9^{+3.4}_{-3.1}$	$6.5^{+2.5}_{-2.6}$	$3.9^{+2.2}_{-2.0}$	1.674	$11.95^{+0.19}_{-0.14}$	$10.82^{+0.26}_{-0.11}$
S015	$11.0^{+3.3}_{-3.1}$	$6.8^{+2.8}_{-2.5}$	$3.5^{+2.2}_{-1.8}$	1.961	$12.01^{+0.15}_{-0.14}$	$10.94^{+0.21}_{-0.13}$
S016	$11.1^{+3.4}_{-3.1}$	$8.1^{+2.7}_{-2.7}$	$2.6^{+2.0}_{-1.6}$	3.099	$12.13^{+0.12}_{-0.16}$	$10.99^{+0.24}_{-0.14}$
S017	$14.4^{+3.8}_{-3.8}$	$11.2^{+3.4}_{-3.4}$	$2.5^{+2.0}_{-1.6}$	4.414	$12.12^{+0.14}_{-0.14}$	$10.81^{+0.14}_{-0.20}$
S018	$13.6^{+3.6}_{-3.4}$	$10.6^{+3.4}_{-3.2}$	$2.7^{+1.9}_{-1.6}$	3.972	$12.13^{+0.12}_{-0.16}$	$10.83^{+0.22}_{-0.12}$

The same results (for each relevant quantity) are graphically represented in the plots below: in Figure 4.4 the number of observed/predicted AGB stars, in Figure 4.5 the number of observed/predicted C-stars, in Figure 4.6 the number of observed/predicted M-stars, in Figure 4.7 the observed/predicted M/C transition luminosity, in Figure 4.8 the observed/predicted AGB tip luminosity. The observed quantities are represented with a line, while the expected ones are represented with a dot with the relative error bars for each model.

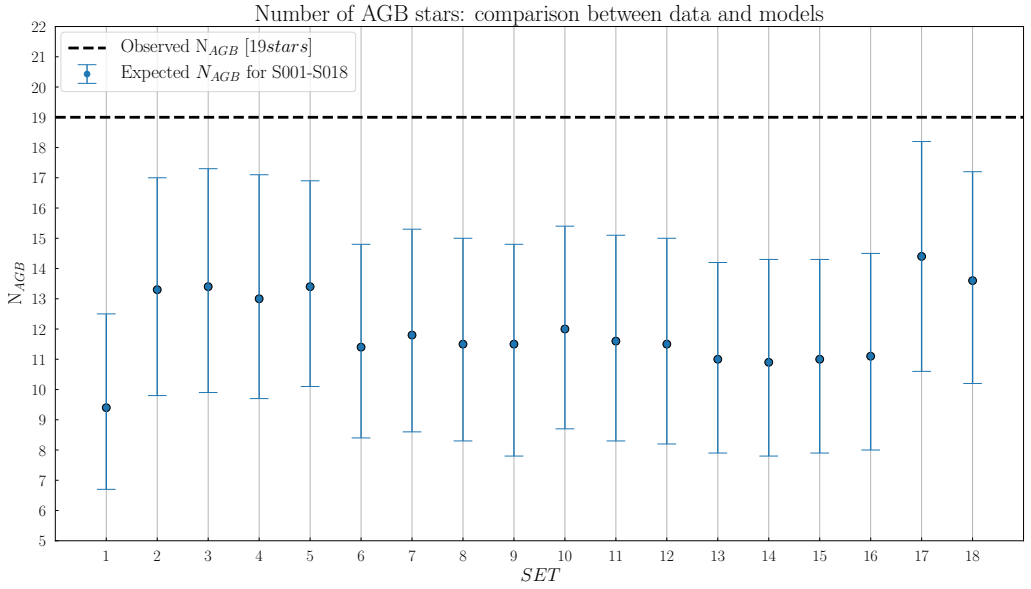

Figure 4.4: Comparison between observed AGB sample and models (`S001-S018`) of the number of AGB stars.

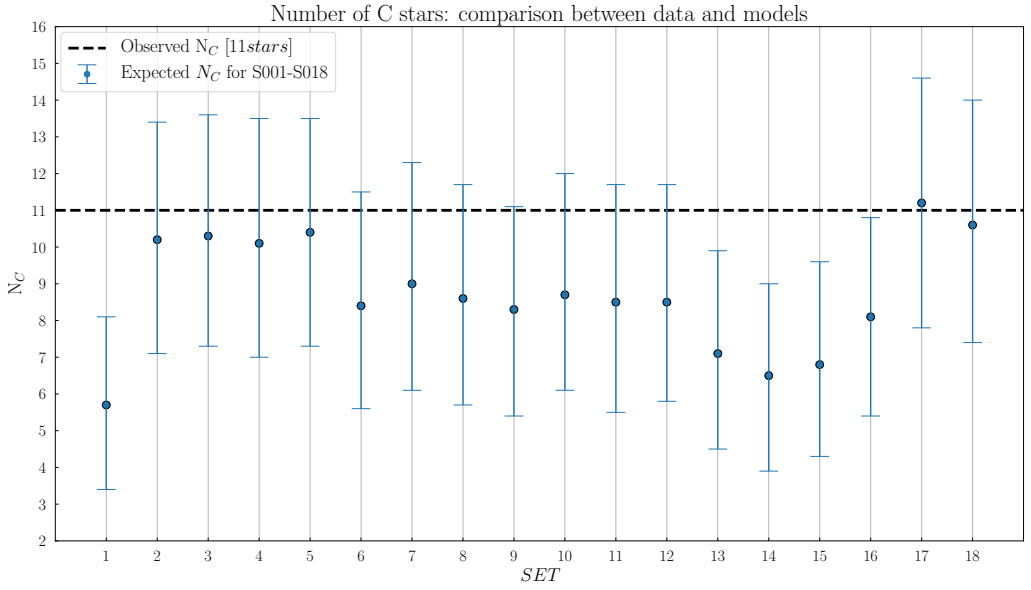

Figure 4.5: Comparison between observed AGB sample and models (`S001-S018`) of the number of C-stars.

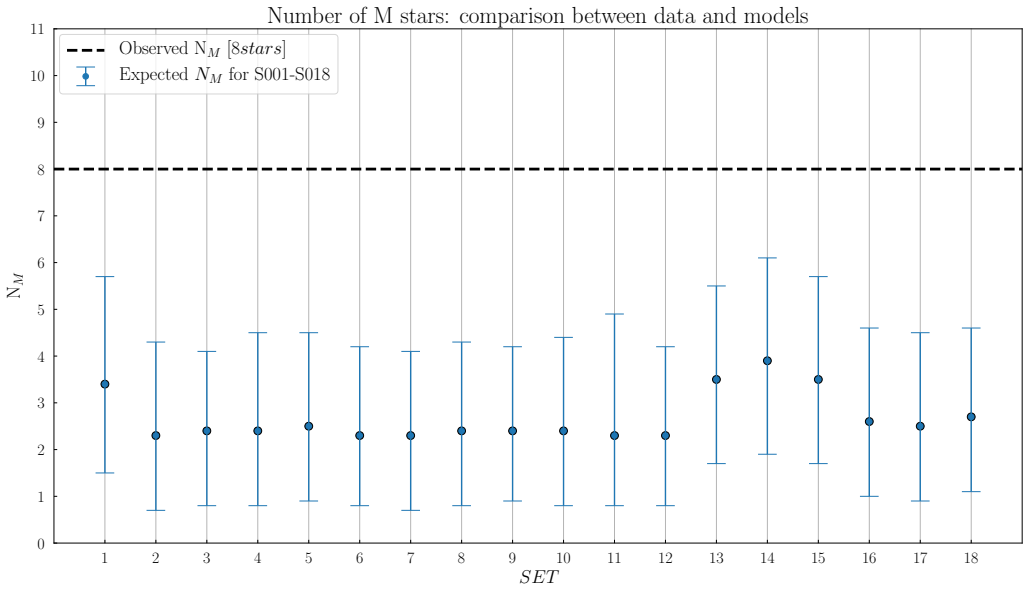

Figure 4.6: Comparison between observed AGB sample and models (`S001-S018`) of the number of M-stars.

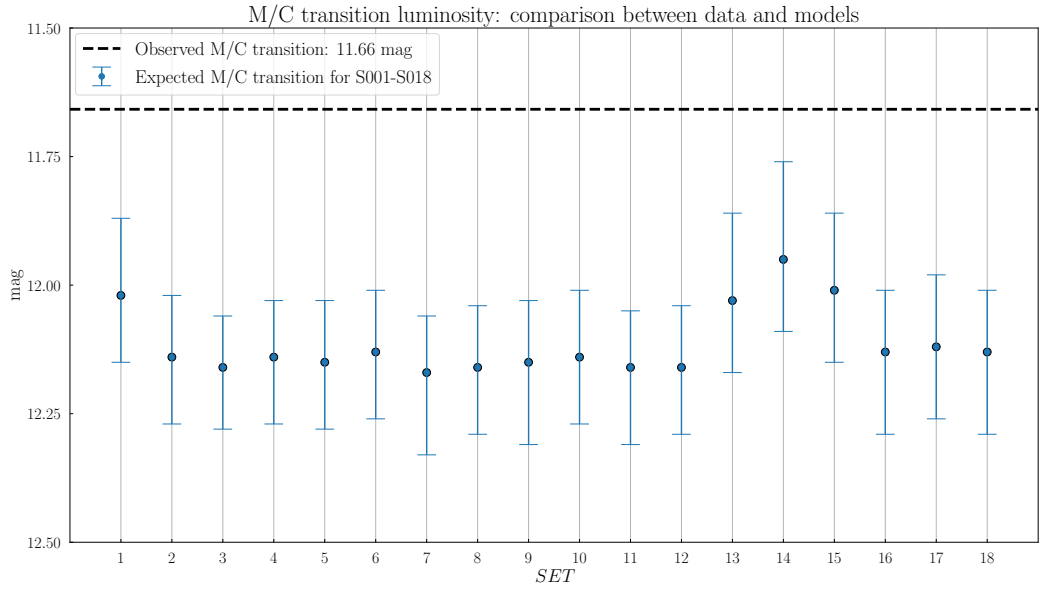

Figure 4.7: Comparison between observed AGB sample and models (`S001-S018`) of the most luminous M-star (M/C transition luminosity).

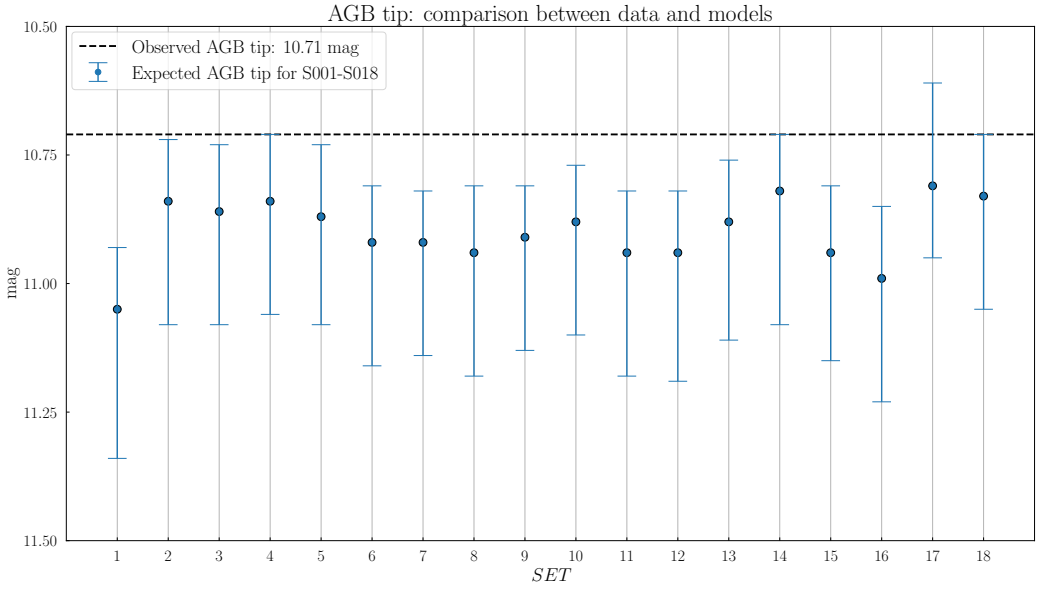

Figure 4.8: Comparison between observed AGB sample and models (`S001-S018`) of the most luminous C-star (AGB tip).

Chapter 5

Discussion and Conclusions

All the models S001-S018 are built to simulate the field AGB stars of the SMC (Pastorelli, PhD Thesis), so it has to be taken into account when considering results of simulations. From Figures 4.4, 4.5, 4.6, 4.7 and 4.8 it is evident that:

- Most of models succeed in reproducing the observed C-star counts within 1σ (especially S002, S003, S004, S005, S017, S018);
- In all the models there is a clear *deficit* in the predicted number of M-stars (the only models which reach the 1σ confidence region are S001 and S014);
- The marginally lack of predicted M-stars is supported by the fact that predicted M/C transition luminosity is fainter than the observed one for all the models;
- There is agreement in reproducing AGB tip luminosity (best models are S004, S017, S018).

The discrepancy between the number of predicted and observed M-stars together with the fainter predicted M/C transition luminosity is a clear indication that *third dredge-up* should be activated later (hence at lower luminosity). While the number of C-stars and the AGB tip depend on both the mass loss prescriptions and the characteristics of third dredge-up, the number of M-stars and the M/C transition luminosity instead depend only on the third dredge-up features, especially on the onset. From Figures 4.6 and 4.7 it can be seen that for models from S002 to S012 the results of simulations are very similar. The effects of differences in third dredge-up prescriptions (between Karakas et al. (2002) and $\lambda_{MAX} = 0.5$, see Table 4.6), are here not visible because of the small initial mass considered ($M = 1.65\ M_{\odot}$).

In the following section we discuss in details the models S001, S014, S017. For the analysis, tracks with a metallicity of $Z = 0.004$ and an initial mass of $M = 1.65\ M_{\odot}$ are considered (these values are the closest to the ones estimated for NGC 419).

5.1 Mass loss regimes

The three models S001, S014 and S017 have different mass loss prescriptions:

- S001: The predust mass loss is taken from Cranmer & Saar (2011) while the dust mass loss is taken from Bloecker (1995). At any stage the current $\dot{M}$ is taken as the maximum between them. The efficiency parameter is $\eta = 0.05$ and this model predicts the shortest duration of the entire TP-AGB phase ($t \sim 1.87\ Myr$). The M-phase lasts $\sim 1.1\ Myr$, while the C-phase lasts $\sim 0.76\ Myr$.

- `S014`: The predust mass loss is taken from Cranmer & Saar (2011)) while the dust mass loss now depends on C/O ratio: if C/O $\leq$ 1, the prescription is the one from Bloecker (1995), if C/O $>$ 1 and the carbon-excess exceeds the limit value of C-O$_{MIN}$ = 8.2, the prescription is the one from Mattsson et al. (2010). At any stage the current $\dot{M}$ is taken as the maximum between predust and dust prescription. The parameter η is lower than the previous case ($\eta = 0.01$). From Figure 5.1 it can be seen that the mass loss used is quite the same (the predust one) until the Mattson precription is activated at the final stages of TP-AGB phase. This model predicts a duration of $\sim 2.14\ Myr$ for the TP-AGB phase. The M-phase lasts $\sim 1.31\ Myr$, while the C-phase lasts $\sim 0.83\ Myr$.

- `S017`: The prescription for the mass loss is the same of the model `S014`. The difference is that this model considers the maximum between predust and dust prescription if C/O $\leq$ 1, while it considers the maximum between Mattsson and Bloecker mass losses when C/O $>$ 1. Effectively from Figure 5.1 it can be seen that if C/O $\leq$ 1 the mass loss is the predust one, then until C-excess limit value is reached the mass loss is the Bloecker one, in the last part mass loss is the Mattsson one. The parameter η s equal to 0.01. This different prescription has been introduced to test the possibility to prolong TP-AGB phase as suggested by AGB stellar simulations in SMC (Pastorelli et al., in preparation). This model predicts a duration of $\sim 2.5\ Myr$ for the TP-AGB phase. The M-phase lasts $\sim 1.11\ Myr$, while the C-phase lasts $\sim 1.4\ Myr$.

In Figure 5.1 different prescriptions of mass loss for the three models are shown. On average the mass loss increases with time. The zero point of time (x-axis) is taken at the beginning of TP-AGB phase. In Figure 5.2 current mass as a function of time is shown: mass decreases slowly when C/O $\leq$ 1 and more steeply when C/O $>$ 1 (because of the different regimes discussed above). The value of the mass at the end of TP-AGB phase is very close to the value of the remnant white dwarf.

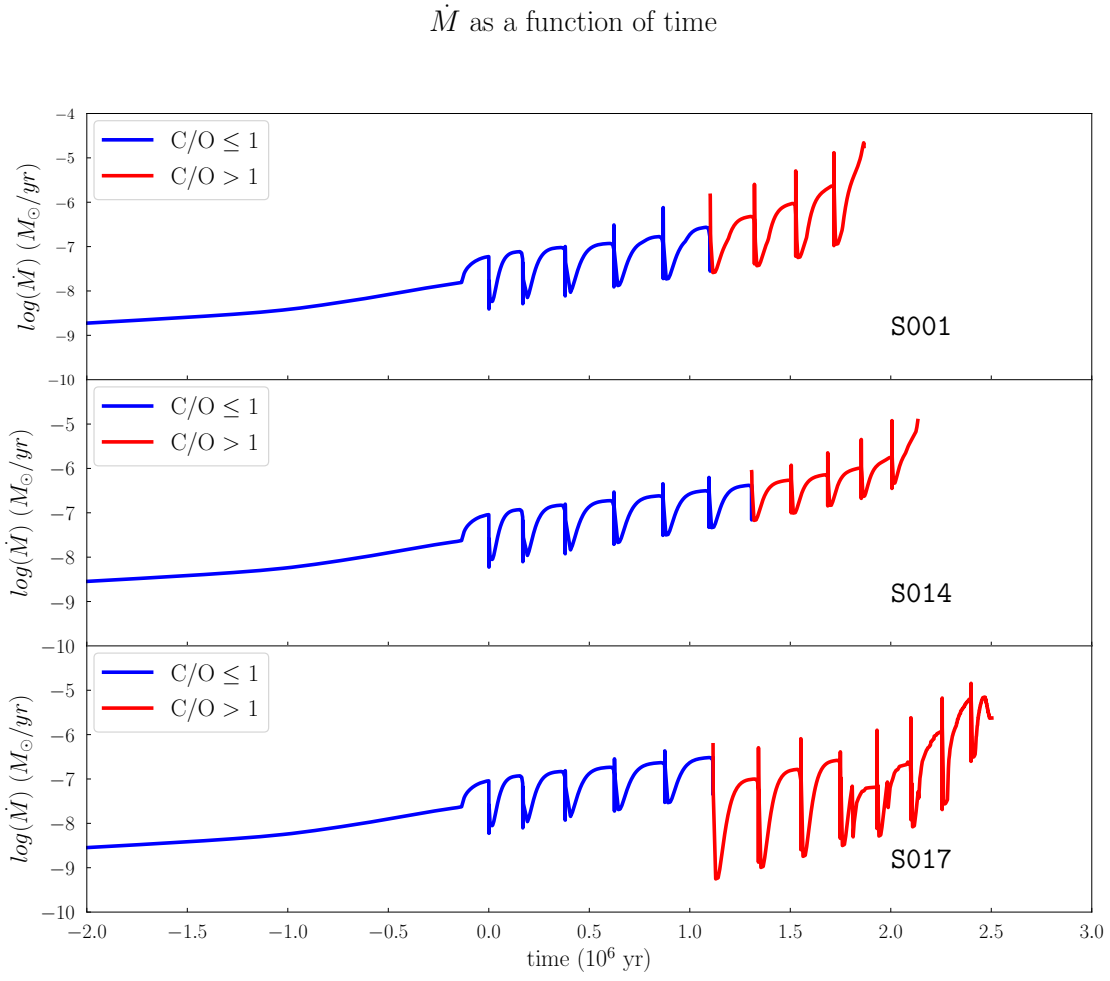

Figure 5.1: Mass loss as a function of time for the three models `S001`, `S014`, `S017`.

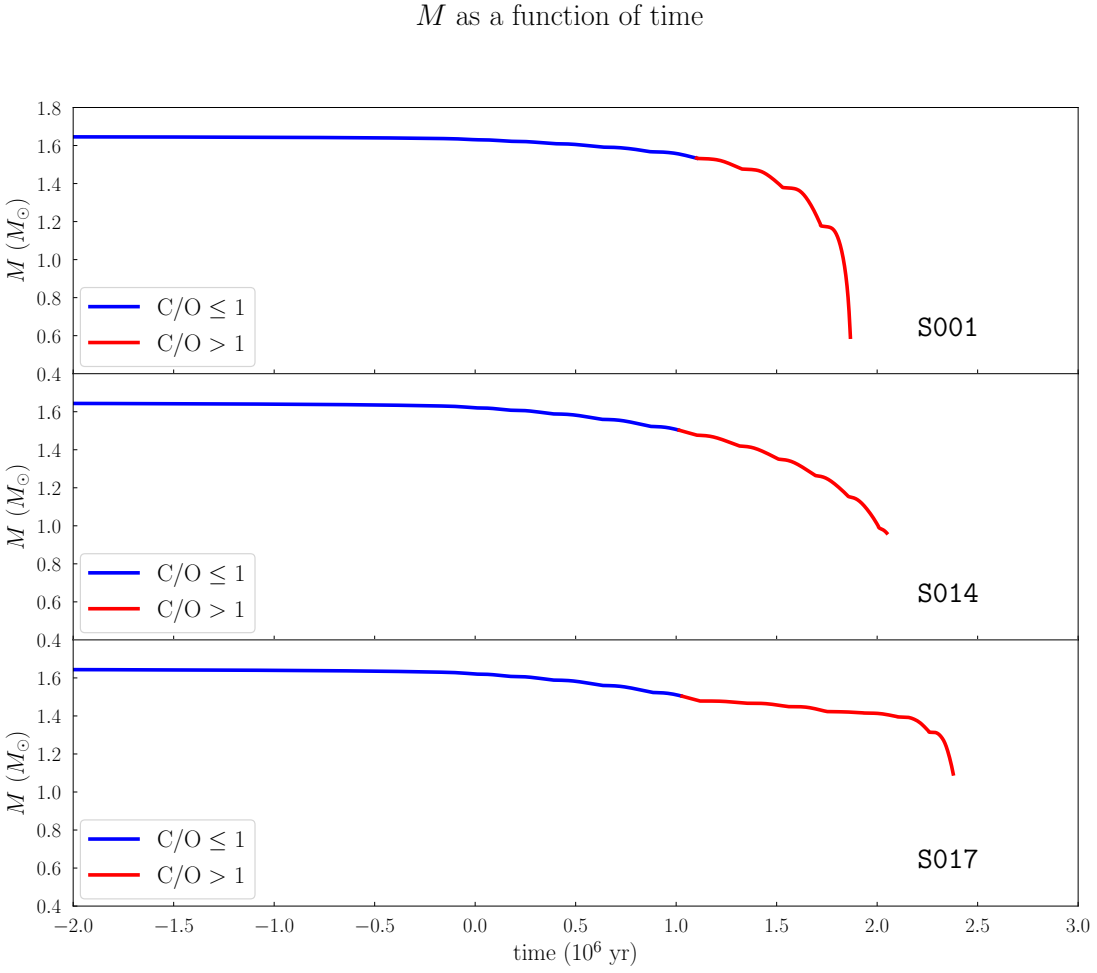

Figure 5.2: Mass as a function of time for the three models `S001`, `S014`, `S017`.

5.2 Characteristics of third dredge up

5.2.1 Onset and Efficiency

Efficiency of the third dredge-up (3DU) is quantified by the parameter λ which is defined as the ratio between the mass which is dredged-up into the envelope and the mass by which the H-exhausted core has grown during the preceding interpulse period.

$$\lambda = \frac{\Delta M_{dup}}{\Delta M_H} \tag{5.1}$$

- Model `S001` uses the prescription of Karakas et al. (2002);
- Models `S014` and `S017` use a different formalism (Pastorelli et al., in preparation).

From Figure 5.3 it can be noticed that in all three cases the efficiency shows a rising branch until a maximum and then a decline related to the decrease of envelope mass due to mass loss. In the three models the activation of 3DU occurs at different times and values of core mass: in `S001` and `S014` the 3DU occurs at $M_C \sim 0.540\ M_\odot$, while in `S017` the 3DU occurs at $M_C \sim 0.532\ M_\odot$. A later onset of the 3DU implies a longer M-phase: infact model `S017` predicts a smaller number of M-stars (than `S001` and `S014`) since the activation of 3DU is rather earlier.

5.2.2 The photospheric C/O ratio

C/O ratio is a fundamental quantity: AGB stars have initially a photospheric $C/O < 1$, i.e. they are O-rich (classified as M-stars). With the repeated occurence of the *third dredge-up* the new products of He-burning, and mainly carbon, are brought to the surface and the C/O ratio at a certain point exceeds unit (C-stars). Figure 5.4 shows the C/O ratio as a function of time for the three models `S001`, `S014`, `S017`. The zero point of time (x-axis) is taken at the beginning of TP-AGB phase. It can be noticed again that M-phase (C/O < 1) and C-phase (C/O > 1) have different duration in the three models. Moreover also the maximum value of C/O is different: in models `S001` and `S014` the value of $\mathrm{C/O}_{MAX}$ is comparable (respecively ~ 2.5 and ~ 2.25), while in model `S017` C/O reaches a very high value (~ 5.65). In model `S017` indeed the C-phase is longer.

5.2.3 Carbon excess

Another fundamental quantity is the carbon excess, defined as

$$C - O = \log_{10}\left(\frac{n_C}{n_H} - \frac{n_O}{n_H}\right) + 12 \tag{5.2}$$

where n_C, n_O, n_H are the abundances of various elements and the two abundance ratios are

$$\frac{n_C}{n_H} = \frac{\left[\frac{X(^{12}\mathrm{C})}{A_{^{12}\mathrm{C}}} + \frac{X(^{13}\mathrm{C})}{A_{^{13}\mathrm{C}}}\right]}{\frac{X(H)}{A_H}} \tag{5.3}$$

$$\frac{n_O}{n_H} = \frac{\left[\frac{X(^{16}\mathrm{O})}{A_{^{16}\mathrm{O}}} + \frac{X(^{17}\mathrm{O})}{A_{^{17}\mathrm{O}}} + \frac{X(^{18}\mathrm{O})}{A_{^{18}\mathrm{O}}}\right]}{\frac{X(H)}{A_H}} \tag{5.4}$$

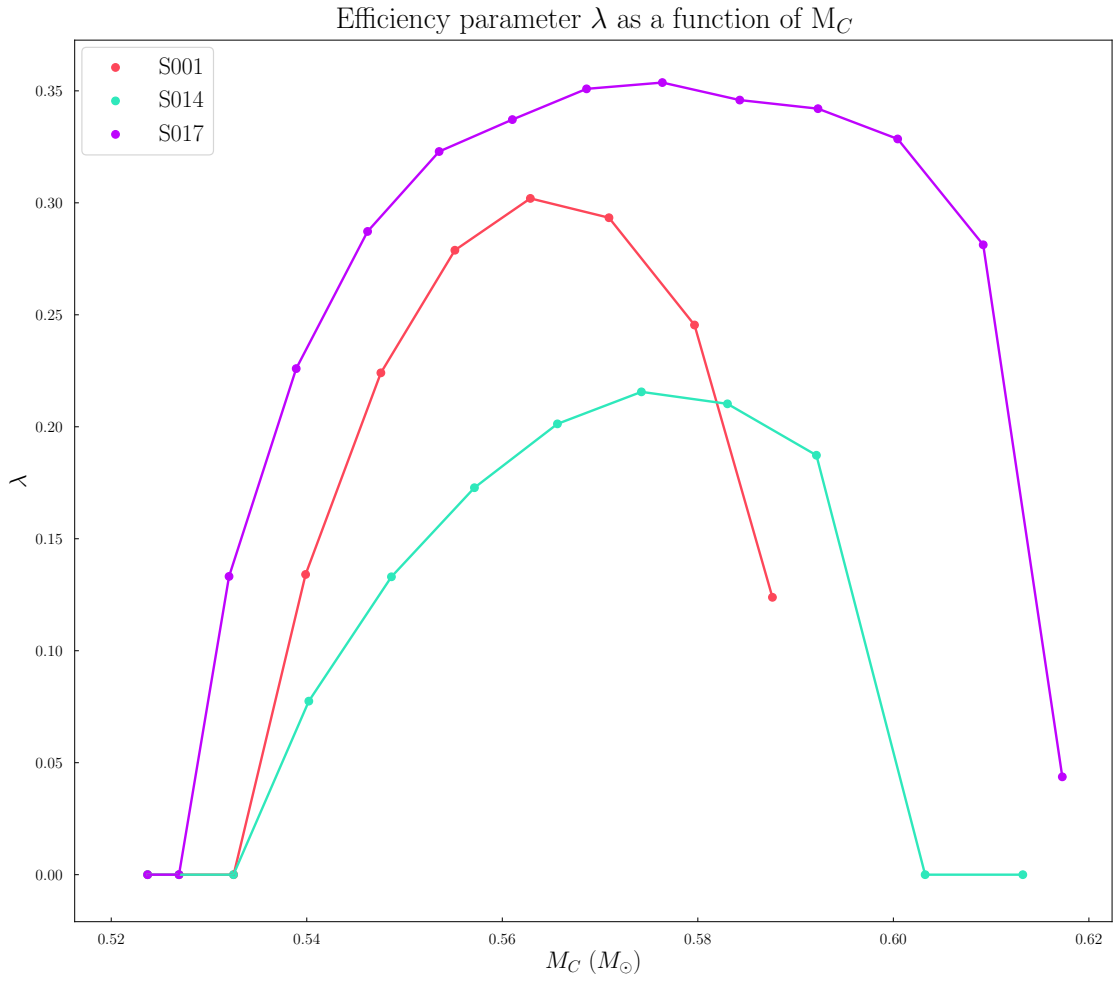

Figure 5.3: Efficiency parameter as a function of core mass for the three models `S001`, `S014`, `S017`.

In figure 5.5 C-O behaviour as a function of time is shown. This is a key parameter since mass loss prescriptions of models `S014` and `S017` take into account C excess: Mattsson prescription for mass loss is activated when the carbon excess exceeds the limit value of $(\text{C-O})_{MIN} = 8.2$ (Mattsson et al., 2010). It can be seen that in model `S014` it occurs $\sim 1.69\ Myr$ after the beginning of TP-AGB phase, while in model `S017` it occurs earlier, $\sim 1.55\ Myr$ after the beginning of the TP-AGB phase.

5.2.4 Core mass as a function of time

The core mass of an AGB star M_C is defined as the mass below H-He discontinuity (i.e. the discontinuity between H-rich envelope and He-rich core). It can be noticed an average increase of the core mass during each interpulse period (the H-He discontinuity moves outward). The occurence of third dregde-up causes a quasi-istantaneous reduction of the core mass. The core mass at the end of TP-AGB phase represents the mass of the remnant white dwarf (M_{WD}). From figure 5.6 it can be seen that different models predict different masses: `S001` predicts $M_{WD} \sim 0.59\ M_\odot$, `S014` predicts $M_{WD} \sim 0.61\ M_\odot$ and `S017` predicts $M_{WD} \sim 0.62\ M_\odot$. Model `S001` predicts the lowest M_{WD}, as expected since it reaches the

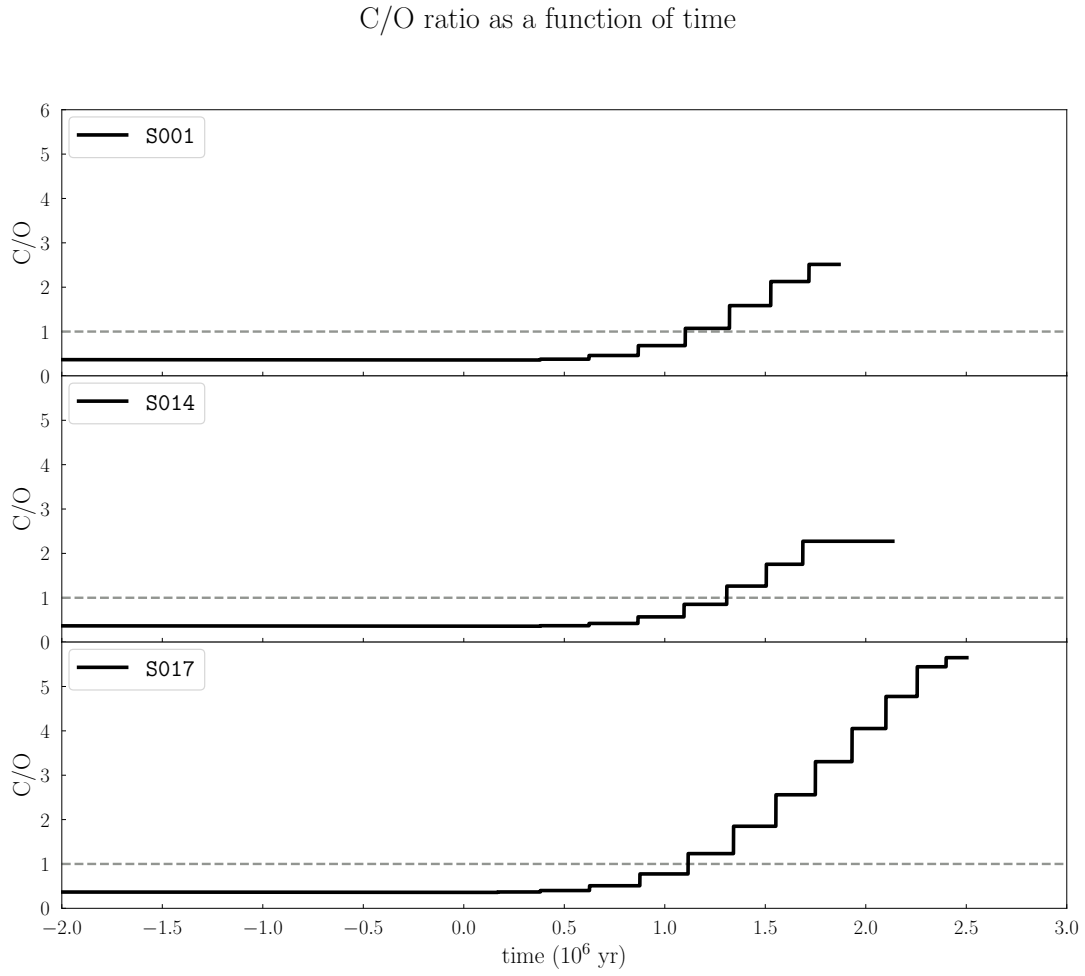

Figure 5.4: C/O ratio as a function of time for the three models `S001`, `S014`, `S017`.

highest mass loss rate.

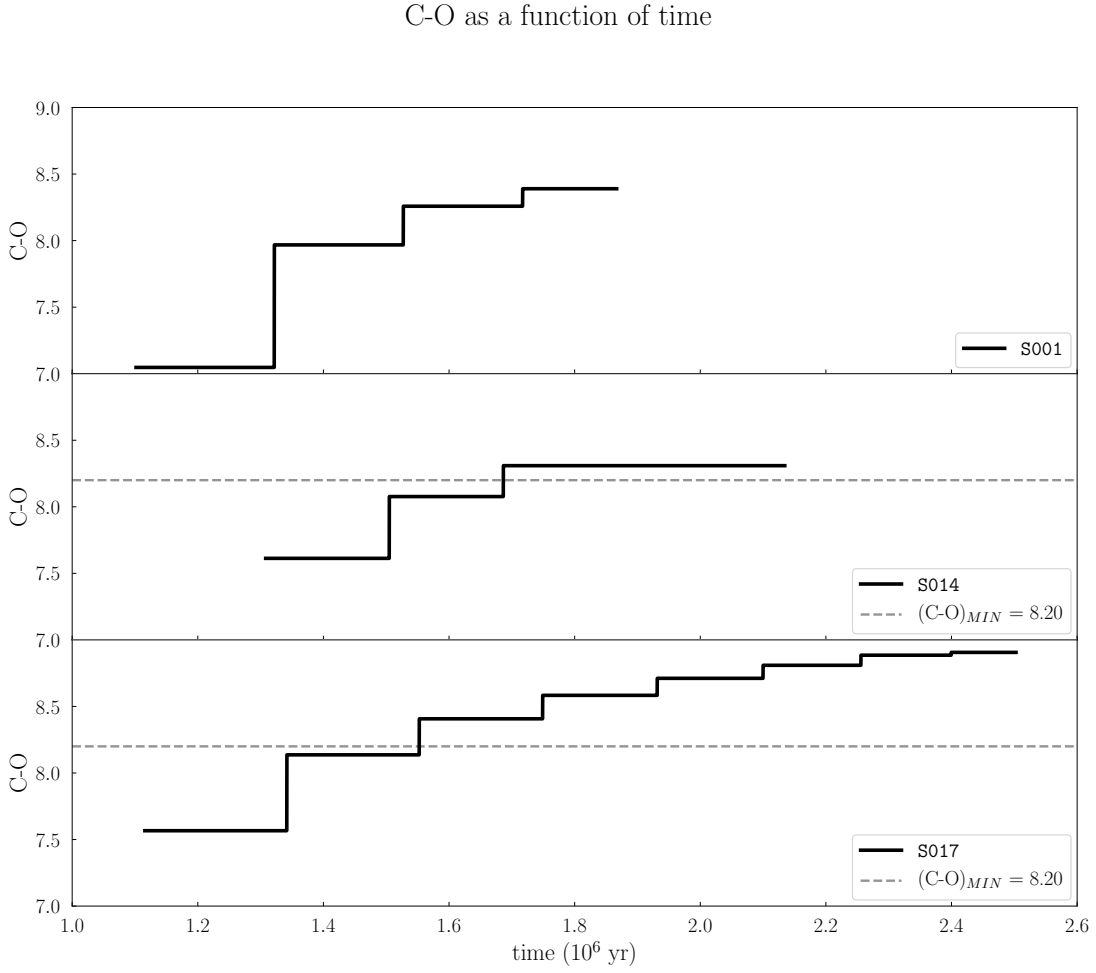

Figure 5.5: Carbon excess as a function of time for the three models `S001`, `S014`, `S017`.

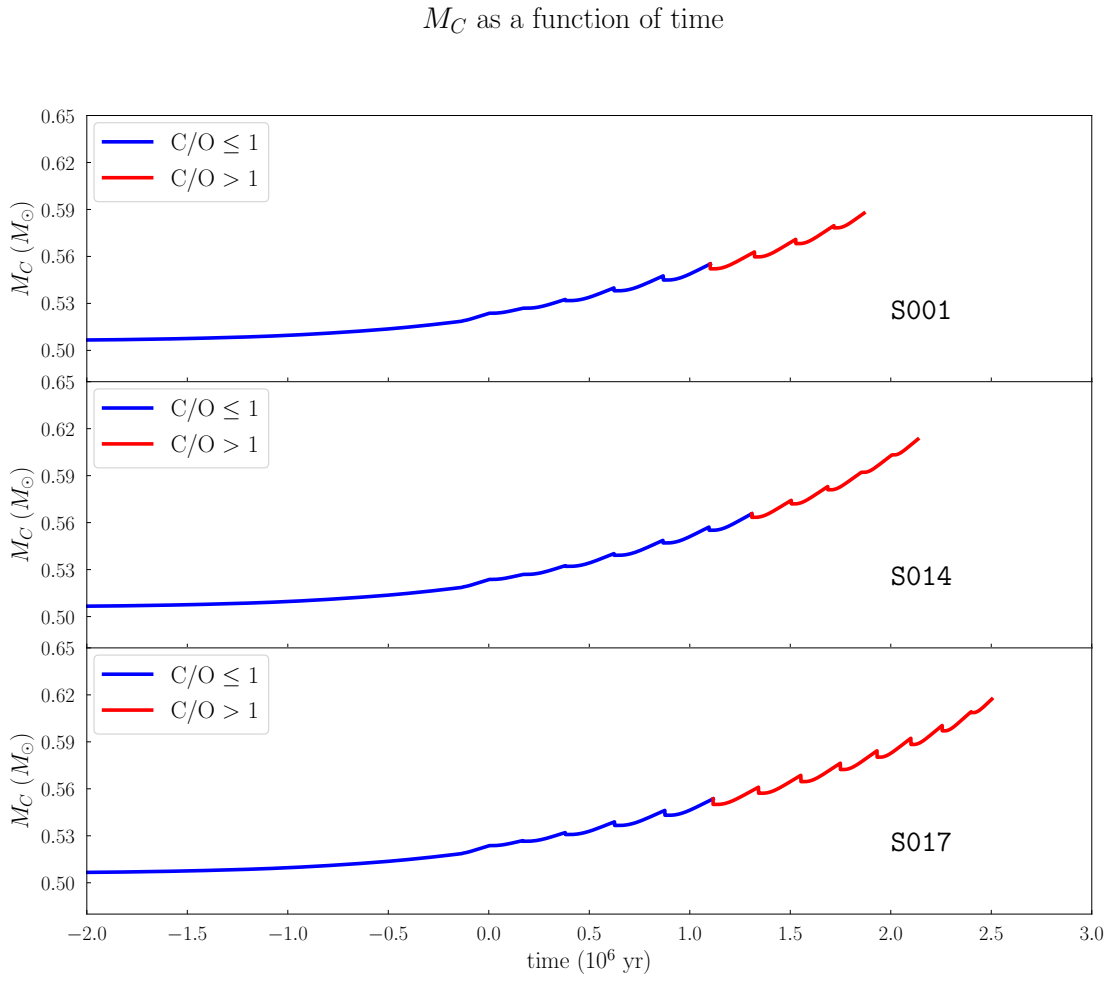

Figure 5.6: Core mass as a function of time for the three models `S001`, `S014`, `S017`.

5.3 Hertzsprung-Russel and Color-Magnitude Diagrams

In Figure 5.7 the effective temperature is shown as a function of time. It can be noticed that the mean trend decreases with time. A pronounced decrement takes place as soon as C/O > 1, due to sudden change of molecular equilibrium and opacities. Model `S017` reaches the lowest T_{EFF}: it is related to the fact that the model predicts also the highest C/O ratio (and so an higher quantity of dust).

In Figure 5.8 luminosity is plotted as a function of time. There is not a drastic change in luminosity as a function of chemical abundance (i.e. when C/O > 1), but L increase monotonically with time. In both plots (Figure 5.7 and 5.8) we note the variations induced by the quasi-periodic occurence of thermal pulses.

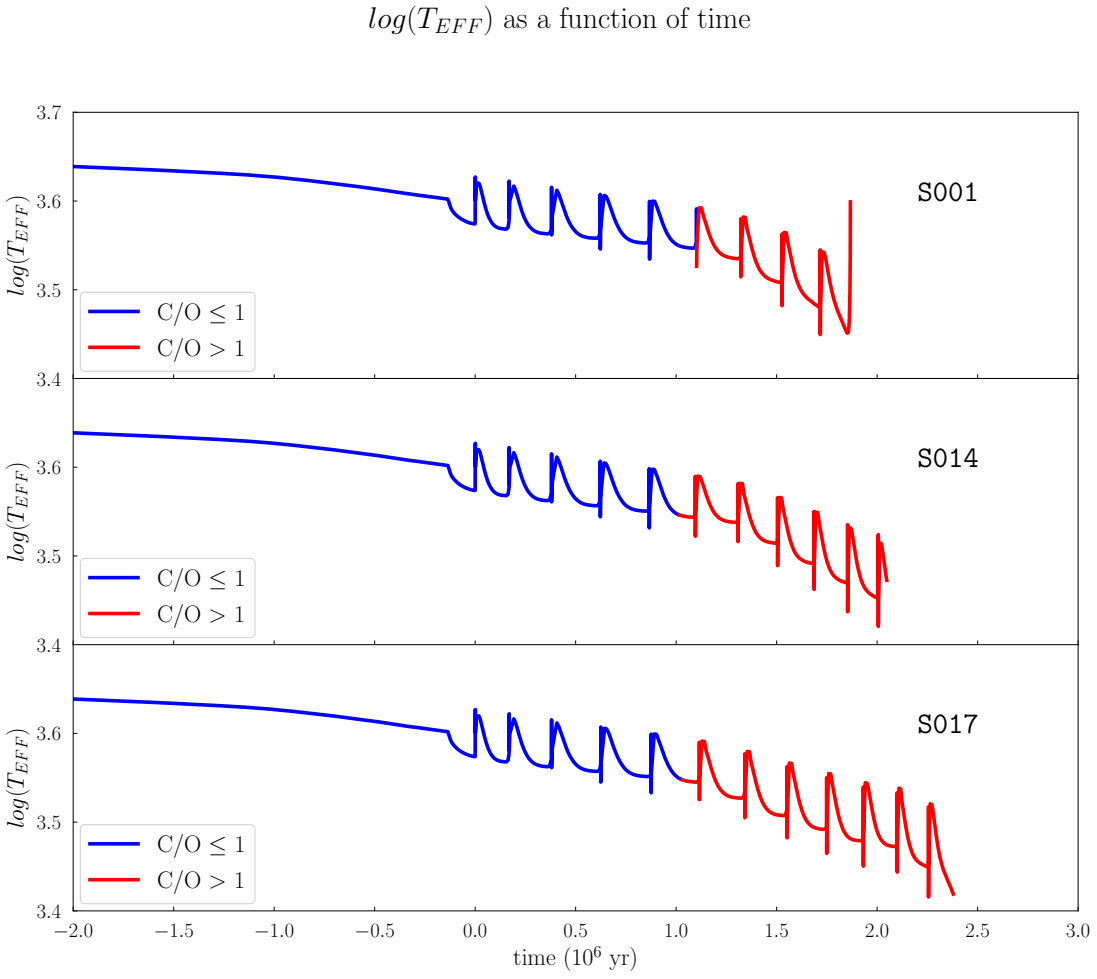

Figure 5.7: Effectve temperature as a function of time for the three models `S001`, `S014`, `S017`.

In Figure 5.9 the evolutionary tracks (including part of E-AGB and the whole TP-AGB phase) are shown for the different models. The points are AGB variables in Kamath et al. (2010). As a general aspect it can be noticed again that there is a significant evolution of T_{EFF} towards lower values beginning from the M/C transition. The highest decrease in T_{EFF} is shown by model `S017`. In Figure 5.9 also the AGB variables in Kamath et al. (2010) are plotted. There is a good agreement between tracks and data.

Finally Figure 5.10 shows the near-infrared CMD of the simulated TP-AGB stars for

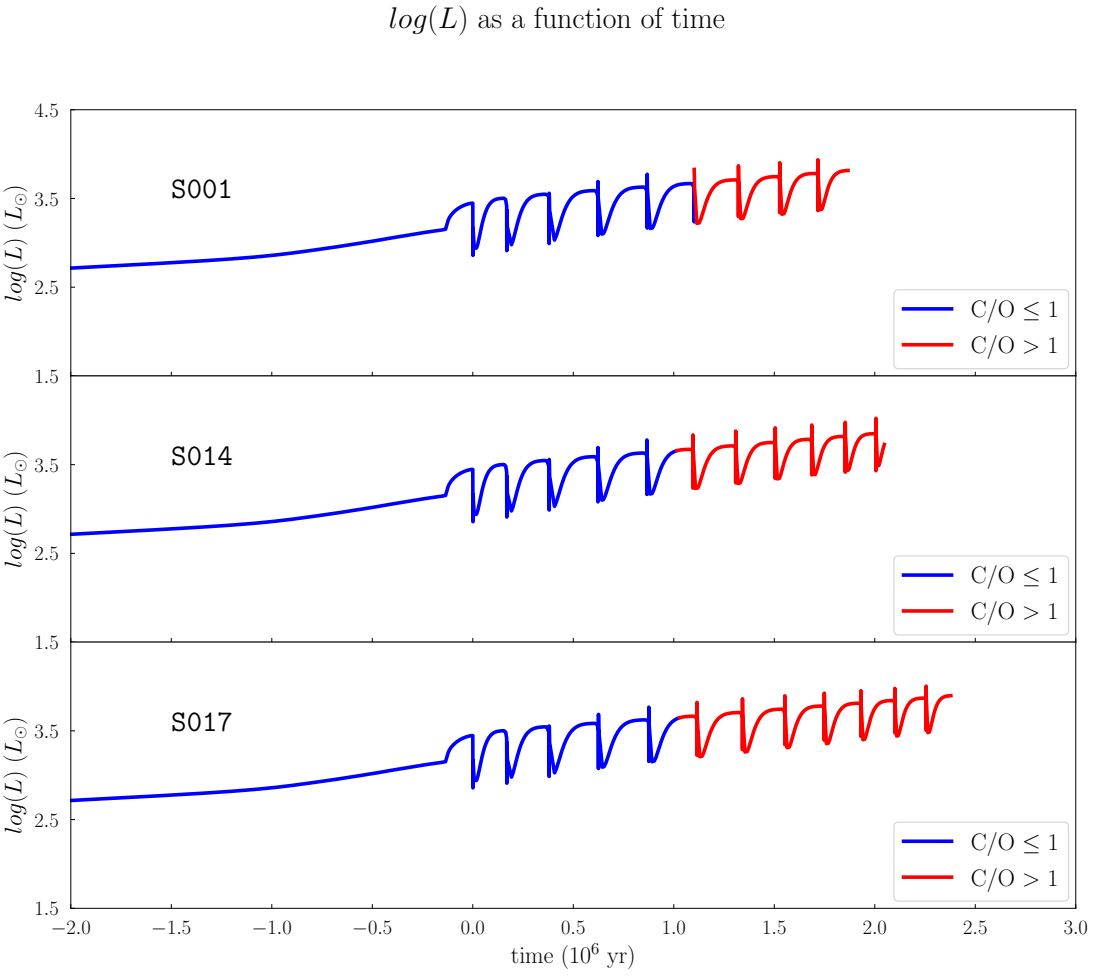

Figure 5.8: Luminosity as a function of time for the three models `S001`, `S014`, `S017`.

the sets `S001`, `S014` and `S017`, compared to the data. The simulated TP-AGB stars plotted come from simulations of the cluster with a mass a thousand times higher than the estimated one. It is useful to plot the total simulation and not only a randomly extracted less massive one just in order to see the general distribution of TP-AGB stars. The stars plotted are the ones with a luminosity $K \leq 12.6$ *mag* (Boyer et al., 2011). The decline of the trends in the diagrams is due to the dust absorption across circumstellar envelopes and re-emission at longer wavelenghts and redder colors. We can note a general agreement with the data, especially for set `S017` which well reproduces the location of C-stars and the observed AGB tip.

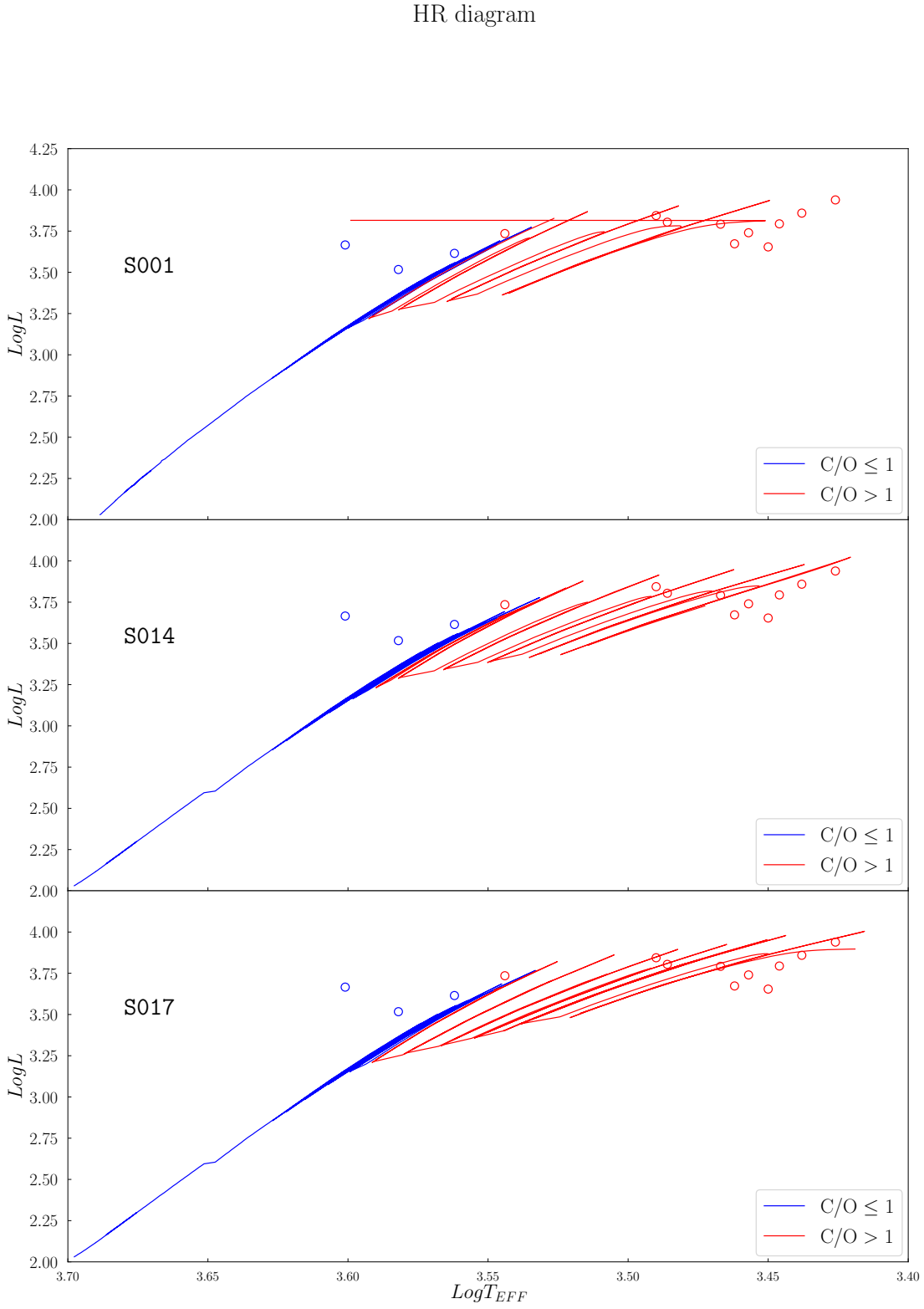

Figure 5.9: HR diagram for the three models `S001`, `S014`, `S017`. The blue and red points are respectively the M-stars and C-stars in Kamath et al. (2010).

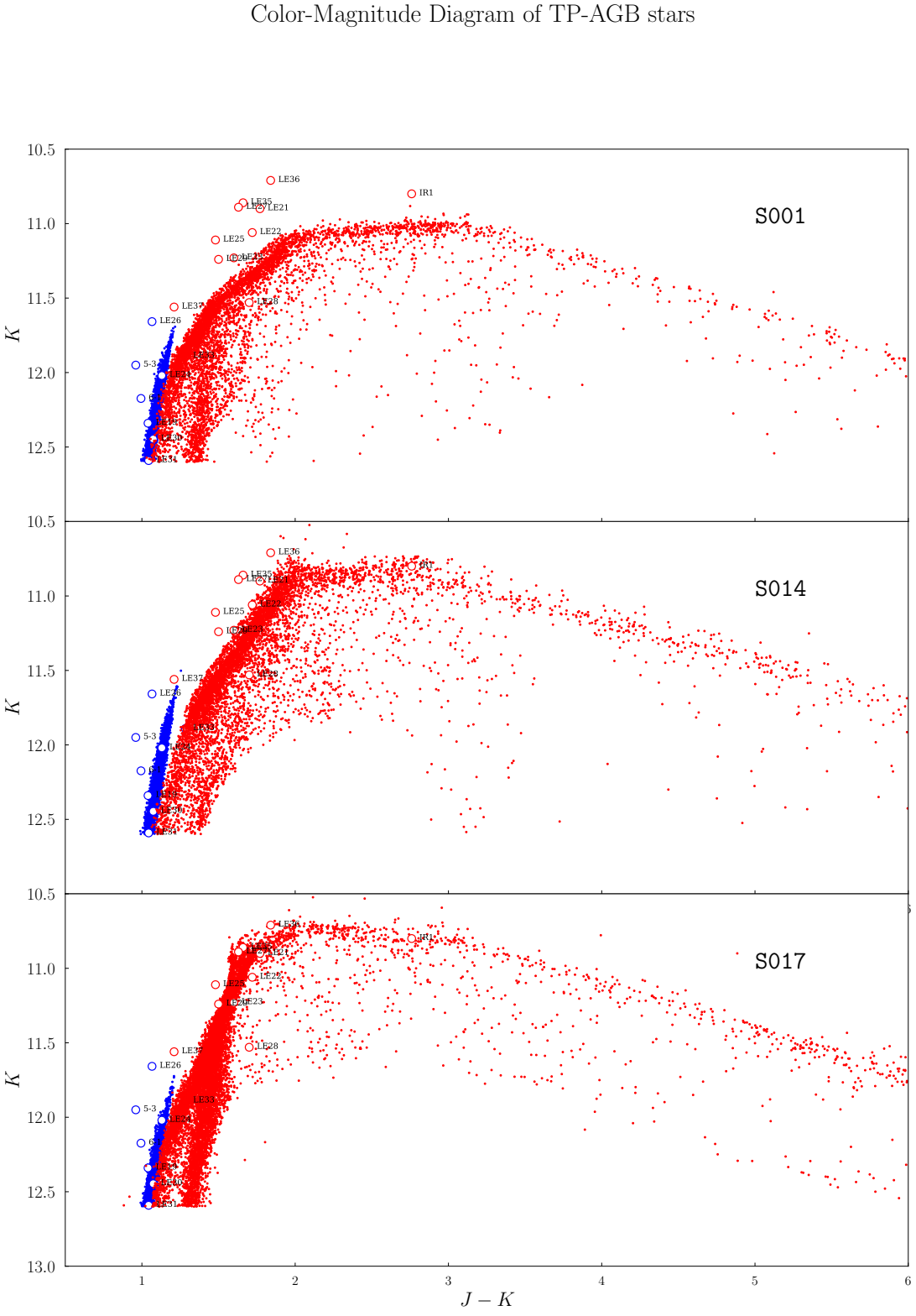

Figure 5.10: Color-Magnitude diagram for the three models `S001`, `S014`, `S017`. The blue and red dots are respectively the M-stars and C-stars produced by simulations, while the empty points are the TP-AGB data of the sample.

5.4 Conclusions

In the framework of a major project aimed at calibrating the AGB stellar evolution phase, we performed simulations using the population synthesis code `TRILEGAL`, focusing on the observed properties of the TP-AGB stars in the SMC star cluster NGC 419.

The TP-AGB stellar models used in simulations mainly depend on two parameters: mass loss and third dredge-up. An interesting result is that the M-star phase, characterized by two observables, i.e. star counts and M/C transition luminosity, is not critically affected by the details of mass loss, rather it is strongly dependent on the activation of the third dredge-up. This helps to disentangle the effects of mass loss and mixing during the calibration of the parameters.

After analyzing a large set of TP-AGB models computed with different prescriptions, we conclude that most of them reasonably reproduce the observed number of carbon-rich stars and the observed AGB tip luminosity. The successful models rely on a moderate efficiency of the third dredge-up (typically $\lambda \sim 0.3$) and a mass loss treatment based on the dynamical model atmospheres for C-stars. They present TP-AGB lifetimes of the order of 2.5 Myr for stars with initial mass of 1.65 $M_{\odot}$. The predicted masses of the resulting white dwarves are $M_{WD} \sim 0.62\ M_{\odot}$, while photospheric carbon-to-oxygen ratio is C/O ~ 5.6.

On the other hand all the models predict an underestimation of the number of oxygen-rich stars and a fainter M/C transition luminosity. Clearly this points to a later activation of the third dredge-up, an indication that will be taken into account in a follow-up work.

Bibliography

Alongi, M., Bertelli, G., Bressan, A., & Chiosi, C. 1991, , 244, 95

Badnell, N. R., Bautista, M. A., Butler, K., et al. 2005, , 360, 458

Bedijn, P. J. 1988, , 205, 105

Bessell, M. S., Wood, P. R., & Evans, T. L. 1983, , 202, 59

Binney, J., & Merrifield, M. 1998, Galactic astronomy / James Binney and Michael Merrifield. Princeton, NJ : Princeton University Press, 1998. (Princeton series in astrophysics) QB857 .B522 1998

Bloecker, T. 1995, , 297, 727

Boyer, M. L., Srinivasan, S., van Loon, J. T., et al. 2011, , 142, 103

Bressan, A., Marigo, P., Girardi, L., et al. 2012, , 427, 127

Caffau, E., Ludwig, H.-G., Steffen, M., Freytag, B., & Bonifacio, P. 2011, , 268, 255

Chabrier, G. 2003, , 115, 763

Charlot, S., & Bruzual, A. G. 1991, , 367, 126

Chen, Y., Bressan, A., Girardi, L., et al. 2015, , 452, 1068

Cranmer, S. R., & Saar, S. H. 2011, , 741, 54

Cutri, R. M., Skrutskie, M. F., van Dyk, S., et al. 2003, "The IRSA 2MASS All-Sky Point Source Catalog, NASA/IPAC Infrared Science Archive.

Dias, B., Coelho, P., Barbuy, B., Kerber, L., & Idiart, T. 2010, , 520, A85

Endal, A. S., & Sofia, S. 1976, , 210, 184

Eriksson, K., Nowotny, W., Höfner, S., Aringer, B., & Wachter, A. 2014, , 566, A95

Frogel, J. A., Mould, J., & Blanco, V. M. 1990, , 352, 96

Girardi, L., Groenewegen, M. A. T., Hatziminaoglou, E., & da Costa, L. 2005, , 436, 895

Girardi, L., Dalcanton, J., Williams, B., et al. 2008, , 120, 583

Girardi, L., Rubele, S., & Kerber, L. 2009, , 394, L74

Girardi, L., Rubele, S., & Kerber, L. 2010, Star Clusters: Basic Galactic Building Blocks Throughout Time and Space, 266, 320

Girardi, L., Marigo, P., Bressan, A., & Rosenfield, P. 2013, , 777, 142

Glatt, K., Grebel, E. K., Sabbi, E., et al. 2008, , 136, 1703-1727

Glatt, K., Grebel, E. K., Gallagher, J. S., III, et al. 2009, , 138, 1403-1416

Goudfrooij, P., Girardi, L., Kozhurina-Platais, V., et al. 2014, , 797, 35

Grevesse, N., & Sauval, A. J. 1998, , 85, 161

Hilditch, R. W., Howarth, I. D., & Harries, T. J. 2005, , 357, 304

Herwig, F. 2004, , 605, 425

Höfner, S., & Olofsson, H. 2018, , 26, 1

Kamath, D., Wood, P. R., Soszyński, I., & Lebzelter, T. 2010, , 408, 522

Kamath, D., Karakas, A. I., & Wood, P. R. 2012, , 746, 20

Karakas, A. I., Lattanzio, J. C., & Pols, O. R. 2002, , 19, 515

Kayser, A., Grebel, E. K., Harbeck, D. R., et al. 2009, Globular Clusters - Guides to Galaxies, 157

Keller, S. C., & Wood, P. R. 2006, , 642, 834

Lloyd Evans, T. 1983, , 204, 985

MacDonald, J., & Mullan, D. J. 2004, , 348, 702

Marigo, P., Girardi, L., Bressan, A., et al. 2008, , 482, 883

Marigo, P., & Aringer, B. 2009, , 508, 1539

Marigo, P., Bressan, A., Nanni, A., Girardi, L., & Pumo, M. L. 2013, , 434, 488

Marigo, P., Girardi, L., Bressan, A., et al. 2017, , 835, 77

Martocchia, S., Cabrera-Ziri, I., Lardo, C., et al. 2017, arXiv:1710.00831

Mattsson, L., Wahlin, R., & Höfner, S. 2010, , 509, A14

Mould, J., & Aaronson, M. 1980, , 240, 464

Nanni, A., Marigo, P., Groenewegen, M. A. T., et al. 2016, , 462, 1215

Pessev, P., Goudfrooij, P., Puzia, T., & Chandar, R. 2008, American Astronomical Society Meeting Abstracts #211, 211, 162.27

Piotto, G., Milone, A. P., Bedin, L. R., et al. 2015, , 149, 91

Renzini, A., & Buzzoni, A. 1986, Spectral Evolution of Galaxies, 122, 195

Rosenfield, P., Marigo, P., Girardi, L., et al. 2016, , 822, 73

Rubele, S., Kerber, L., & Girardi, L. 2010, , 403, 1156

Schröder, K.-P., & Cuntz, M. 2005, , 630, L73

Sirianni, M., Jee, M. J., Benítez, N., et al. 2005, , 117, 1049

Spruit, H. C. 2002, , 381, 923

Trabucchi, M., Marigo, P., Montalbán, J., Wood, P. R., & Girardi, L. 2017, European Physical Journal Web of Conferences, 152, 06009

Vassiliadis, E., & Wood, P. R. 1993, , 413, 641

Willson, L. A. 2000, , 38, 573

Wu, X., Li, C., de Grijs, R., & Deng, L. 2016, , 826, L14

Ringraziamenti

RINGRAZIO la mia famiglia, Mamma e Papà e i miei fratelli Ester, Sofia, Giuseppe, Elisabetta Rosa e Diletta per avermi sempre sostenuta nei momenti difficili, supportata e sopprattutto pazientemente sopportata

GRAZIE al nostro fantastico gruppo di *Astrochef*. Stare in vostra compagnia per me è una delle cose più belle della vita. Siete stati per me indispensabili, abbiamo affrontato mille sfide e ce l'abbiamo fatta! Sono felice che possiamo vivere questo giorno assieme, come a mostrare che è un traguardo "nostro", non individuale, perchè l'unione fa la forza! Grazie Andrea, Piero, Erica, Francesca e Gabriele, Maria Silvia, Francesca, Michela, Martina!

GRAZIE ad Aurelio, Rita, Marta, Priscilla, Luca, Maria, Giacomo, Lucia, Felicita, Giuditta, Elia, Beatrice, Benedetto, Giovanni, Salvatore, Bruno, Domitilla e Paola, per aver reso evidente la Speranza nella mia vita

GRAZIE a Giulia, che in tutti questi anni mi è sempre stata vicina nei momenti più importanti

GRAZIE a Ginevra, carissima amica, fedele compagna di imprese folli, punto di riferimento nei dilemmi esistenziali

GRAZIE alla Prof. Paola Marigo e al Dr. Leo Girardi per la pazienza e la fiducia

THANKS to Dr. Yang Chen for his HUGE patience. All the times you said *"Ah ok"*, every problem seemed surmountable.

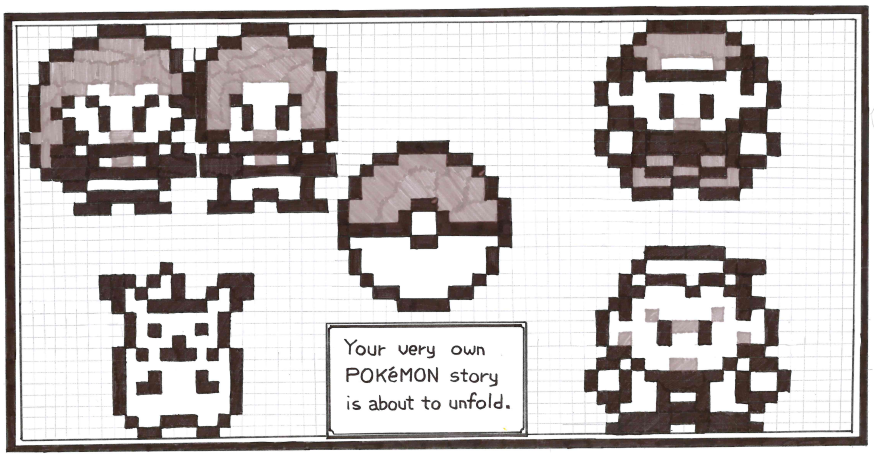
Your very own
POKéMON story
is about to unfold.